Material Design and Electrochemical Behavior Study on Metal-Based Electrocatalysts for Rechargeable Zn-Air Batteries

by

Ya-Ping Deng

A thesis

presented to the University of Waterloo

in fulfilment of the

thesis requirements for the degree of

Doctor of Philosophy

in

Chemical Engineering (Nanotechnology)

Waterloo, Ontario, Canada 2020

Examining Committee Membership

The following served on the Examining Committee for this thesis. The decision of the Examining Committee is by majority vote.

Extremal Examiner	Dr. Chao Wang Associate Professor
Supervisor	Dr. Zhongwei Chen Professor
Internal Member	Dr. Ali Elkamel Professor
Internal Member	Dr. Michael Pope Assistant Professor
Internal-external Member	Dr. Xianguo Li Professor

Author’s Declaration

This thesis consists of material all of which I authored or co-authored: see Statement of Contributions included in the thesis. This is a true copy of the thesis, including any required final revisions, as accepted by my examiners.

I understand that my thesis may be made electronically available to the public.

Statement of Contributions

The body of this thesis is based upon a combination of published work and work drafted for submission. Various chapters are adapted from the following list.

Chapter 1 of this thesis consist of a review paper that was co-authored by myself; my supervisor, Dr. Z. Chen; Drs. G. Jiang; Y. Jiang and A. Yu; and Mr. R. Liang. I prepared the draft and all authors revised this review paper.

"The Current State of Aqueous Zn-Based Rechargeable Batteries", ACS Energy Letters, 2020, 5, 1665.

Chapter 3 of this thesis consists of a paper that was co-authored by myself; my supervisor, Dr. Z. Chen; Drs. Y. Jiang; J. Fu; S. Cheng; Z. Bai; Y. Liu; W. Lei; L. Yang; and J. Zhu; and a PhD student, D. Luo and Mr. R. Liang. I designed and carried out the synthesis, catheterizations, electrochemical measurements as well as the draft preparation. Dr. S. Cheng assisted with processing and reconstructing the tomography data. All authors reviewed and commented on the manuscript.

"Hierarchical Porous Double-Shelled Electrocatalyst with Tailored Lattice Alkalinity toward Bifunctional Oxygen Reactions for Metal−Air Batteries", ACS Energy Letters, 2017, 2, 2706.

Chapter 4 of this thesis consists of a paper that was co-authored by myself; my supervisor, Dr. Z. Chen; Drs. Y. Jiang; Y. Hu; X. Wang; J. Li; and A. Yu, a PhD student, D. Luo; and Mrs. R. Liang and S. Zhang. I; Drs. A. Yu; and Z. Chen conceived the

concept and initiated the project. I; Drs. Y. Jiang; X. Wang and J. Li. carried out the synthesis, performed electrochemical measurements, and characterizations. S. Zhang and D. Luo assisted with characterizations. Dr. Y. Hu participants in the setup design for operando X-ray absorption spectroscopic measurements and X-ray absorption spectroscopy analysis. All authors read and commented on the paper.

"Dynamic electrocatalyst with current-driven oxyhydroxide shell for rechargeable zinc-air battery", Nat. Commun. 2020, 11, 1952.

Chapter 5 of this thesis consists of a manuscript that was co-authored by myself; my supervisor, Dr. Z. Chen; Drs. Y. Jiang; A. Yu and Mr. R. Liang. I designed and carried out the synthesis, catheterizations, electrochemical measurements, as well as the draft preparation. Dr. Y. Jiang assisted with the characterizations. R. Liang helped with the manuscript revision. All authors reviewed and commented on the manuscript.

Abstract

Zn-based electrochemistries can provide bivalent redox, reserve abundancy in earth, moderate reactivity, and compatibility with aqueous electrolyte. When comparing to Li-based battery technologies, their superiorities in energy/power density, cost and safety are demonstrated. As the sub-branch of Zn-based electrochemistries, rechargeable Zn-air battery has drawn tremendous research attention in the past decade and been considered as one of the most promising candidates for commercial energy storage and conversion systems. However, some challenges still remain at its core components and hinder the commercialization of its rechargeable versions, such as the sluggish electrocatalytic kinetics and inferior cycleability at the air cathode side, inevitable volatilization and CO_2 poisoning of alkaline electrolyte, and dendrite formation and side reactions at Zn anode side. In this thesis, the primary efforts have been paid to showcase the performance optimization through nanostructure engineering on metal-based electrocatalyst and understand their electrochemical behavior as well as the corresponding structural evolution under rechargeable Zn-air battery operation.

In the first work, based on the proposed design principles regarding the accessibility and efficiency of active sties in electrocatalyst, a hierarchical porous double-shelled spinel Co_3O_4 with controllable Mg substitution is designed and synthesized *via* an *in-situ* coordinating process. These morphology and composition features are validated by microscopic and structural characterizations. The hierarchical porosity is capable to optimize the availability of active sites and broaden mass diffusion channels. Meanwhile, Mg substitution is beneficial to increase the overall electrical conductivity and tailor the lattice alkalinity (*i.e.* the hydroxyl concentration within lattice). Specifically, the substituted Mg is considered to induce the creation of

buffer zones within lattice of electrocatalyst, which can promote hydroxyl detachment from nearby catalytic sites. As a result, the catalytic site accessibility and intrinsic activity of multi-shelled materials are both increased. The electrochemical measurements confirm the performance merits of such electrocatalyst in the comparison with the limited porous or Mg-free counterparts.

The second work is regarding the synthesis of a Co-Fe containing bimetal nitride with a morphology of hollow nanocuboid. Benefiting from its morphological and conductive merits, at the raw state, it exhibits battery parameters that are comparable to the noble-metal benchmark. Then, a notable maturation process is further demonstrated with performance increments in power density and discharge-charge voltage gap within the initial several cycles. By means of time-resolved X-ray and electron spectroscopic analyses, its actual configuration and structural evolution during the maturation period is visualized, and a concept of "dynamic electrocatalyst" is proposed. The battery cycling is a dynamic process for such bimetal nitride, including the gradual establishment of a "shell-bulk" configuration and periodic valence variation of Co, which is responsible for the performance improvement and stabilization during long-term cycling.

Thirdly, with the knowledge gained from the metal nitrides, a Ni-Fe diselenide with a nanobox morphology is prepared as another demonstration for "dynamic electrocatalyst". Besides the metal cations, the electrochemical evolution of Se is also recorded by *operando* measurements. As shown, an amorphous phase is generated along with decreased diselenide feature during the maturation process, and hence the "shell-bulk" configuration is also established for this diselenide. Within this amorphous shell, the periodic valent variation of Ni is observed and identified as the electrocatalytic active sites, while Fe exhibits inert response to electrochemical

condition and maintains its chemical state. More importantly, the oxidation of Se is also monitored on the surface without generation of any other new species. The positive effect of Se on the battery performance is clearly demonstrated and considered as the key in the comparison with the alloy-based counterpart.

In summary, this thesis presents three types of metal-based oxygen electrocatalysts with different nanostructures for rechargeable Zn-air battery. By taking advantages of advanced characterization techniques, new insights are provided herein to confirm their morphology features, isolate the active site, identify the actual configuration, and understand their electrochemical behavior. On the basis of these results, some novel design blueprints for electrocatalyst may be inspired to drive the development of rechargeable Zn-air battery into a practical era.

Acknowledgement

I would like to thank my supervisor Professor Zhongwei Chen who gave me the opportunity and resources to work on the topic of zinc-air batteries. He guided and inspired me throughout my Ph.D. study, and gave me the freedom to pursue various research ideas. Also, I would like to thank my Ph.D. thesis examining committee, including Professor Xianguo Li, Professor Ali Elkamel, Professor Michael Pope from the University of Waterloo, and Professor Chao Wang as my external examiner from John Hopkins University, for their valuable time and contributions through this important process.

I would like to thank all the group members at Applied Nanomaterials and Clean Energy Laboratory, especially those who have worked on zinc-air batteries and assisted me during my Ph.D. study. During the last two years, I got several opportunities to conduct experiments at Canadian Light Source. It was my great honor working with the beamline mangers, Dr. Yongfeng Hu and Dr. Qunfeng Xiao from Soft X-ray Microcharacterization Beamline, Dr. Graham King from Brockhouse X-ray Diffraction and Scattering Beamline, Dr. Renfei Feng from Very Sensitive Elemental and Structural Probe Employing Radiation from a Synchrotron beamline and Dr. Ning Chen from Hard X-ray MicroAnalysis Beamline. Special thanks for sharing the knowledge and ideas with me and give me hints to tackle challenges from the projects.

I would also like to express my gratitude to my friends, my parents and my wife for their unconditional support and encouragement. Dedicated to them for standing with me all the time with their love and caring.

Finally, I would like to acknowledge the funding sources, including China Scholarship Council, Natural Sciences and Engineering Research Council of Canada, the Waterloo Institute for Nanotechnology, and the University of Waterloo, for the financial support.

Table of Content

List of Figure

List of Tables

List of Abbreviations

Abbreviations	Intended Word/Phrases
SEM	Scanning Electron Microscopy
TEM	Transmission Electron Microscopy
STEM	Scanning Transmission Electron Microscopy
EDS	Energy Dispersive X-ray Spectroscopy
SAED	Select Area Electron Diffraction
EELS	Electron Energy Loss Spectroscopy
ELNES	Energy Loss Near Edge Structure
FFT	Fast Fourier Transform
XPS	X-Ray Photoelectron Spectroscopy
XRD	X-Ray Diffraction
SXRD	Synchrotron X-Ray Diffraction
WAXS	Wide-Angle X-ray Scattering
XAS	X-ray Absorption Spectroscopy
XANES	X-ray Absorption Near Edge Structure
EXAFS	Extended X-ray absorption fine structure
TEY	Total Electron Yield
TFY	Total Fluorescence Yield
BET	Brunauer–Emmett–Teller
EPR	Electron Paramagnetic Response
ICP-AES	Inductively Coupled Plasma Atomic Emission Spectroscopy
ORR	Oxygen Reduction Reaction
OER	Oxygen Evolution Reaction
RDE	Rotating Disc Electrode
RHE	Reversible Hydrogen Electrode
SCE	Saturated Calomel Electrode
LSV	Linear Sweep Voltammetry
CV	Cyclic Voltammetry
η	Overpotential
GDL	Gas Diffusion Layer

1 Introduction

1.1 Energy challenge

The effects of climate change and fluctuation of petroleum prices have forced the battery community to seek for alternative energy storage and conversion systems to meet the increasing energy and power requirement of various portable devices or electrical vehicles. In the past 30 years, Li-ion batteries have drawn extensive research attention and already been commercialized as power systems in numerous products, such as Tesla and Apple. However, because of the interaction electrochemistry that generates electricity through migration of Li^+ between cathode and anode materials,[1, 2] the most state-of-the-art battery products are struggling to achieve a energy density of 500 Wh kg^{-1}, even when all the battery components are pushed to their performance limit.[3, 4] Such energy density is feeble to chase the ever-growing practical demands in traveling distance of electrical vehicles. Besides, the low reserve of Li and the inevitable employment of Co in cathode results in that the current cost of commercial Li-ion batteries is still higher than $150 per kWh.[5] Then, Li-O_2 and Li-S batteries were proposed as possible alternatives with higher energy density,[6, 7] and meanwhile Na- and K-based batteries are also received significant interests due to their higher material abundancy in the Earth crust.[8, 9] However, there is another issue regarding those alkali metal based battery technologies, *i.e.* safety concern. These alkali metal batteries primarily utilize aprotic electrolytes due to their water and air sensitive nature, which may lead to fire and explosion hazard.[10]

In comparison, aqueous batteries using multivalent ions open up possibilities for much safer technologies using multi-electron involved redox couples.[11, 12] These

multi-electron transferred reactions can theoretically provide a comparable or even higher energy density in comparison to current Li-ion batteries. The common configuration for these battery technologies usually include a metallic anode, aqueous electrolyte, separator, and cathode. By taking advantage of different redox couples at anode, such as Mg^{2+}/Mg, Al^{3+}/Al, Fe^{2+}/Fe, and Zn^{2+}/Zn *etc.*, various battery output parameters can be obtained to meet different application targets. With recent development of material science, most of these couples have already been validated in a rechargeable manner.[11, 13] Among them, Zn-based electrochemical technologies are widely considered as the most promising prospect due to their high rechargeability and practical potential. Other major superiorities of Zn also include its natural abundancy, safety and projected low cost of below \$100 kWh^{-1}.[14]

1.2 Zn-based electrochemistries

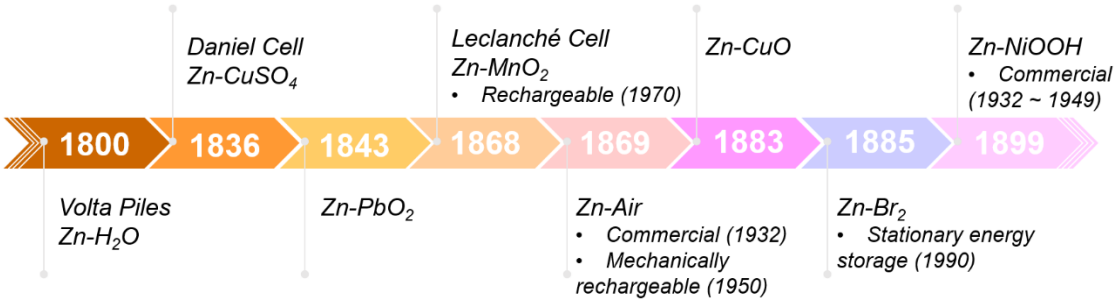

Figure 1-1 The historic timeline of Zn based battery technologies. The data were obtained from the ref[15].

As shown in the historic evolution (**Figure 1-1**), Zn-based technologies are the easiest battery systems starting from Volta Piles to Daniel Cell and the later Zn-MnO_2, Zn-air, Zn-Br_2 or Zn-NiOOH batteries, which were invented more than a century ago.[15] Although some preliminary products have already entered the market, most of them are

rejuvenated recently and drew substantial research efforts to push forward their commercialization. These batteries are established on the basis of Zn^{2+}/Zn redox couple.

$$Zn^{2+} + 2e^{-} \rightleftharpoons Zn,\ E° = 0.763\ V\ \textit{vs.}\ \text{Standard Hydrogen Electrode (SHE)}$$

At the cathode side, a wide range of electrochemistries are available and several categories of aqueous Zn-based batteries are proposed, which mainly include Zn-ion, Zn-redox, and Zn-air batteries.[16, 17]

1.2.1 Zn-ion Battery

Various families of cathode with different crystal structures have been proposed as cathodes for Zn-ion batteries, which mainly consist of Mn-based, V-based, Ni-based, Prussian blue analog or organic cathodes.[16, 18, 19] Based on their electrochemical behaviors, these cathodes can be classified into two general categories, *i.e.* intercalation and conversion. Similar to Li-ion batteries, intercalation type Zn-ion batteries exhibit Zn^{2+} intercalation into cathode crystal and reduction of corresponding elements during discharge, while Zn deintercalation occurs with oxidation of principle elements when charged.[20, 21] Typically, suitable cathodes exhibit multi-electron redox couples and wide crystal channels for Zn^{2+} diffusion, one particular example is the Mn^{4+}/Mn^{3+} couple that provides up to 1 e^{-} per formula unit in mildly acidic Zn-MnO_2 batteries, which was also named as Leclanché cell and firstly emerged in 1868.[22, 23] As for the conversion-based cathodes, they utilize the redox transition of principle metals between oxide and hydroxides or corresponding oxyhydroxides, this process can also be represented as H^{+} insertion.[24] A typical example is Zn-NiOOH batteries that was proposed in 1899 using Ni^{3+}/Ni^{2+} redox couples with Faradaic reactions between NiOOH and $Ni(OH)_2$.[25-27] In many cases, the conversion and intercalation chemistries co-exist in Zn-ion batteries, especially for Zn-MnO_2 batteries. Specifically, conversion of the cathode occurs after

H^+ insertion, and then the phase-transformed cathodes act as the host for Zn intercalation during cycling.[22, 28] As for solution to address the intrinsic limitation on the cell voltage and energy density of Zn-ion batteries, the electrolyte related research beyond conventional mildly acidic or neutral saline solution is the current hotspots. These key battery parameters can be boosted by unlocking new chemistries. As such, the incorporation of Mn^{2+} electrolysis into the cathode reactions and the employment of alkaline Zn redox have been proposed and both showcased their feasibility in raising the working voltage of Zn-ion batteries.[29-31]

1.2.2 Zn-redox battery

The second category is Zn-based redox batteries with flowing electrolyte.[32] They are established by coupling Zn anode with different redox couples, mainly including Zn-halogen (Cl_2,[33] Br_2[34] and I_2[35-37]), Zn-Fe,[38] Zn-Ce,[39] and Zn-organic batteries (*e.g.* quinone,[40] 2,2,6,6,-tetramethylpiperidinyloxyl[41] and polymers[42]). Although some of them, such as Zn-Br_2 and Zn-Fe, have been demonstrated in the scale of tens to hundreds of kWh, further efforts are still paying into improving their key parameters to meet practical feasibility and compete with the commercially available V-based flow batteries.[43, 44] The current attentions of Zn-based redox battery are primarily focused on development and optimization of electrolyte, membrane and electrode. Taking Zn-I_2 flow battery as an typical example, it was initiated in 2015 by employing concentrated ZnI_2 aqueous solution as both anolyte and catholyte that were segregated by Nafion membrane.[36] Zn plating-stripping was paired with the reversible conversion between triiodide and iodide ($I_3^- + 2e^- \rightleftharpoons 3\ I^-$, $E° = 0.536$ V *vs.* SHE) to build up a cell potential of 1.299 V and a discharge energy density of 167 Wh L^{-1}. Following such, the studies focused on electrolyte composition was reported by adding Br^- as supporting electrolyte to stabilize extra I^- and increase its energy density to 202 Wh L^-

[1].[45] While a level-up value of 330.5 W h L^{-1} was reported by another work utilizing alkaline anolyte.[37] As for membrane development, multiple properties are usually considered, including ion conductivity that determines maximum areal current density and voltage efficiency, ion selectivity that minimizes self-discharge rate and improves columbic efficiency, chemical resistivity and mechanical stability.[43] In addition to the commercial Nafion membrane, porous polyolefin based membranes have been investigated for Zn-I_2 flow batteries.[35, 46] Meanwhile, some studies are focusing on the development of cathodes with high electrocatalytic activity to promote the I_3^-/I^- redox couple. Their electric conductivity, wettability and porous structure are also crucial properties.

1.2.3 Zn-air Battery

Zn-air battery is also a century-old system that was proposed in 1869, its primary products were first commercialized in 1932 and its rechargeable version was provided in a mechanical manner in 1950.[17] Then, Zn-air battery felt into a long-time silence that was finally broken until 2010s by substantial progresses on material science to drive this battery technology into an electrically rechargeable era.[14, 47, 48] Zn-air battery is conceptually different with other aforementioned Zn-based technologies, as it works in a half-open system and its main fuel is O_2 from the air.[49] In a rechargeable Zn-air battery system, electrocatalytic oxygen redox at triple-phase boundaries of electrocatalyst in alkaline aqueous electrolyte is the reversible cathode reactions:[17, 48, 50]

$$O_2 + 4e^- + 2H_2O \rightleftharpoons 4OH^-,\ E° = 0.4\ V\ \textit{vs.}\ SHE$$

Briefly, oxygen reduction reaction (ORR) occurs during discharge while oxygen evolution reaction (OER) is responsible for charge.[51] The background and electrochemistry of Zn-air battery will be expanded in detail in the following section.

1.3 The fundamentals of Zn-air battery

1.3.1 The comparison with other metal-air batteries

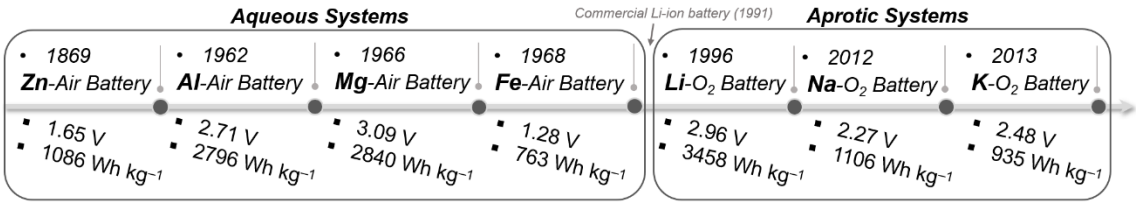

Figure 1-2 The invention timeline and key parameters of different metal-air batteries. The data were obtained from the Refs[15, 17].

Zn-air battery was the first energy system since the awareness on the positive influence of O_2 upon battery operation.[15] Then, the air-based versions of various metals were successively proposed at early age as shown in **Figure 1-2**, including Al-air (1962), Mg-air (1966) and Fe-air (1968) batteries.[17] Along with the launch of commercial Li-ion batteries in 1991, the research interests on alkali-O_2 batteries based on aprotic electrolyte was sharply increased, followed by the rapid landing of Li-O_2 battery (1996). Due to the similar dilemma of Li reserves with Li-ion batteries, Na-O_2 and K-O_2 batteries were put forward latter at the year of 2012 and 2013, respectively.[52, 53] At this point, the current family of air involved batteries have been established and can be classified into two categories according to their different electrolytes, *i.e.* the aprotic and aqueous systems.

As for the aprotic category, including Li-air (the theoretical energy density of 3458 Wh kg^{-1}), Na-air (1106 Wh kg^{-1}) and K-air batteries (935 Wh kg^{-1}), they are still at the very early stages of development and none commercial product has been proposed.[6, 54-61] Although their working voltage (> 2 V) are appealing advantages, the requirement of organic solvents as electrolyte in these systems leads to some intrinsic

problems, such as inferior ORR kinetics, the inevitable formation of insoluble metal peroxides or superoxides that hold up oxygen diffusion at air electrode, and possible fire hazard when water is introduced into batteries and reacts alkali metals.[6, 17, 62] In the aqueous category, Fe-air batteries (763 Wh kg^{-1}) present very low practical energy density in the range of 60−80 Wh kg^{-1}, despite its long cycleability (more than 1000 cycles) and low cost.[17, 63] Although Al-air (2796 Wh kg^{-1}) and Mg-air batteries (2840 Wh kg^{-1}) have very high theoretical energy densities, the severe corrosion reaction and the corresponding H_2 evolution at the anodes greatly restrain attempts in their practical applications. Besides, it is generally accepted that the electroreduction of Al and Mg is thermodynamically infeasible in aqueous environment and there is yet to be any reporting of rechargeable Al-air and Mg-air batteries.[17]

In comparison, Zn-air battery (1086 Wh kg^{-1}) is the option with the highest practical possibility as electrochemical energy storage and conversation systems for powering electrical vehicles in the near future, because of their decent practical energy density (350−500 Wh kg^{-1}), moderate reactivity and electrical rechargeability.[64-66] Nevertheless, some technical challenges have yet to be solved, *e.g.* low bifunctional oxygen electrocatalytic kinetics, insufficient durability of electrocatalysts, detrimental effect of CO_2 and zinc dendrite.

1.3.2 Battery configuration and electrochemistry

Generally, as illustrated in **Figure 1-3**, a rechargeable Zn-air battery consists of Zn metal as anode, membrane separator and air electrode as cathode.[48, 64] It is usually assembled based on a layer-by-layer planar prototype using polymethyl methacrylate (PMMA) or Teflon plates and rubber pieces to seal the electrolyte, while the strain-less mesh and copper sheet are usually utilized as the current collectors at cathode and anode

sides, respectively. Alkaline aqueous solution, such as KOH or NaOH, dissolved with Zn acetates or Zn oxides is the electrolyte, the concentration of KOH or NaOH is relatively high (usually 6M) to enable reasonable diffusion kinetics for both cathode and anode reactions. The air electrode usually consist of a catalytic active layer on carbon paper as the gas diffusion layer (GDL).[48] The electricity is generated by the redox reaction between Zn anode and air cathode.[51] During discharge, O_2 in atmosphere is pulled into the GDL by pressure gradients. Then, the electrocatalysts on GDL reduces the O_2 to OH^- ions, *i.e.* ORR, with the corresponding oxidation of Zn.[63, 65] The reverse process in terms of OER and Zn^{2+} reduction occurs when batteries are charged. The detailed reactions are provided as follow:[17, 51, 64]

Cathode: $O_2 + 2H_2O + 4e^- \rightleftharpoons 4OH^-$ (E° = +0.4 V *vs.* RHE)

Anode: $Zn \rightleftharpoons Zn^{2+} + 2e^-$

$Zn^{2+} + 4OH^- \rightleftharpoons Zn(OH)_4^{2-}$ (E° = −1.25 V *vs.* RHE)

$Zn(OH)_4^{2-} \rightleftharpoons ZnO + H_2O + 2OH^-$

Overall: $2Zn + O_2 \rightleftharpoons 2ZnO$ (E° = +1.65 V *vs.* RHE)

Both cathode and anode have their respective challenges, such as the dendrite formation on metallic Zn, the sluggish kinetics of electrocatalyst as well as their inferior durability in battery operation. Therefore, intensive research efforts have been paid to address these issues and seek for performance improvement on rechargeable Zn-air batteries.

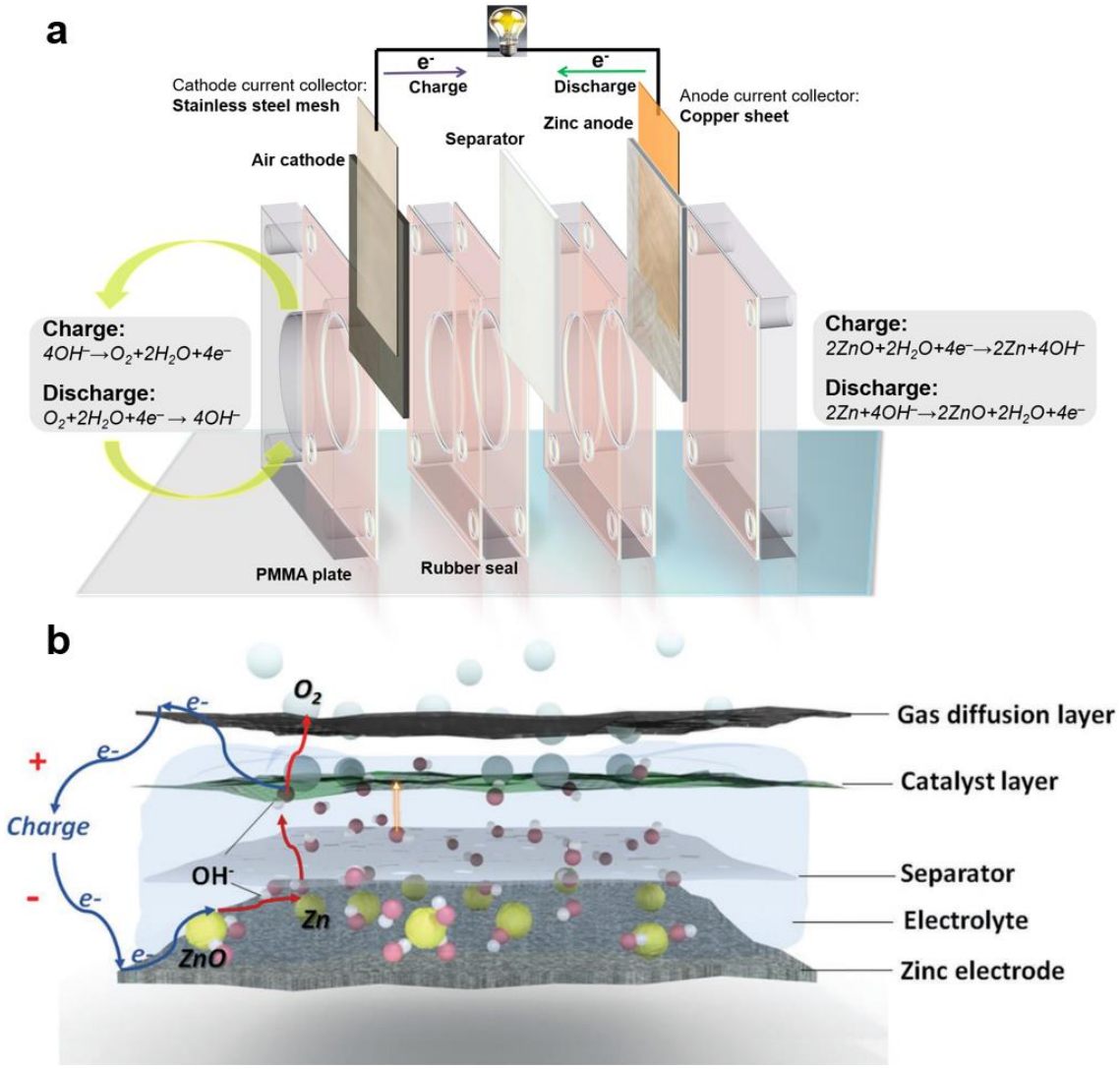

Figure 1-3 (a) The schematic assembly of Zn-air battery. Reproduced with permission from ref[67]. Copyright 2017 Royal Society of Chemistry. (b) The mechanical demonstrations at molecular level. Reproduced with permission from ref[48]. Copyright 2017 John Wiley & Sons, Inc.

1.3.3 Zn anode

Similar to other Zn-based batteries, metallic anode, *e.g.* Zn foil, is applied directly in most cases. As shown in the anode reaction, Zn losses two electrons and dissolves into the electrolyte during discharge, while it plates back onto the anode when charged. In the meantime, Zn anode experiences some side reactions, *e.g.* hydrogen

evolution reactions (HER), and thus self-discharge as a result of its inferior thermodynamic stability in aqueous electrolyte.[68] The solutions to address this issue can be divided into two major aspects, surface engineering and electrolyte additives. For example, the Al_2O_3 coating and Bi alloying both increased HER overpotentials,[69, 70] while the additives could also act as an organic inhibitor in alkaline electrolyte to reduce side reactions.[71] The major challenge regarding Zn anode lies in the dendrite suppression. Generally, uneven distribution of Zn^{2+} on anode surface and preferential deposition at tip spots are the primary reason for leaf-like Zn dendrites.[68] These dendrites can penetrate the separator and cause battery failure through internal short circuiting. Therefore, regulating plating behavior and suppressing Zn dendrite formation are critical for prolonging battery lifetime.[26, 72, 73] Another recent research hotspot is the development of electrolyte to achieve Zn dendrite suppression, such as the so-called "water-in-salt" electrolyte based on highly concentrated bis(trifluoromethanesulfonyl)imide (TFSI).[74, 75]

1.3.4 Air cathode

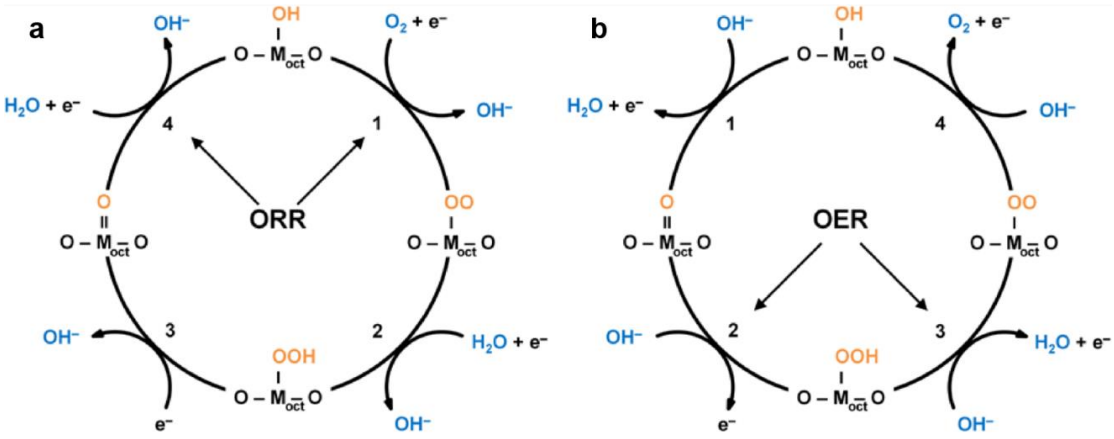

Figure 1-4 The schematic electron/proton coupled (a) ORR and (b) OER mechanisms. Reproduced with permission from ref[76]. Copyright 2017 John Wiley & Sons, Inc.

In air cathode, bifunctional oxygen electrocatalyst plays a critical role in determining the key battery parameters. **Figure 1-4** demonstrates the intermediate steps of ORR (discharge) and OER (charge) processes. Specifically, the cleavage of strong O−O bonds (498 kJ mol^{-1}) in the multi-electron ORR required large activation energy, and assistance of electrocatalysts is essential for the occurrence of the process.[77-79] As for OER, it also experiences kinetically sluggish multi-step processes to generate O_2.[79-83] The electrocatalytic mechanisms describe two general processes on the surface of air cathode, including reactants adsorption and electrocatalysis. The first one is mainly influenced by the geometry properties and hydrophilia of electrocatalysts, while the later one is reflected by its charge transfer (*i.e.* electrical properties) and electrocatalytic efficiency.

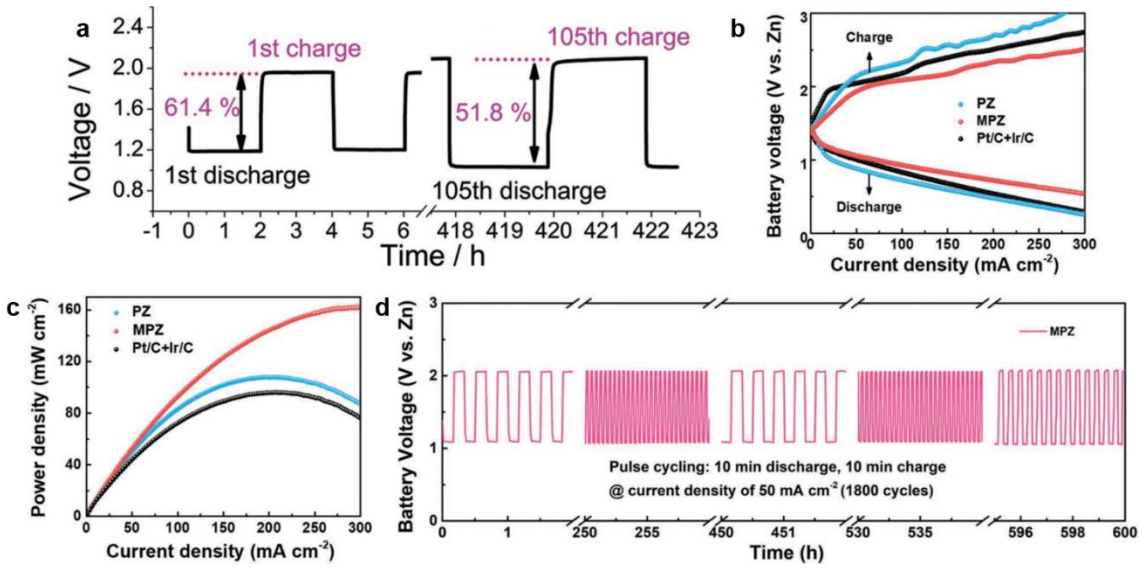

Figure 1-5 (a) The discharge-charge voltage gap as well as the calculated energy efficiency; (b) the polarization curves, (c) the power density and (d) cycling profile of Zn-air battery. Reproduced with permission from refs[84, 85]. Copyright 2016 and 2018, John Wiley Sons, Inc.

Two aspects of battery parameters are usually taken into consideration in performance evaluation of a Zn-air battery: activity and rechargeability. Specifically, the activity includes the energy efficiency (or stated as discharge-charge voltage gap, **Figure 1-5a**), polarization (**Figure 1-5b**) and power density (**Figure 1-5c**). The bifunctionality of electrocatalyst is responsible for these activity parameters. The rechargeability (or cycleability, **Figure 1-5d**) describes the battery lifetime in cycling measurements at various current densities. Besides the aforementioned dendrite growth at anode and electrolyte loss or leakage, the rechargeability is heavily dependent on the stability and durability of bifunctional electrocatalysts.

1.4 Oxygen electrocatalyst

As demonstrated above, superior bifunctional oxygen electrocatalysts are critical to reduce the activation energy and increase conversion kinetics of both ORR and OER in a durable manner. Although noble-metal materials based on Pt, Pd, Ir or Ru *etc.* have the halo of ORR or OER benchmarks, their scarcity, high cost and inferior bifunctionality render them unsuitable for this system.[86] As such, the development of feasible and low-cost electrocatalysts is the core challenges in Zn-air battery studies.

1.4.1 Material categories

1.4.1.1 Carbon materials

Carbon materials, or metal-free materials, emerged as one of the earliest considerations due to their cost efficiency and high conductivity.[87] With the aim to optimize their electrocatalytic activity, N-, S- or P-doping are usually used to tune their active sites,[88, 89] and application of these carbon materials in Zn-air batteries were also reported.[89, 90] Taking N dopants as an example, four kinds of N species can be

obtained after carbonization in high-temperature calcination, including pyridinic, quaternary, pyrrolic and oxidized N.[90] Dai *et al.* studied the temperature influence on the N dopants and examined the application of N-doped carbon in rechargeable Zn-air battery as shown in **Figure 1-6**.[90] This battery provided a peak power density of 55 mW cm^{-1} outperforming Pt/C. Among different N species, Liu *et al.* further identified n-type N dopants (quaternary) as ORR active sites and p-type N dopants (pyridinic) responsible for OER (**Figure 1-6d**).[91] Unfortunately, due to the inevitable carbon corrosion and oxidation in alkaline electrolyte, these materials often show inferior durability. As indicated in **Figure 1-6c**, a rapid enlargement in voltage gap was reflected in the first several hours of repeated discharge and charge.[92]

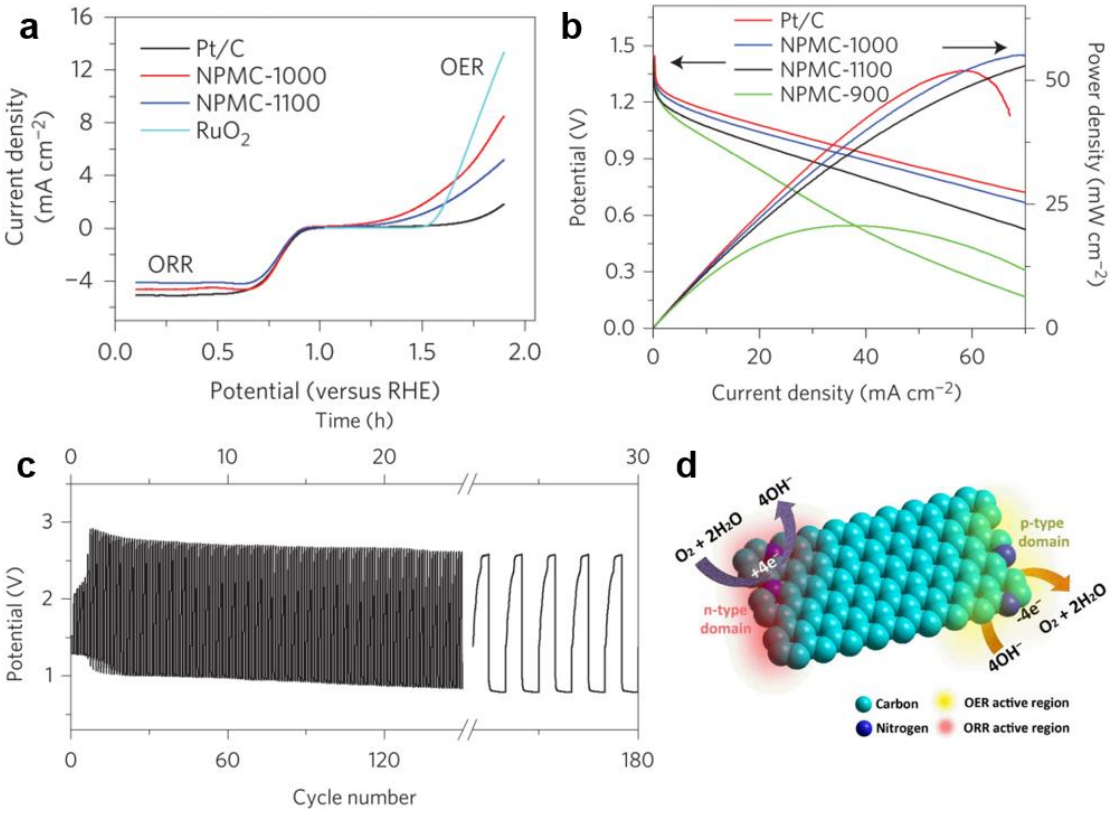

Figure 1-6 (a) Bifunctional acivity, (b) polarization and power density curves of N-doped carbon material with Pt/C and RuO_2 as the perofmrnace benchmark; (c) cyling performance of coin-type Zn-air battery using NPMC-1000. Reproduced with

permission from ref[90]. Copyright 2015 Nature Publishing Group. (d) Schematic illustruation of ORR and OER process at different N dopants. Reproduced with permission from ref[91]. Copyright 2016 American Association for the Advancement of Science.

1.4.1.2 Metal compounds

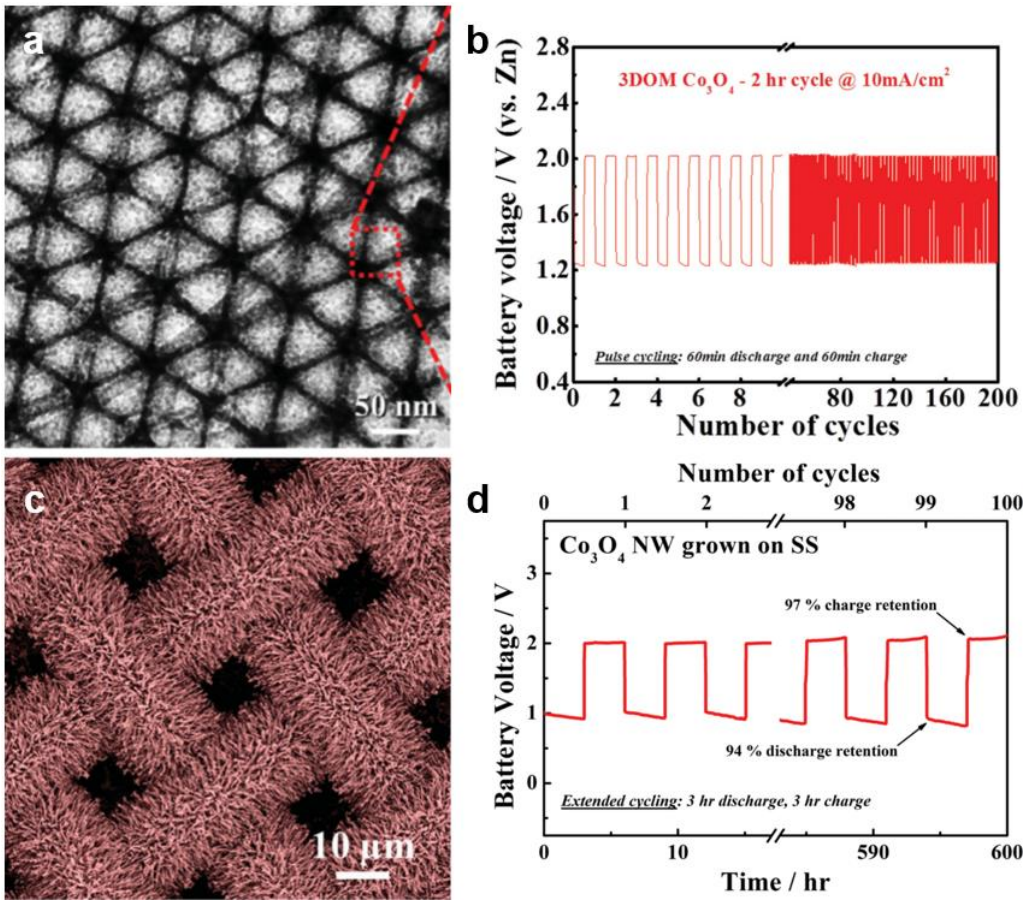

Figure 1-7 The morphologies and cycling profiles in Zn-air batteries of (a, b) 3DOM Co_3O_4 and (c, d) Co_3O_4 nanowires on stainless steel mesh. Reproduced with permission from refs[93, 94]. Copyright 2014 and 2016, John Wiley Sons, Inc.

The metal compounds mainly include alloys, spinel and perovskites oxides and their derived phosphides, carbides, sulfides, and nitrides.[95-101] The recent reports on metal compounds are summarized in Table 1-2. In comparison to carbon materials,

studies on metal oxides usually report decent stability and long period operations in Zn-air batteries. **Figure 1-7a** is a typical example regarding the synthesis of 3D ordered mesoporous (3DOM) Co_3O_4 and its utilization as bifunctional electrocatalyst in Zn-air battery.[93] When cycling at a current density of 10 mA cm^{-1} with a cycling period of 2 hours, it demonstrated a stable cycling for over 200 cycles (400 hours, **Figure 1-7b**). Another example in **Figure 1-7c** exhibited Co_3O_4 nanowire arrays grown on stainless steel mesh, which performed a cycling lifetime of 600 hours at .[94] However, due to the semi-conductive nature, their bifunctional activity is relatively mediocre.

1.4.1.3 Metal-carbon hybrids

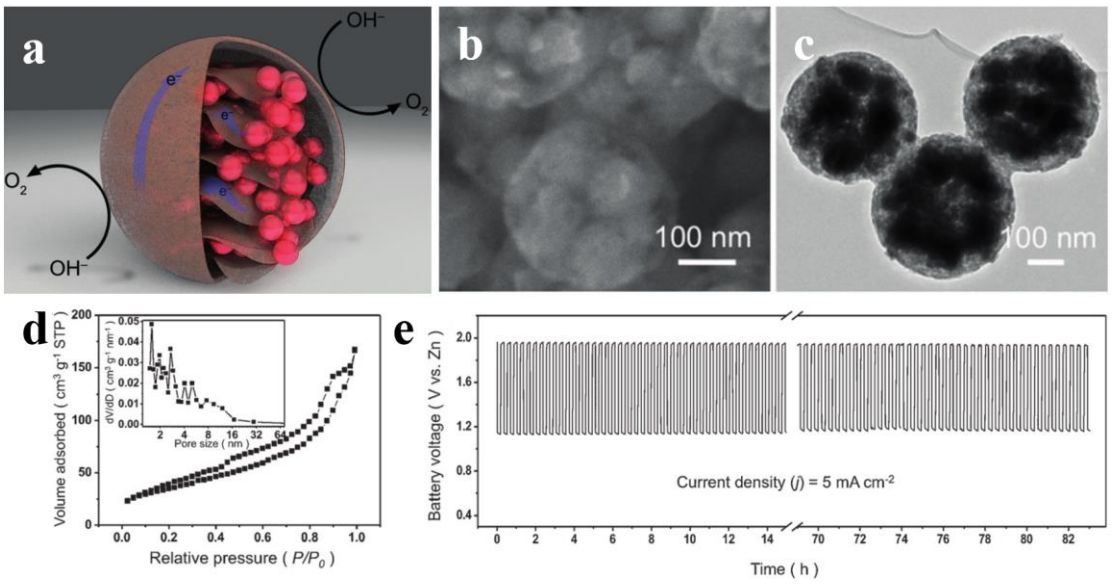

Figure 1-8 (a) Schematic illustration, (b, c) morphology and (d) porosity distribution of the Co_3O_4 nanocrystals embedded in a nitrogen-doped partially graphitized carbon framework with unique pomegranate-like composite architecture; and (e) its galvanostatic charge–discharge cycling performance of rechargeable ZABs. Reproduced with permission from ref[102]. Copyright 2016, John Wiley Sons, Inc.

The rational combinations between carbon and metal compounds have drawn massive research efforts since a pioneer work on core-corona structured $LaNiO_3$

supported N-doped carbon nanotubes (NCNT) for Zn-air batteries.[103] The synergetic effects between the two components endow higher active sites abundancy, conductivity and structural stability than each of the single counterpart.[102, 104-106] There are three different combination modes for these metal-carbon hybrids. Specifically, the first one is physically mixing metal components with carbon materials,[107] the second is carbon coated metal particles,[108-110] and the last is metal components dispersed outside carbon materials.[111] **Figure 1-8** shows an example of N-doped carbon coated Co_3O_4.[102] Several superiorities were demonstrated by this pomegranate-like nanostructure: low dimensional Co_3O_4 seeds serve as active sites for electrochemical reactions; self-accumulation of those nanosized particles is inhibited by the pomegranate-like structure; the high porosity provide additional pathways for mass transfer (**Figure 1-8d**); partially graphitized carbon shell is beneficial for boosting electrical conductivity and structural stability. As a result, an excellent performance in terms of low voltage gap and stable cycling was demonstrated in Zn-air batteries (**Figure 1-8e**).

1.4.2 Design principles

Oxygen electrocatalysis is a complex process, and many factors of electrocatalysts greatly influence their performance, such as electrical conductivity and hydrophilicity at triple-phase interface *etc*.[112, 113] However, for constructing an ideal bifunctional oxygen electrocatalyst, two general design principles are usually followed as indicated in **Figure 1-9**, which includes the maximizing active sites exposures and optimizing intrinsic activity.[79, 114] The first direction is often achieved by morphological designs aimed to expand surface area and amend pore channels.[103, 115] On the other hand, the intrinsic activity of active sites heavily depends on their electron configurations, which can be tuned by various methods such as defect engineering and

multi-element incorporation *etc*.[106, 116, 117] These two strategies and recent research progress will be expanded in this section.

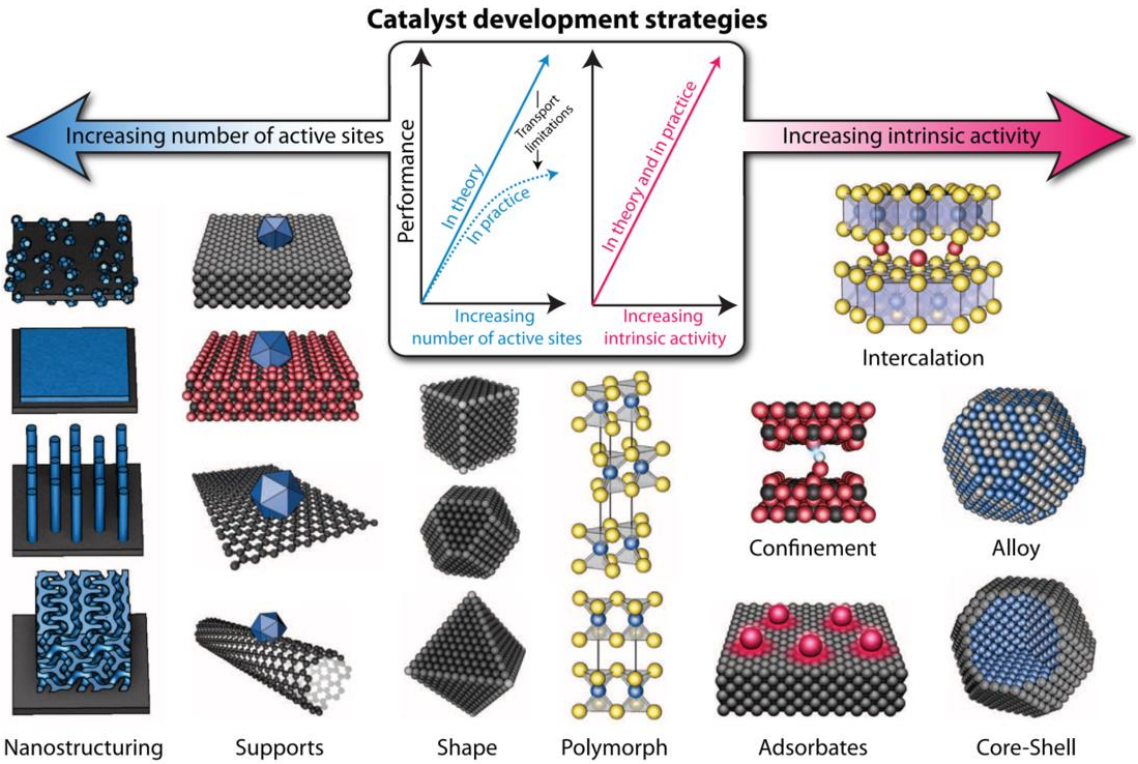

Figure 1-9 The shematic of desgin principles for electrcatalyst. Reproduced with permission from ref[114]. Copyright 2017 American Association for the Advancement of Science.

1.4.2.1 Increasing the number of Active Sites

The oxygen-involved cathode reactions of rechargeable Zn-air batteries are heterogeneous electrocatalysis occurred at the triple-phase boundary regions as illustrated in **Figure 1-10a**, *i.e.* O_2 gas, liquid electrolyte and solid electrocatalyst.[79] Increasing the surface area and porosity not only raise the number of active sites, but also improve the accessibility of the active sites and accelerate mass transfer due to the widened diffusion channels for oxygen species.[118] Therefore, structural engineering on materials at nanoscale exhibits great potential in producing highly efficient and durable

bifunctional oxygen electrocatalysts for rechargeable Zn-air battery. **Figure 1-10b** is an example regarding porosity engineering on carbon materials.[89] By taking advantage of silica sphere as the hard template, the hierarchical porosity (**Figure 1-10c**) was introduced into carbon framework after template removal. The hierarchical porosity, *i.e.* co-existence of micro-, meso- and macropores, is considered as the optimal for heterogeneous electrocatalysis. The different pores play different roles: the micropores increase number of active sites while the meso/macropores accelerate reactant transfer toward/away from the reaction locations. Another example is about 3DOM Co_3O_4 with a higher surface area and more pores than the bulk counterpart, and hence an improved electrocatalytic activity and battery performance was obtained.[93] Meanwhile, these secondary structures also ensure excellent structural stability during cycling.[102, 119] On basis of this principle, a great number of literatures have emerged and investigated the effectiveness of nanostructure on bifunctional electrocatalytic performance, such as core-corona structured $LaNiO_3$-NCNT, human hair emulated Co_3O_4-NCNT, pomegranate–like Co_3O_4 on N-doped carbon, "ship in a bottle" designed CoS_2 inside Ketjen Black carbon and $NiCo_2O_4$-rGO nanosheets, *etc*. [102, 105, 120-122]

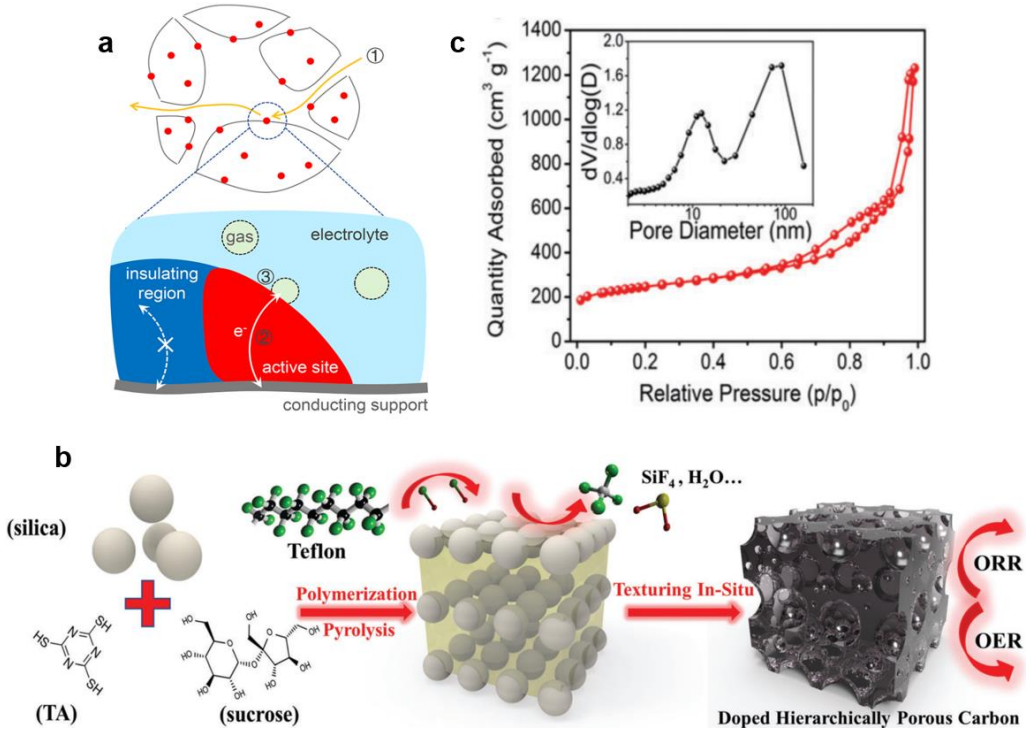

Figure 1-10 (a) Schematic representation of the gas-involving electrocatalysis. Three critical steps are coupled with each other, including (1) mass diffusion, (2) electron transfer, and (3) surface reaction. Reproduced with permission from ref[79]. Copyright 2018 American Chemical Society. (b) Schematic synthesis, (b) N_2 isotherms as well as pore size distribution of hierarchically porous carbon. Reproduced with permission from ref[89]. Copyright 2016 Royal Society of Chemistry.

1.4.2.2 Boosting the intrinsic activity

It is widely accepted that the rational modulation of electronic structure can positively influence the intrinsic activity of individual sites, that is to say, tuning electrocatalytic efficiency of active sites.[79] Also taking N-doped carbon as a demonstration. As discussed above, there are pyridinic, quaternary, pyrrolic and oxidized N as four types of dopants. Among them, the quaternary N at the edge of carbon can decrease the OOH intermediate adsorption energy by redistributing charges in the π–conjugated system, so that it is considered as the most active site for ORR.[91]

While OER activity relies on the pyridinic N because it promote adsorption of OOH* and O* intermediates on its adjacent C. Another example regarding electronic engineering is shown in **Figure 1-10**, it is a representative work that improved intrinsic activity through interpenetrating spinel Co_3O_4 and metallic Co within "Janus" particles.[123] The boundary between the two phases provided an interface with defect-rich feature that was beneficial for trapping oxygen reactants, while the metallic Co greatly improved the overall charge transfer kinetics. With these merits, this electrocatalyst outperformed single-phase counterparts in battery performance, and achieved an operation span over 800 h at 10 mA cm^{-2}.

The composition alteration on metal compounds is also a feasible strategy to boost intrinsic activity. Xu *et al.* demonstrate that ORR/OER intrinsic activity is determined by the percentage and valency of Mn at the octahedral sites in spinel $Mn_xCo_{3-x}O_4$.[76] Multi-element incorporation is also illustrated in a ternary Fe/Ni/Co electrocatalyst which showed higher bifunctional activity than its unary or binary counterparts.[124] Another effects of composition alteration is on the overall electrical conductivity of electrocatalysts. For example, Ni substitution into Co_3O_4 was reported to improve ORR activity due to the enhanced electrical conductivity of spinel lattice.[125]

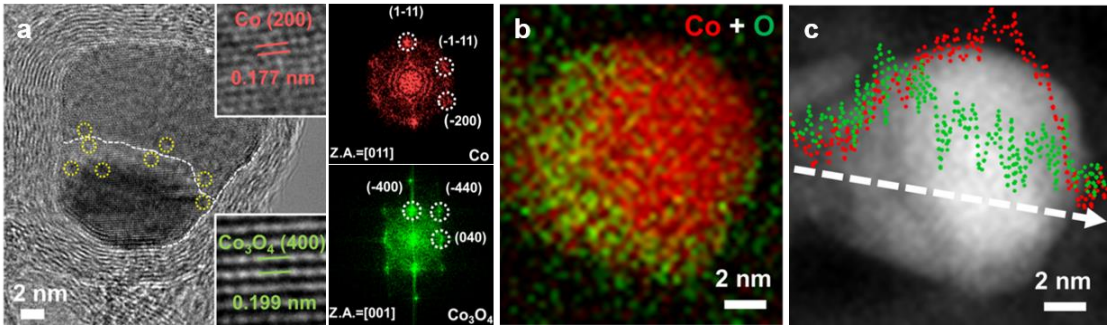

Figure 1-11 (a) High-resolution transmission electron microscopy (HRTEM) images and corresponding fast Fourier transformation patterns; (b) electron energy loss spectroscopic (EELS) elemental distribution and line scan of "Janus" Co/Co_3O_4@PGS

electrocatalyst. Reproduced with permission from ref[123]. Copyright 2018, John Wiley Sons, Inc.

1.5 Research objectives

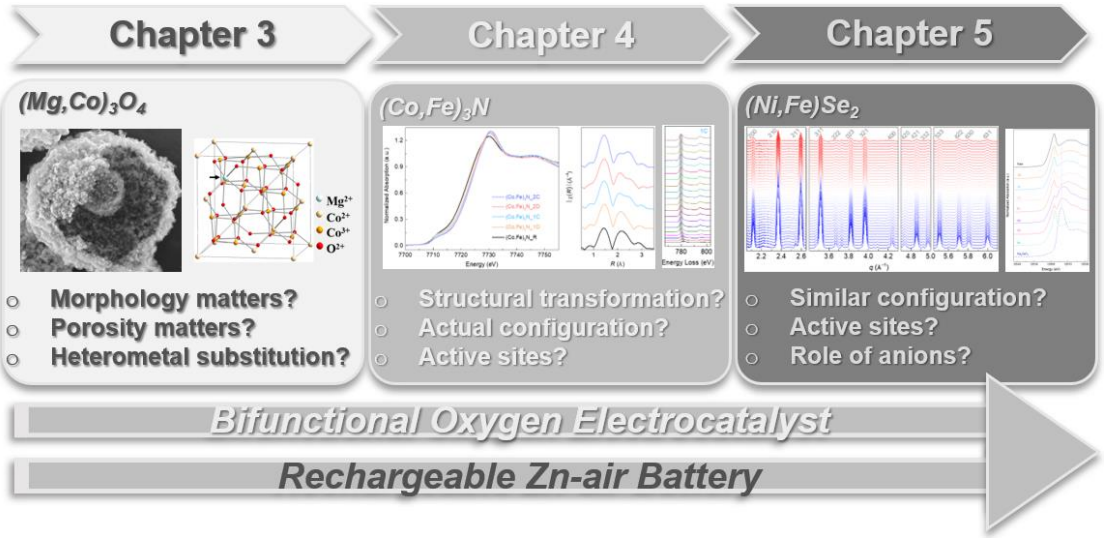

Figure 1-12 The research uncertainties aimed to address throughout this thesis.

As indicated in **Figure 1-12**, the main objective of this thesis is to address several uncertainties regarding materials designs and electrochemical behaviors of bifunctional oxygen electrocatalyst, i) how to amend the porous channels in electrocatalyst though nanostructure engineering, ii) what the role of different metals is in multi-metal compounds as electrocatalyst, iii) whether the raw states of electrocatalyst preserve during Zn-air battery operation, vi) what the actual configuration and active species of electrocatalyst are during battery cycling, and v) whether the anionic elements are inactive for oxygen electrocatalysis. In this thesis, several metal-based electrocatalysts with different nanostructures have been designed and characterized in detail though the combination of various techniques to provide answers and solutions to above uncertainties. With those results, I expect to obtain some fundamental understandings

on materials design and the structural evolution underlying electrochemical behaviors, and also get some new insights into origin of performance difference.

1.6 Structure of thesis

This thesis is organized into six chapters. **Chapter 1** introduces the general background, history, recent research progress on each battery component of Zn-air battery, and motivation of the thesis. **Chapter 2** presents various characterizations and electrochemical measurement techniques adapted throughout the thesis, with more details provided within experimental section of subsequent chapters. In **Chapter 3**, an in-situ coordinating strategy is introduced to fabricate hierarchical porous double-shelled electrocatalyst, and the effects of Mg substitution on electrocatalytic activity of spinels are also studied. **Chapter 4** studied the electrochemical behavior and structural evolution of metal nitrides during Zn-air battery cycling. With the concept of dynamic electrocatalyst, a "core-shell" configuration with a newly generated oxyhydroxide shell as the active species is observed, and periodic valence swings of performance-dominant element are detected within the active shell. **Chapter 5** focuses on the role of anionic element in battery cycling by using a bimetal selenide. Besides the observation of the similar actual configuration and the periodic valence swings with nitrides, selenium is oxidized under battery operation, which is considered as the reason for the superior performance of bimetal selenide to its alloy counterparts. Lastly, in **Chapter 6**, a summary of important results and some suggestions for future studies on bifunctional electrocatalyst for rechargeable Zn-air batteries are provided.

2 Chemicals and Characterization Techniques

In this chapter, the basic principles and mechanisms of key techniques adopted to characterize the morphological and physicochemical properties of electrocatalysts are described, while the electrocatalytic evaluation based on three-electrode systems and Zn-air battery measurements are also provided. The materials preparation procedures and the detail techniques will be described in the section of Experimental methods of following three chapters.

2.1 Physical characterization

2.1.1 X-Ray diffraction analysis

As an X-ray derived analytic technique, X-ray diffraction (XRD) is established based on Bragg's Law as indicated in **Figure 2-1a**. A beam of incident X-ray goes inside the crystal and causes diffractions into many specific directions. By recording the degree and the intensity of diffracted X-rays, the diffraction patterns with crystal information can be observed. Then, when referring to the standard patterns, the space group and the miller index of each diffraction peak can be identified. According to the different X-ray sources, XRD is usually divided into two categories. The first one is lab-source diffractometer as shown in **Figure 2-1b**, which usually utilized Cu Kα as the radiation source. During measurement, either the sample holder or the director continuously rotates to observe the diffraction intensity at different degrees. The second category is based on the synchrotron source. **Figure 2-1c** is an example at Brockhouse X-ray Diffraction and Scattering Beamlines (BXDS-WHE) of Canadian Light Source (CLS). The energy for diffraction is relatively high, so it is named as high-energy XRD (HEXRD) or synchrotron XRD (SXRD). Two-dimensional (2D) diffraction images are

usually obtained in transmission mode. After being calibrated by the standard reference, such as LaB_6 or CeO_2, those images can be converted into 1D curves with crystal information. In comparison to lab-source XRD, SXRD is capable to provide higher resolution within a wider diffraction window, and it is also much more efficient. Generally, it takes less than 1 min per pattern, which opens up the possibility to record the rapid phase evolutions in a narrow time interval. As for the demonstration of XRD applications in battery related studies, two cases will be discussed in the following parts, involving the typical crystal identification and in-situ experiments combined with electrochemical potentiostatic.

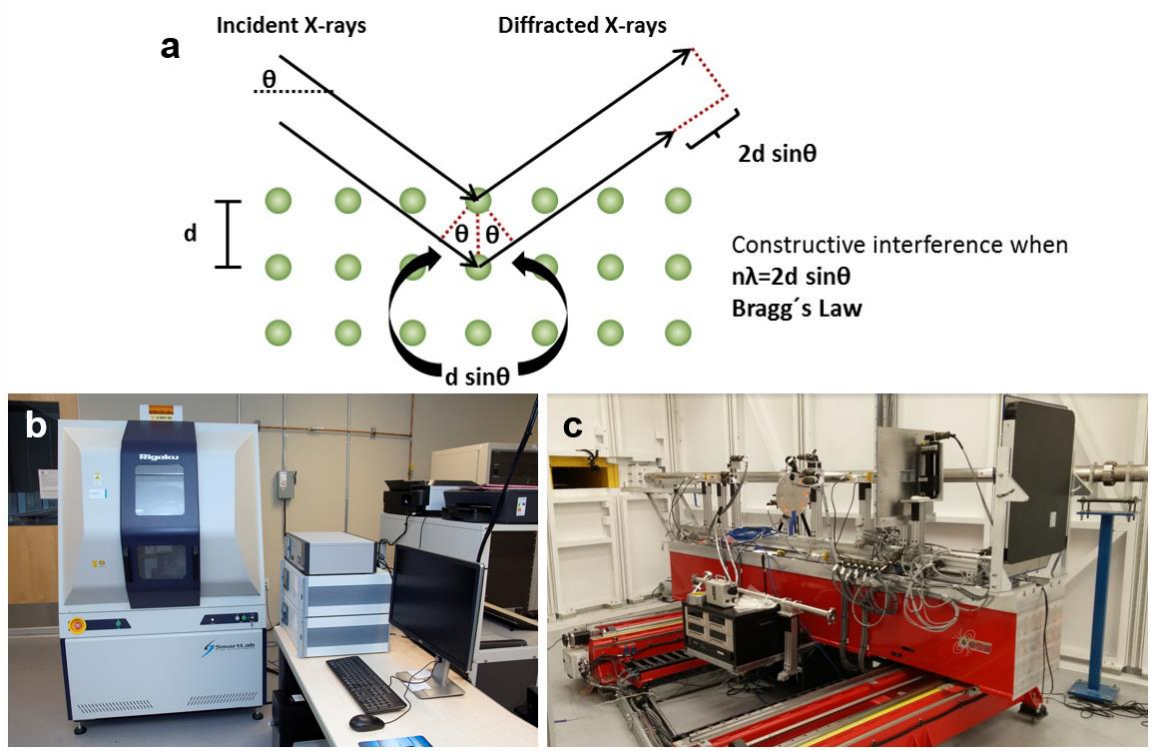

Figure 2-1 (a) The schematic of XRD mechanism and the Bragg's Law. The photographs of (b) lab-source Rigaku diffractometer with Cu Kα radiation (1.5406 Å) and (c) synchrotron-based diffraction in transmission mode at Brockhouse X-ray Diffraction and Scattering beamlines (BXDS-WHE) of CLS.

2.1.2 X-ray adsorption spectroscopy

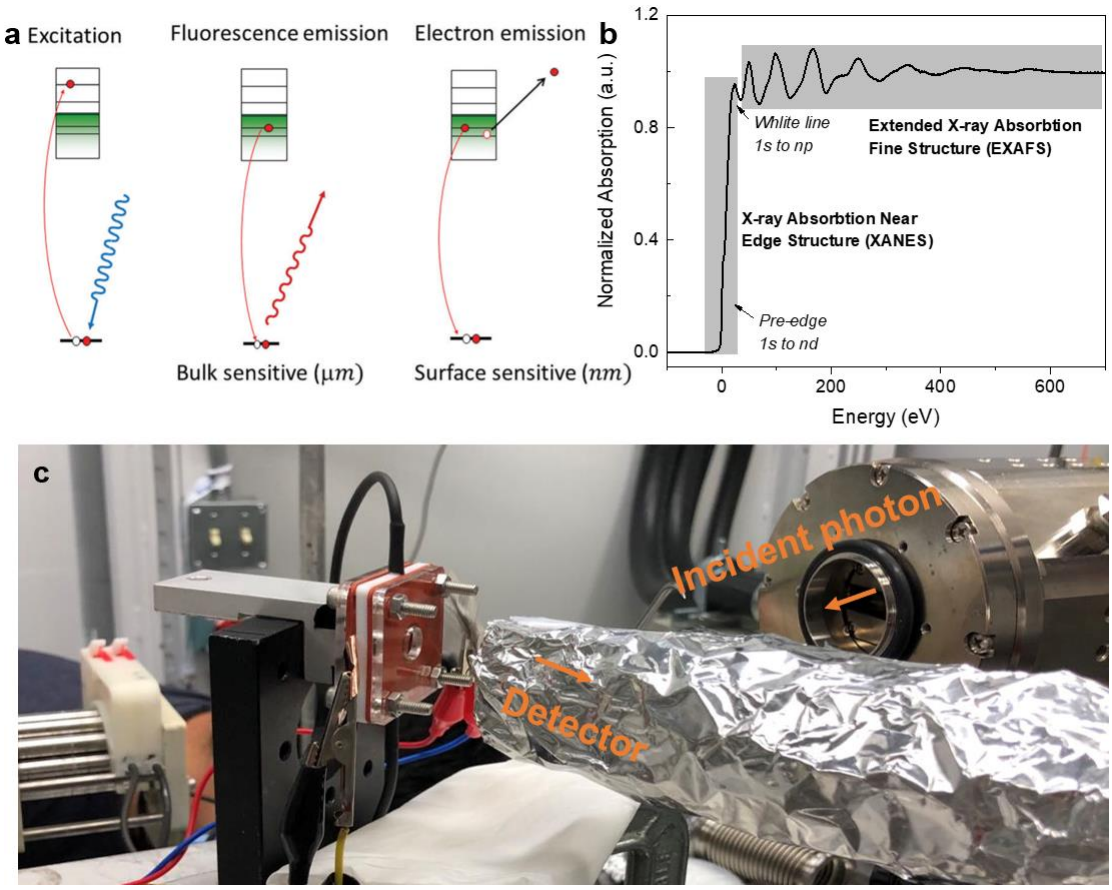

Figure 2-2 (a) The schematic illustration of X-ray excitation, fluorescence and electron emission probe manners. Reproduced with permission from ref[126]. Copyright 2017 Royal Society of Chemistry. (b) A typical XAS spectrum and (c) the photograph of operando setup for XAS experiments at Soft X-ray Microcharacterization Beamline (SXRMB, 06B1-1) of CLS.

X-ray absorption spectroscopy (XAS) is based on synchrotron radiation facility, such as Canadian Light Source (CLS). As shown in **Figure 2-2a**, the core electron of element is excited to an unoccupied orbital by incident photon at a specific energy range that is element-selective. By detecting the transmission X-ray, generated fluorescence, or electron emission, the XAS curve can be observed as indicated in **Figure 2-2b**, which is usually divided into two regions as X-ray absorption near edge structure (XANES)

and extended X-ray absorption fine structure (EXAFS).[126] According to the different observation manners, three detection modes are accessible in XAS experiments, i.e. transmission, total fluorescence yield (TFY) and total electron yield (TEY). In comparison to the bulk information gathered by transmission and TFY, TEY focus on the surface information in the range of several nanometers and requires a reasonable conductivity of sample stage for electron transfer. By deciphering the XANS curves of a specific element, a wide range of chemical information, including electronic structure, oxidation state and coordination, can be obtained.[127] Usually, commercial metal foils and metal oxides with known valence states are also measured and used as standard references. As for the EXAFS region, the Fourier transformation (FT) of k-space is usually utilized in EXAFS analysis to general R-space and provide the bond environment at atomic scale. After the peak fitting on R-space, the diffusion pathway as well as the coordination numbers of center element can be obtained.

Another advantage of XAS technique is its compatibility on other equipment, such as electrochemical workstations.[128, 129] As such, the *operando* experiments can be conducted to get the real-time evolutions of chemical information under electrochemical conditions. **Figure 2-2c** is a typical demonstration of operando setup for a Zn-air battery. As shown, the homemade Zn–air battery prototype can be adopted as the *operando* cell for XAS measurements. Usually, a hole is drilled onto the cell to let the incident photon go through, so that the spectra can be recorded on either transmission or TFY mode. Due to the presence of the other battery components, such as the PMMA or Teflon cell, and electrolyte, the TEY mode is generally inaccessible for *operando* experiments. By detecting the XAS curves at specific time intervals, the chemical evolution can be recorded to understand the electrochemical behaviors.

2.1.3 X-Ray photoelectron spectroscopy

X-ray Photoelectron Spectroscopy (XPS) is another X-ray based photoemission technique, and it is a quantitative tool to analyze the surface chemistry of samples. It can be used to identify of elemental composition (**Figure 2-3a**) and determine the chemical and electronic states of each element (**Figure 2-3b**). XPS is built on the principle of photoelectric effect which describes the phenomenon of electron emission from a solid medium by photon radiation and introduces the idea of Wave–particle duality. Using this principle, the measured kinetic energy of the ejected electrons can be related to their binding energy in the atomic orbitals. Since each element have a characteristic set of binding energies, the elements in a material can be identified by simply comparing the measured spectrum to the known reference. Furthermore, since binding energies may different due to presence of chemical bonds or variation in oxidation states, shifting of the characteristic peaks can also provide useful information of chemical and electronic states of the elements.

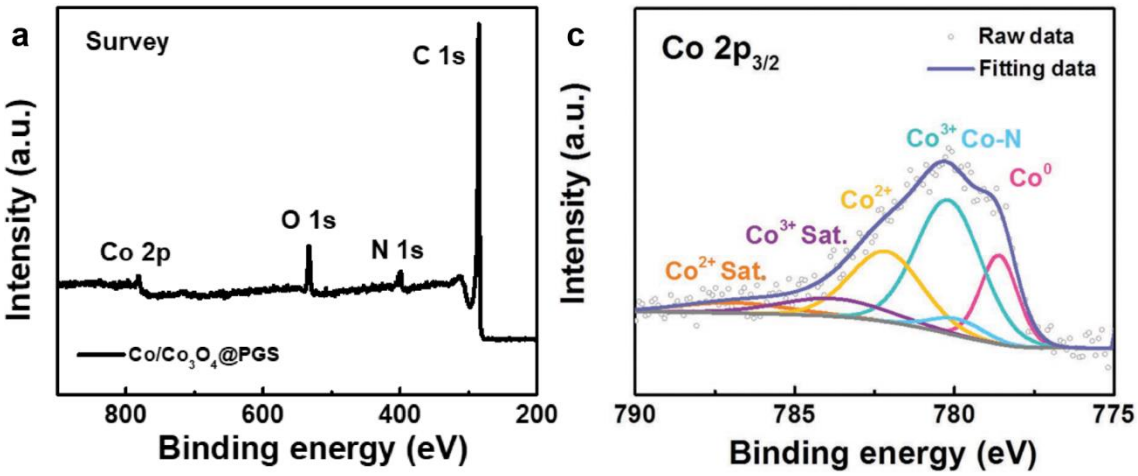

Figure 2-3 (a) The XPS survey spectrum shows the presence of Co, O, N, and C in the electrocatalyst, and (b) high-resolution Co 2p3/2 spectra indicates different Co species. Reproduced with permission from ref[123]. Copyright 2018, John Wiley Sons, Inc.

2.1.4 Scanning electron microscopy

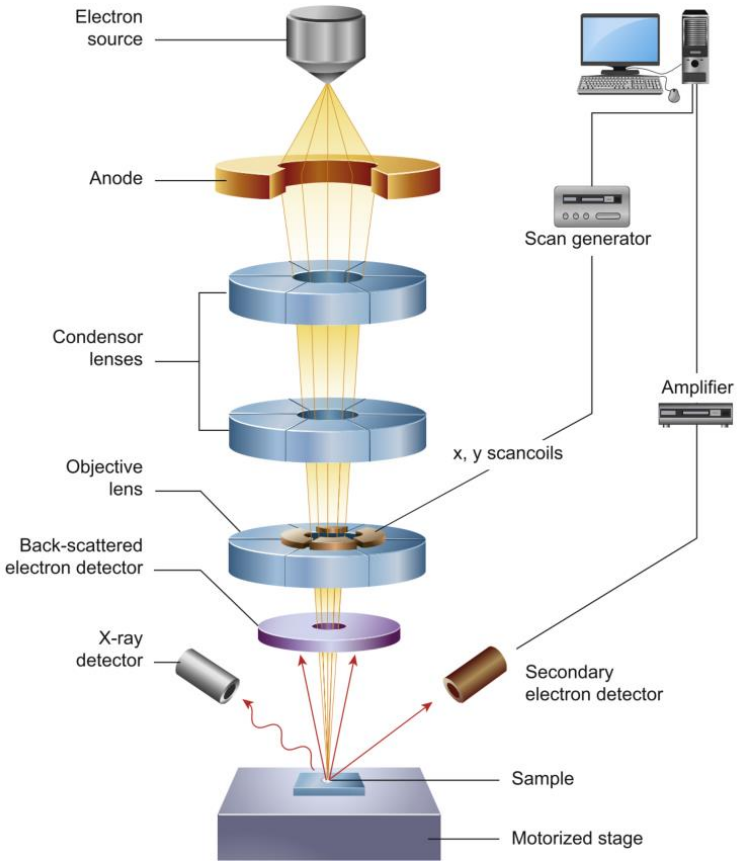

Figure 2-4 The schematic illustration of core components and working principles of SEM. Reproduced with permission from ref[130]. Copyright 2016, Elsevier.

Figure 2-4. exhibits a typical layout inside the Scanning Electron Microscopy (SEM) microscope. The electrons are first stimulated at electron guns and accelerated by electric field, which is usually in the range of 5 to 20kV, within high-vacuum environment onto samples. Then, by monitoring the signals (mainly including the secondary electrons, back scattering electron, characteristic X-ray and cathodoluminescence) emitted from samples using different lens, the surface structure and morphology of samples can be characterized in a high-resolution manner (~10 nm). In a typical SEM image, the electron signals of interest regions are turn into current,

and the brightness of the image reflects the intensity of the current. In this thesis, the SEM images in this thesis were collected using a FEI Quanta FEG 250 ESEM or Zeiss ULTRA plus Field Emission SEM.

2.1.5 Transmission electron microscopy

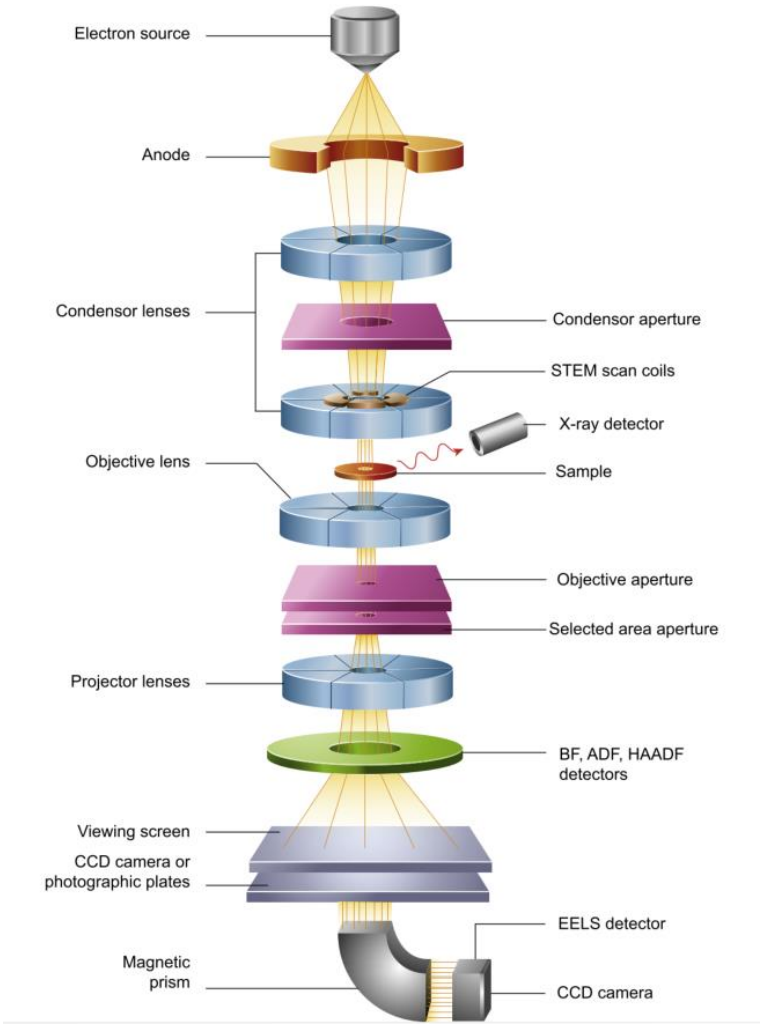

Figure 2-5 The schematic illustration of core components and working principles of TEM. Reproduced with permission from ref[130]. Copyright 2016, Elsevier.

Transmission Electron Microscopy (TEM) microscopes have similar components (**Figure 2-5**) with SEM but usually operate at much higher voltage from 200 to 300 eV, and therefore the atom arrangements and lattice fringes are usually detectable. Because of the transmission-probing manner, TEM provides information

about interior structure and compositions with very high resolution, rather than surface of the sample for SEM. Besides, as shown in **Figure 2-5**, TEM microscopes usually incorporated with a wide range of lenses or detectors, so that energy dispersive X-ray spectroscopy (EDS), selected area electron diffraction (SAED), or electron energy loss spectrometry (EELS) can also be measured to reflect the elemental composition/distribution, structural and chemical features of samples. Besides these common techniques, another specific TEM based technique adopted in this thesis is the 3D tomography.

In this thesis, TEM results were mainly obtained from several microscopes, including JEM-2010F microscope, JEM-3200FS microscope, FEI Titan 80-300 LB microscope and FEI Titan 80-300 HB microscope with a double aberration correction. As for the sample preparation, the powders were first dispersed in ethanol under ultrasonication and then drop casted onto an amorphous carbon coated copper mesh. Regarding the 3D tomography, a rotatable sample holder is used to load the copper mesh with samples. A series of STEM images are taken within a wide tilt range (such as -70^{o} to 70^{o} with an increment of 2^{o}). Then, by using the software (Aviso package is employed in this thesis), these 2D images can be reconstructed to visualize the morphology either at different rotation degrees or different depths.

2.2 Electrochemical characterization

2.2.1 Galvanostatic tests

Galvanostatic cycling is carried out on a battery tester (LAND-CT2001A) to measure the electrochemical performance of Zn-air battery by applying constant current, in terms of charge/discharge voltage and life span for cycling. The Zn-air battery can be fabricated following the protype in **Figure 1-3a**. In a typical fabrication,

the sample powders are dispersing within 0.2 wt% Nafion solution to form electrocatalyst ink, which is sprayed onto a carbon paper as the gas diffusion layer (GDL, the mass loading of electrocatalyst is fixed as 1 mg cm^{-2} in this thesis). Then, this GDL as air cathode is assembled with polished zinc plate as anode to form Zn–air battery, in which 6M KOH solution dissolved with 0.2 M $Zn(CH_3COO)_2$ is filled as electrolyte in this thesis. The stain-less mesh and copper foil are used in this thesis as the current collector at cathode and anode side, respectively. By recording the charge and discharge profiles with a fixed time interval (such as 2 hours cycle period), the cycling performance at a specific areal current density can be obtained. Besides setting the galvanostatic current, a cut-off voltage is usually added to avoid overcharge on Zn-air battery. As shown in **Figure 1-5d**, two sets of parameters are commonly considered as the criterions in performance comparison, *i.e.* discharge-charge voltage gap and cycling number. The previous one can be also expressed as the energy efficiency (*i.e.* the ratio between discharge and charge voltage) and is related to the activity of electrocatalyst, while the latter is regarding its durability under battery operation.

2.2.2 Galvanodynamic tests

The galvanodynamic measurement is conducted on a Gamry electrochemical workstation, which allows investigation of charge and discharge behaviors at different current density. Briefly, by increasing the current density from 0 mA cm^{-2} up to a cut-off value with a fixed rate (such as 1 mA cm^{-2} s^{-1}), the changes in the battery operation voltage are recorded and plotted as a function of current density. **Figure 1-5b** is a typical illustration for charge and discharge polarization curves, in which the overall overpotential at a specific current density can be identified as the basis in performance comparison. As another key battery parameter, the power density of Zn-air battery is also calculated based on discharge polarization curves (**Figure 1-5c**).

2.2.3 Electrocatalytic tests

The electrocatalytic measurement is established based on three-electrode systems using rotating disc electrode (RDE) as the working electrode, a saturated calomel electrode (SCE) as the reference electrode and a graphitic rod as the counter electrode. Oxygen/nitrogen saturated 0.1 M KOH aqueous solution is usually applied as the electrolyte. Prior to the measurement, the catalyst ink is drop deposited onto the glassy carbon disc of RDE. The graphitic rod is utilized to complete the current circuit, while the SCE allows to record electrode potential, which is then calibrated to a reversible hydrogen potential (RHE) based on Nernst equation.

In a typical measurement of ORR, the potential of the working electrode is swept from *ca.* 0 to 1 V (*vs.* RHE) with a scan rate of 10 mV/s within O_2 saturated electrolyte. The electrode is continuously rotated (*i.e.*, at 1600 rpm) to induce convective electrolyte flow and ensure a steady supply of O_2 saturated electrolyte towards the catalyst layer. Background (capacitive) currents obtained under N_2 saturated conditions will be removed to account for the solely Faradaic ORR. Then, the ORR pathway is determined by calculating the number of transferred electrons, which allows the quantitative kinetics comparison. The number of transferred electrons is calculated by a Koutecky–Levich (K–L) plot.[131] As for OER activity, it is usually measured from *ca.* 1 to 2 V with a scan rate of 10 mV/s. The ORR/OER overpotential is defined by the difference between $E°(OH^-/O_2)$ = 1.23 V and the measured potential. The Tafel slopes are calculated based on Tafel equation

3 Hierarchical Porous Double-Shelled Electrocatalyst with Tailored Lattice Alkalinity toward Bifunctional Oxygen Reactions

3.1 Introduction

As discussed in Chapter 1, the hybrid catalysts of metal oxides composited with carbon-based materials have drawn the major research attentions in Zn-air battery studies.[102] Among the hybrids, the spinel oxides, especially cobalt-based oxides, are explored to be decent OER electrocatalysts in spite of their inefficient ORR activities.[76, 132, 133] Meanwhile, the excellent ORR activities have been achieved on carbon materials via heteroatom doping, such as N, S, P *etc.*[134-136] Owing to the synergic effects of the above two components, reasonable bifunctionality and durability are usually demonstrated.[102, 121, 137]

There are two general modification strategies for these hybrid electrocatalysts. On the one hand, morphological tuning on electrocatalysts to expand porosity and active sites availability is the most effective strategy to optimize oxygen electrocatalysis. In recent decades, multi-shelled micro-structured metal oxides with unique hollow architecture and large surface area have been developed for different applications.[138-142] Theoretically, those hollow materials can enhance the accessibility of electrolyte and reactants. However, they are never applied as bifunctional oxygen electrocatalyst for metal-air batteries since their limited porosity hinders efficient oxygen reactions. It means if hierarchical porosity is introduced into multi-shelled materials, their electrocatalytic sites abundancy would be improved drastically. Such open system is also beneficial for mass transfer of oxygen species, *i.e.* OH^-, O_2, and H_2O.[118] The hard-

template method is the most commonly adopted to synthesize multi-shelled metal oxides. It usually contains tedious steps, including carbonaceous template preparation, repeated cation adsorption, and template removal. During the repeated cation-adsorption process, the interconnection between the metal cations and the negative charged template surface is mainly driven by electrostatic attraction, while the empty *d* orbits of transition metal ions can also be occupied by *p* electrons of oxygen-involved functional groups on hydrophilic surface of carbonaceous microspheres.[138] Since so, the metal cations densely gather on the hydrophilic surface, and rarely penetrate into the carbonized core of template.[143] Upon gradual removal of the carbonaceous template, metal oxides will form into shells with very limited porosity. In contrast, if the metal ions are uniformly distributed within carbonaceous template, pore-rich multi-shelled metal oxides may be produced. Therefore, a general and feasible blueprint to synthesize multi-shelled materials with hierarchical porosity is highly desirable for the development of exceptionally efficient electrocatalysts for metal-air batteries.

Another strategy focuses on modifying the intrinsic electrocatalytic activity of spinel cobalt-based components in hybrids. The incorporation of transition-metal ions, *e.g.* Zn, Mn, and Ni, with tunable chemical state is commonly adopted.[76, 144, 145] Alternatively, with the aim to expedite their poor intrinsic ORR activity, the controlled substitution of metal ions with low hydroxyl coordination capability, such as Mg^{2+}, should also be an effective approach. Since Mg-substitution would create buffer zones with weakened lattice alkalinity, and hence facilitate the extraction of ORR resultants (OH^-) away from active sites. However, previous attempts in increasing oxygen electrocatalysis of Co_3O_4 via Mg-substitution have never been successful in spite of the boosted electrical conductivity.[132, 146] The root cause of the failures are the excessive occupation of bivalence Mg that are inactive for oxygen electrocatalysis. Hence,

controllable occupation of Mg^{2+} at relatively low amount is the key factor to realize the insight of tailoring lattice alkalinity.

With the aim to realize the above hypotheses, a novel *in-situ* coordinating process is proposed in this chapter to synthesize double-shelled spinel (Mg, $Co)_3O_4$ with hierarchical pores (HP-DS) and controlled Mg^{2+} doping. The positive effects of Mg-modulation on spinel structure and electrocatalytic performance are studied. With the addition of a uniform layer of N-doped graphitized carbon (NGC) onto (Mg, $Co)_3O_4$, the final hybrid catalyst, signified as (Mg, $Co)_3O_4$@NGC, demonstrates feasibility as a bifunctional oxygen electrocatalyst for Zn-air batteries.

3.2 Experimental methods

Synthesis of HP-DS (Mg, $Co)_3O_4$. A one-step hydrothermal method was adopted to synthesize hierarchical porous and double-shelled hollow metal oxides. In a typical synthesis, 80 mL aqueous solution of 0.5 M $Co(NO_3)_2$, 0.25 M $Mg(NO_3)_2$, and 0.56 M glucose was sealed into a 100 mL Teflon container, and then hydrothermally reacted at 160 °C for 400 minutes. The brown precipitate was collected by filtration, washed with DDI and ethanol for several times, and dried at 80 °C in oven. The target products were generated through calcination in air at 500 °C for 60 minutes with a heating rate of 1 °C per minute. The pure Co_3O_4 were prepared following the same procedure without the addition of $Mg(NO_3)_2$. Other spinel metal oxides, such as (Mn, $Co)_3O_4$, (Ni, $Co)_3O_4$, (Mn, $Ni)_3O_4$, (Ni, Mn, $Co)_3O_4$ *etc.*, could be also prepared using the same synthetic route with different metal nitrates.

Synthesis of LP-QS (Mg, $Co)_3O_4$. Similarly, the quadruple-shelled hollow microspheres metal oxides (LP-QS) with limited porous surface were prepared using the method provided in the above section, but the metal nitrates are substituted with

metal acetates, *i.e.* $Co(CH_3COO)_2$, $Mg(CH_3COO)_2$, $Ni(CH_3COO)_2$, and $Mn(CH_3COO)_2$.

Synthesis of $(Mg, Co)_3O_4$@NGC. 50 mg of the as-prepared $(Mg, Co)_3O_4$ and 50 mg of dopamine hydrochloride were dispersed in 100 mL of 0.01 M tris(hydroxymethyl)aminomethane buffer solution. The solution was allowed to react under magnetic stirring for 5 hours at room temperature, and the black powders were collected by centrifugation. Following the isolation of the product, it was washed with DDI and ethanol several times, dried at 80 °C in oven, and then calcined at 500 °C for 0.5 h under NH_3 flows with a heating procedure of 1 °C min^{-1} in argon gas. Finally, the obtained sample was annealed at 150 °C for 6 hours in air to oxidize any metallic Co generated during the carbonization of polydopamine.

3.2.1 Materials characterizations

The morphology, energy-dispersive spectroscopy (EDS), and electron energy loss spectroscopy (EELS) were collected by scanning electron microscope (SEM; FEI Quanta FEG 250 ESEM) and transmission electron microscope (TEM; JEOL, JEM-2010F, 200 kV) equipped with an X-ray spectrometer detector. The 3D high angle annular dark field scanning transmission electron microscopy (HAADF-STEM) tomography was acquired by an FEI Titan 80-300 LB field emission TEM operated at 300 kV. STEM images were taken with a tilt range from −70 to 70° with an increment of 2°. The Inspect3D and Aviso software packages were employed to align, reconstruct and visualize the raw data. The chemical composition of the samples was determined by inductively coupled plasma atomic emission spectroscopy (ICP-AES; Perkin Elmer Ltd.). Nitrogen adsorption and desorption isothermal curves were measured on Folio Micromeritics ASAP 2020, and the surface area was calculated according to the

Brunauer-Emmett-Teller (BET) method. The pore size distribution was obtained from the adsorption branch using the Barrett-Joyner-Halenda (BJH) model. The structural features of synthesized samples were determined by X-ray diffraction (XRD; Rigaku Miniflex 600 X-ray Diffractometer), X-ray photoelectron spectroscopy (XPS; Thermal Scientific K-Alpha XPS spectrometer), and Raman spectra (WiTEC alpha300R Raman microscope) with an excitation line of 532 nm. All the XPS spectra were calibrated by taking 284.5 eV of C 1*s* peak as a reference.

3.2.2 Electrochemical measurements

Bifunctional electrocatalytic performance for ORR and OER was measured on an electrochemical workstation (Biologic VSP 300) with a three-electrode system and rotation speed controller (Pine Instruments Co., AFMSRCE). The working electrode is a glassy carbon (GC) electrode with an area of 0.196 cm^2, while a graphitic rod and saturated calomel electrode (SCE) were used as counter and reference electrode, respectively. The obtained data were calibrated to the reversible hydrogen electrode (RHE) based on Nernst equation ($E_{RHE} = E_{SCE} + 0.059 \times pH + 0.241$). 0.1 M KOH solution is adopted as the electrolyte; the iR-compensation was corrected based on the resistance of 40 ohm in 0.1 M KOH. To prepare the catalyst ink, 2 mg of material and 1 mg of Vulcan XC-72 carbon were dispersed in 500 µL of 0.15 wt.% Nafion ethanol solution by ultrasonication for 1 hour. Then, 15 µL of the formed homogenous ink was pipetted on GC with a catalyst loading of 0.3 mg cm^{-2}. O_2 was bubbled continuously during the ORR tests, and N_2 was used for OER tests. The commercial state-of-the-art noble-metal electrocatalysts, including Pt/C (20 wt.% Pt) and Ir/C (20 wt.% Ir), were adopted as ORR or OER benchmark with the same catalyst loading. The onset potential for ORR is defined as the potential when the current density reaches −0.1 mA cm^{-2}. While the ORR and OER overpotentials are calculated from the difference between

$E°(OH^-/O_2) = 1.23$ V and ORR half-wave potential or OER potential at 10 mA cm^{-2}, respectively. Lastly, the bifunctional activities are set as the sum of the ORR and OER overpotentials. The electron transfer number per oxygen molecule was calculated based on Koutecky-Levich (K-L) equation: $\frac{1}{j} = \frac{1}{j_k} + \frac{1}{B\omega^{1/2}}$, in which j_k is the kinetic current and B is Levich slope ($B = 0.2nFD_o^{2/3}C_o v^{-1/6}$; F is the Faraday constant; D_o is the oxygen diffusion coefficient of 1.9×10^{-5} cm^2 s^{-1}; C_o is the oxygen concentration of 1.1×10^{-6} mol cm^{-3}; v is the kinematic viscosity of 0.01 cm^2 s^{-1} in 0.1 M KOH).

The full-cell Zn-air battery tests were performed using home-made plastic prototypes containing a polished Zn-plate as anode and catalyst-sprayed gas diffusion layer (GDL; SGL Carbon 39 BC; Ion Power Inc.; active area of 1 cm^2; catalyst loading of 1 mg cm^{-2}) as air electrode. The space between the electrodes was filled with electrolyte of 6 M KOH and 0.2 M $Zn(CH_3COO)_2$. The catalyst ink was prepared by homogenously dispersing the electrocatalyst in 0.3% Nafion ethanol solution by ultrasonication. As for the reference, a mixture of commercial Pt/C and Ir/C (1:1 mass ratio) was also sprayed on GDL with the same loading and fabricated in full-cell Zn-air batteries. Rechargeability tests were carried out using a periodic galvanostatic method on a Land battery tester (LAND-CT2001A, Land Electronic Co., Ltd., Wuhan). All the battery experiments were conducted in ambient conditions using atmospheric air.

3.3 Results and Discussions

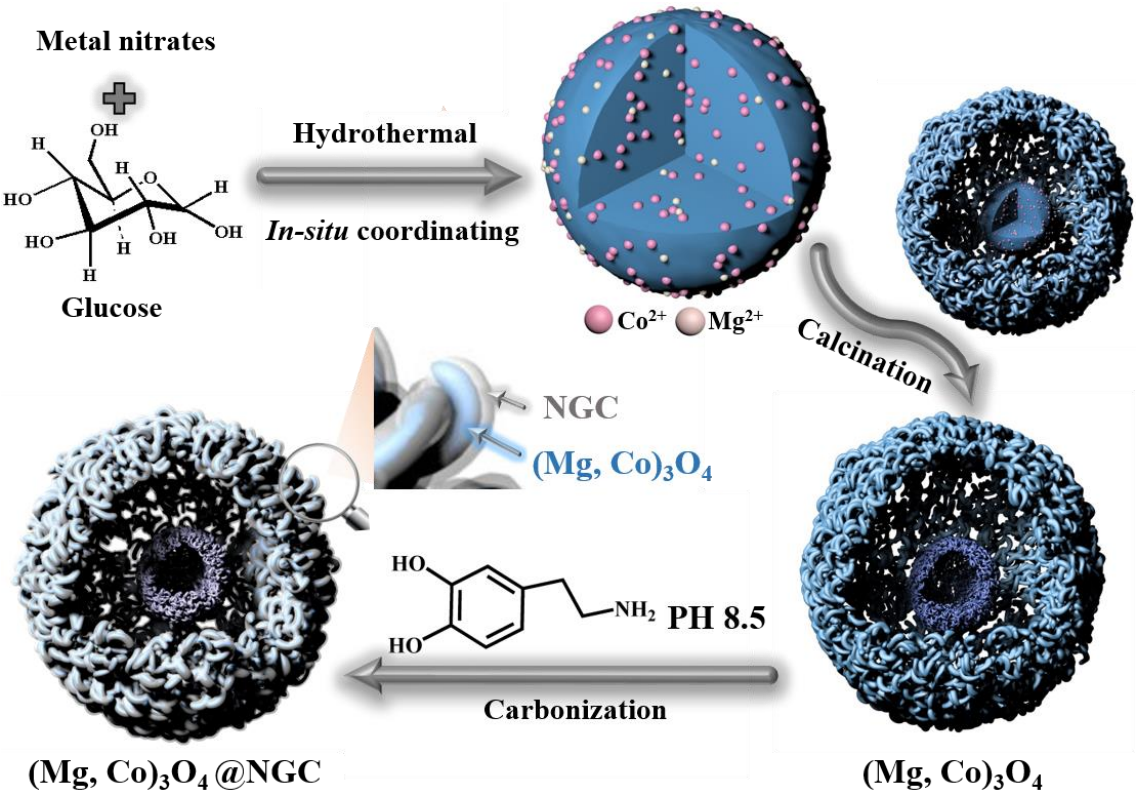

Figure 3-1 Schematic of the synthesis routes of HP-DS (Mg, Co)$_3$O$_4$ and (Mg, Co)$_3$O$_4$@NGC.

A one-step hydrothermal synthesis is presented here as illustrated in **Figure 3-1**. Firstly, a homogeneous solution of metal nitrates and glucose is sealed and heated in a Teflon reactor. During the gradual condensation of glucose under hydrothermal condition, the metal cations (Co^{2+} and Mg^{2+}) are adsorbed via an *in-situ* coordinating process that includes intermolecular condensation of glucose and simultaneous coordination with metal ions. These metal ions can then act as "bridges" to interconnect glucose, leading to the incorporation of metal cations within the carbonaceous microspherical frameworks. Moreover, there is a competition for free sites between Co^{2+} and Mg^{2+} throughout the *in-situ* coordinating process. Due to the filled 2*p* orbits of Mg^{2+}, its interaction with the functional group is much weaker than Co^{2+} with empty

d orbits, and hence the Mg^{2+} amount is controlled at low level. Afterwards, the carbonaceous frameworks are removed to obtain HP-DS (Mg, Co)$_3O_4$. Finally, self-polymerization of dopamine and subsequent cobalt-catalyzed graphitization in pyrolysis are conducted for the encapsulation of metal oxides within a uniform layer of NGC to attain targeted hybrid.[147] It is worth to mention that, based on the proposed *in-situ* coordinating mechanism, the morphology of spinel oxides can be rationally tuned by using metal salts with various anions. As an example, when metal acetates are adopted as raw materials with the same stoichiometric amount, quadruple-shelled hollow microspheres with limited porosity (LP-QS) are synthesized. The different acidity of anions is considered to be the main reason responsible for the morphology transformation.

Through the *in-situ* coordinating process, nanoparticle-aggregated microspheres with diameter of *ca.* 1.5 μm, uniform morphology and high purity are obtained (**Figure 3-2a**). The mesh-like interconnected porous shells of HP-DS (Mg, Co)$_3O_4$ are clearly revealed in **Figure 3-2b**. In the SEM image of a broken microsphere (**Figure 3-2c**), the hollow interior and the porous inner shell can be easily witnessed. Furthermore, the NGC coating appears to be uniform and well-defined in (Mg, Co)$_3O_4$@NGC, and the coating process did not alternate the original morphology (**Figure 3-2d, e, f**). The architecture visualization of HP-DS is enhanced by three-dimensional (3D) tomography in **Figure 3-2g**. The porous structures on both shells can be clearly observed at different rotational degrees and representative slices through the 3D volume of single microsphere at different depths.

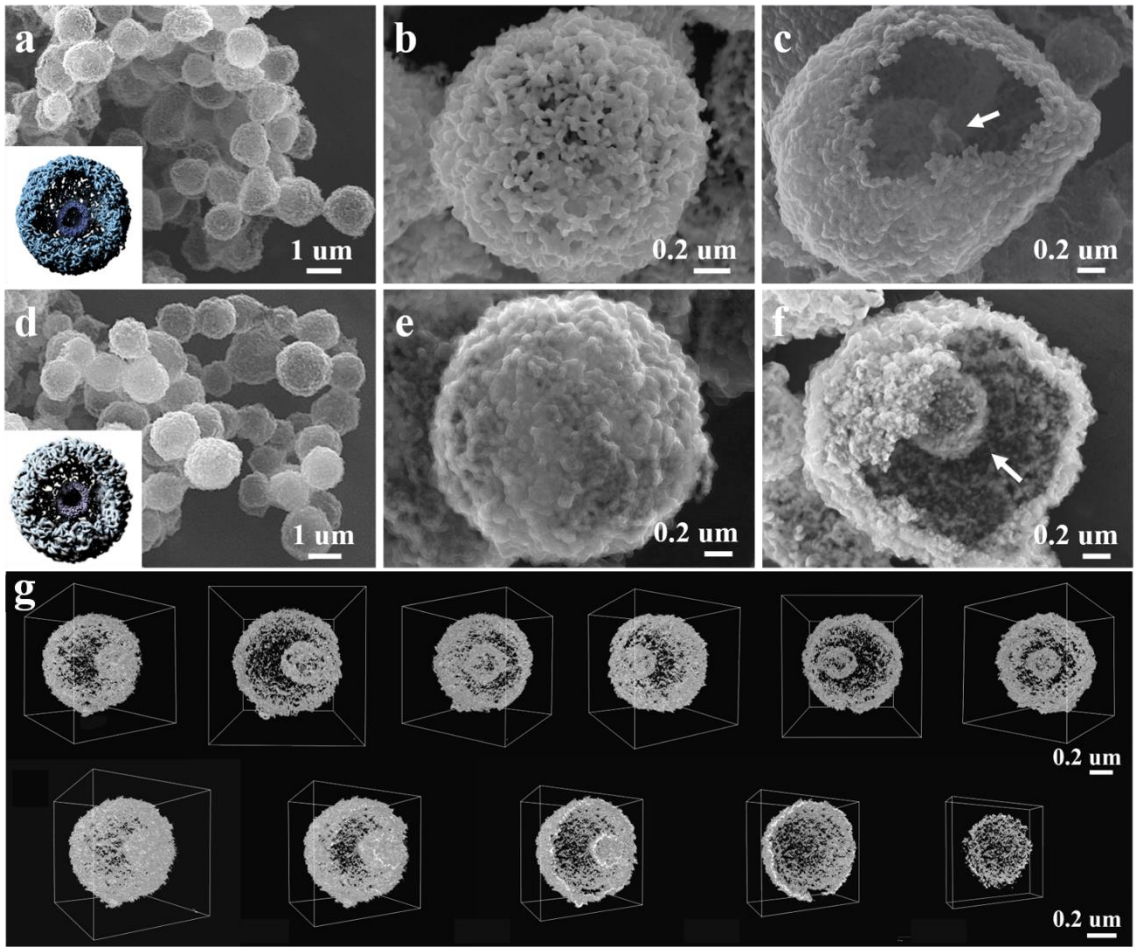

Figure 3-2 SEM images for (a-c) HP-DS (Mg, $Co)_3O_4$ and (d-f) (Mg, $Co)_3O_4$@NGC. The insets are the corresponding schematic images. (g) Perspective view of 3D morphology at various rotate angles and slices at different depths for HP−DS (Mg, $Co)_3O_4$.

TEM images and associated elemental mapping of HP-DS (Mg, $Co)_3O_4$ and (Mg, $Co)_3O_4$@NGC are provided in **Figure 3-3**. The primary particles of HP-DS (Mg, $Co)_3O_4$ are identified with average particle size of 20.1 nm. The energy-dispersive spectroscopy (EDS) results verify the uniform distribution of Co, Mg, and O. The HRTEM images in **Figures 3-3c, f** suggest high crystallinity of the primary particles for both (Mg, $Co)_3O_4$ and (Mg, $Co)_3O_4$@NGC, in which the typical cubic spinel patterns are defined by the lattice fringes and FFT. Also, the intimate contact between

$(Mg, Co)_3O_4$ particle and the graphitized carbon layer is revealed with characteristic *d*-spacings in **Figure 3-3f**. These results coincide with the polycrystalline selected area electron diffractions (SAED) patterns and Raman spectrum (**Figure 3-3g, h, i**). The highly graphitized degree of NGC is confirmed by the low intensity ratio of disorder (D) and graphic (G) peaks (I_D/I_G is 0.96) in Raman spectra.[121]

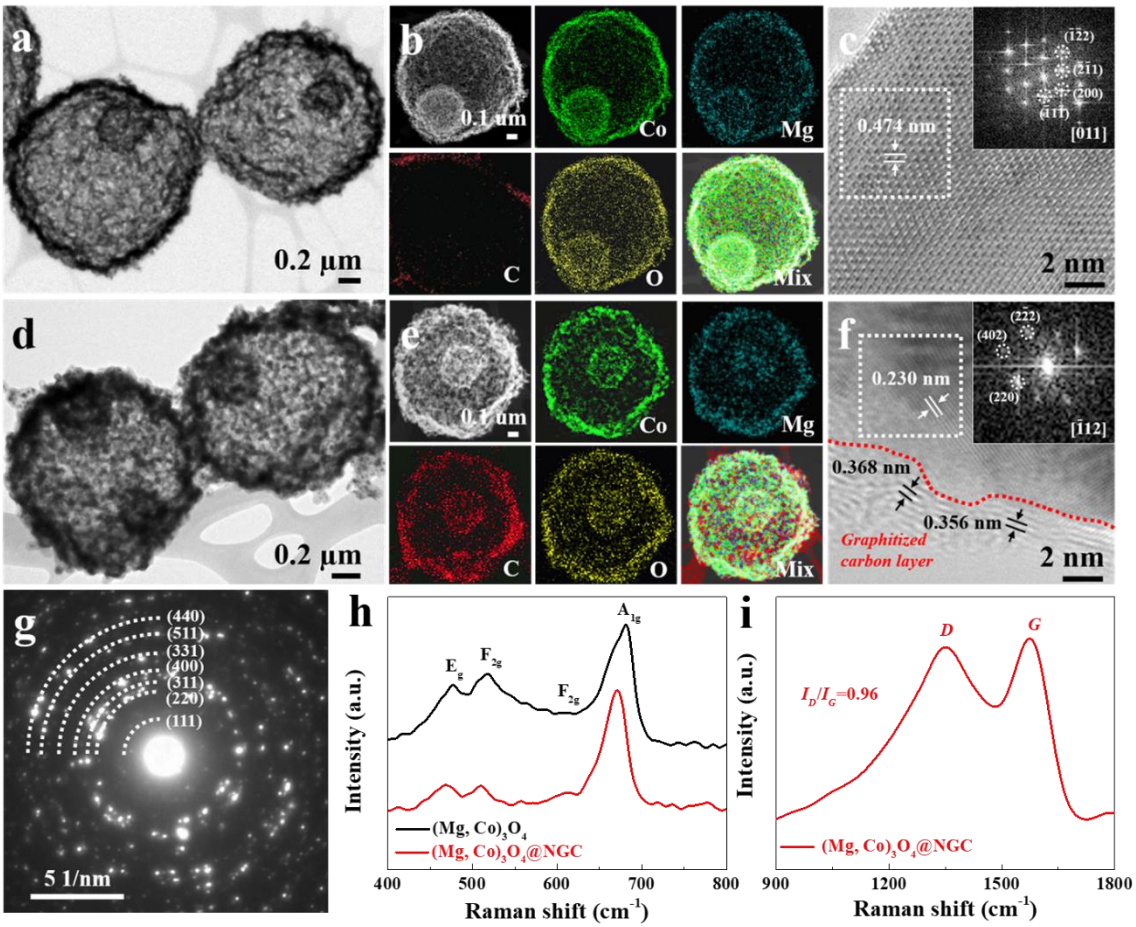

Figure 3-3 TEM images, HAADF-STEM images, corresponding EDS mappings and overlaid images of Co, Mg and C for (a, b) HP-DS $(Mg, Co)_3O_4$ and (d, e) $(Mg, Co)_3O_4$@NGC; (c, f) HRTEM images and inserted corresponding FFT patterns. (g) The SAED patterns of $(Mg, Co)_3O_4$@NGC, and (h, i) Raman spectra of $(Mg, Co)_3O_4$ and $(Mg, Co)_3O_4$@NGC.

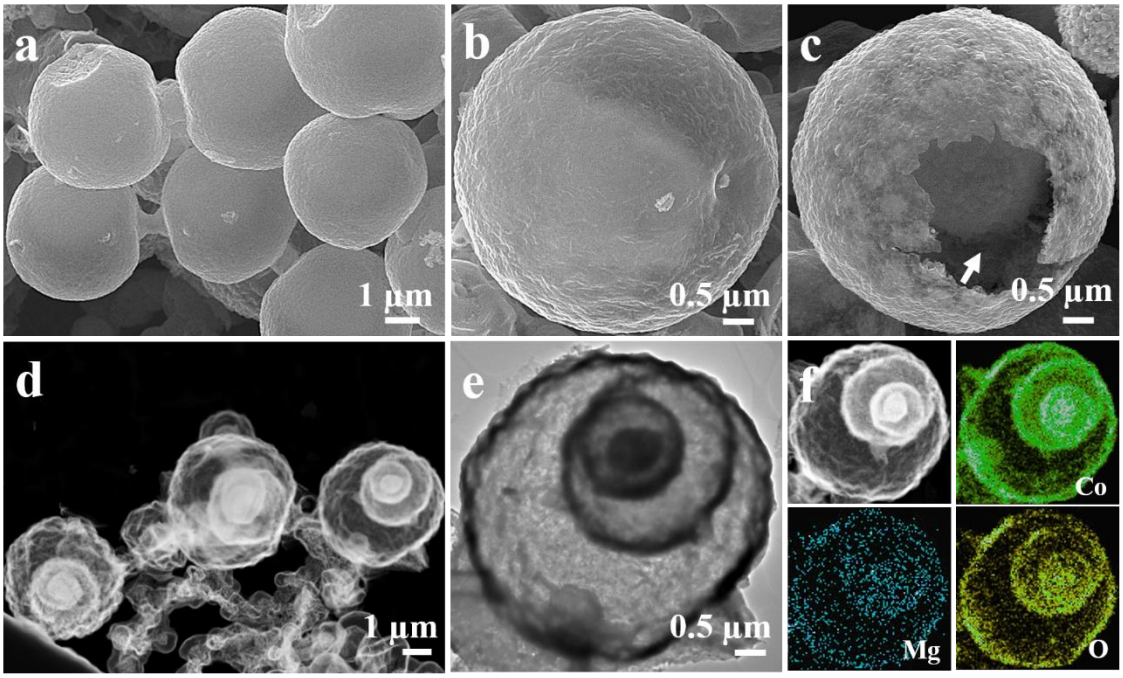

Figure 3-4 (a-c) SEM images, (d) STEM images, (e) TEM images and (f) corresponding EDS mapping of limited porous quadruple-shelled (LP-QS) hollow microspheres $(Mg, Co)_3O_4$.

As for LP-QS $(Mg, Co)_3O_4$ in **Figure 3-4**, its porosity on the shells is very limited. The main reason for the morphology difference between HP-DS and LP-QS is the higher pH of metal acetate solution in comparison to metal nitrates. The weak acidity of acetate solution causes the carbonaceous framework to have more negative charges on the surface, which then lead to higher cation absorption and bulk/surface concentration. When the carbonaceous frameworks are removed, the highly concentrated metal ion will form into multi-shelled metal oxide with larger sizes of microspheres and less porous shells. Furthermore, the acetate anions may react with glucose via the formation of ester bonds, which can also donate *p* electrons to the empty *d* orbits of transition metals and thus further increases the cation concentration within the frameworks.

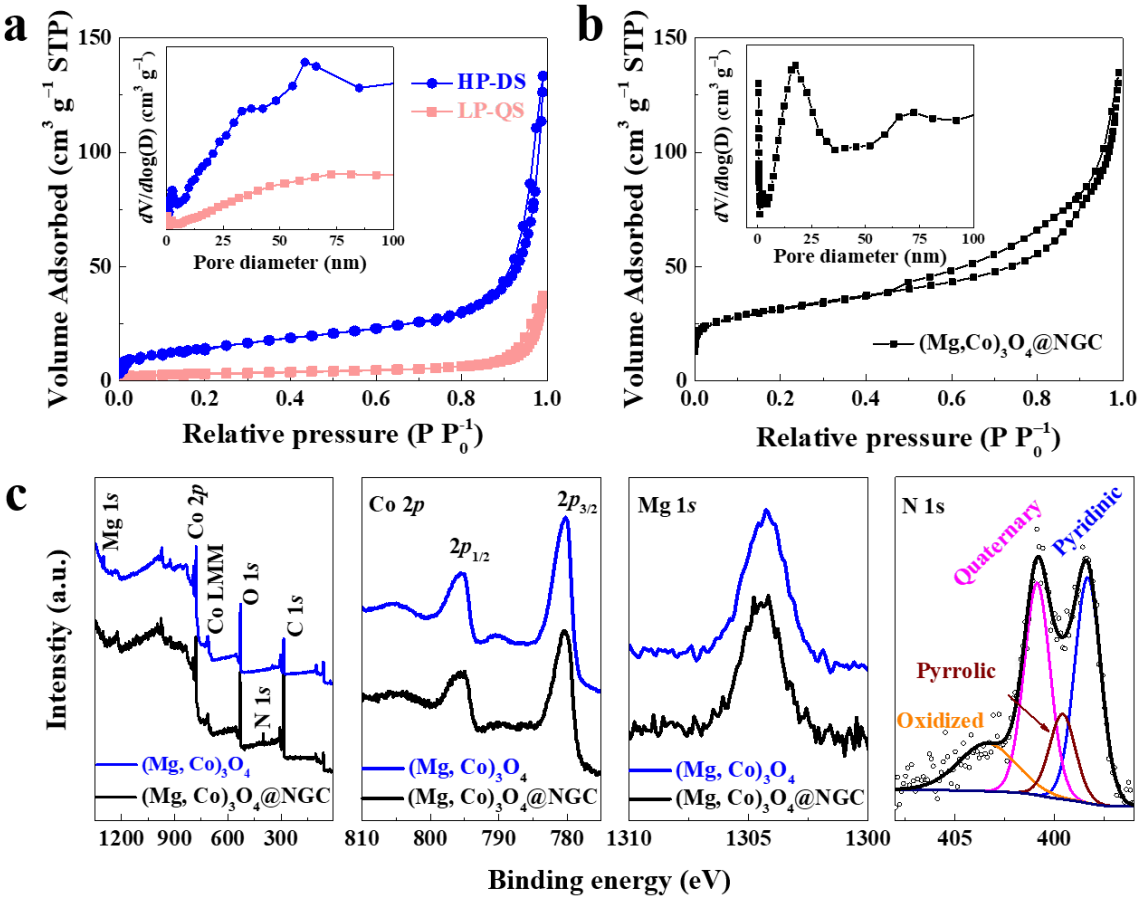

Figure 3-5 N_2 adsorption-desorption isotherms and pore size distributions for (a) HP-DS and LP-QS (Mg, Co)$_3$O$_4$, (b) (Mg, Co)$_3$O$_4$@NGC. (c) XPS survey spectra and Co 2*p*, Mg 1*s* and N *1s* high-resolution spectra for HP-DS (Mg, Co)$_3$O$_4$ and (Mg, Co)$_3$O$_4$@NGC.

The surface area and pore size distribution of the catalysts are examined by N_2 adsorption/desorption analysis. Although LP-QS consists of two additional inner shells, its estimated surface area of 32 m^2 g^{-1} is much lower than 84 m^2 g^{-1} of HP-DS that exhibits an obvious hierarchical pore distribution (**Figure 3-5a**). Additionally, the surface area and porosity are greatly increased by the NGC coating on (Mg, Co)$_3$O$_4$. A typical type-IV isotherm is observed for (Mg, Co)$_3$O$_4$@NGC with surface area as high as 194 m^2 g^{-1} (**Figure 3-5b)**, demonstrating its apparent hierarchical porosity.[102] The pore distribution indicates the well-defined coexistence of micropores with diameter

less than 2 nm, mesopores distributed around 16 nm, and macropores with average size of 75 nm.

XPS is performed to analyze the effects of polydopamine coating on $(Mg, Co)_3O_4$ (**Figure 3-5c**). The result signifies that the chemical valence of Co and Mg are maintained, and a newly observed peak attributed to N 1*s* is marked in $(Mg, Co)_3O_4$@NGC. The high-resolution N 1*s* spectrum demonstrates four types of N species at 398.3, 399.6, 400.9, and 403.4 eV, representing pyridinic, quaternary, pyrrolic, and oxidized N, respectively.[136] Among these species, the quaternary N is responsible for the ORR activity because it induces O_2 adsorption on the adjacent carbons; the OER activity is provided by the pyridinic N that expedite adsorption of the oxidation intermediates, such as OH^- and OOH^-.[91]

The XRD patterns in **Figure 3-6a** exhibit a typical $Fd\bar{3}m$ spinel structure for all the three samples. Additionally, a broad peak at about 25° attributed to (002) graphitic facet is observed in $(Mg, Co)_3O_4$@NGC.[148] When compared to XRD pattern of Co_3O_4 with the same morphology (**Figures 3-6b**), a significant negative shift of $(Mg, Co)_3O_4$ suggests a larger lattice volume that is beneficial for the transportation of oxygen species within lattice.[144, 149] Meanwhile, a sharp increase in electrical conductivity is also realized via Mg-substitution in $(Mg, Co)_3O_4$ (**Figure 3-6c, d**), which coincides with previous reports regarding Mg^{2+} doping.[146] Specifically, the electrical conductivity was calculated according to the equation: $\sigma = \rho^{-1} = \frac{l}{R \times A}$, in which σ is the electrical conductivity (S cm^{-1}), ρ is the electrical resistivity, l and A are respectively the length of 0.2 cm and the cross-sectional area of 0.018 cm^2 of densely packed materials. The electrical conductivity of HP-DS Co_3O_4 and HP-DS $(Mg, Co)_3O_4$ is calculated as 8.5×10^{-4} and 1.9×10^{-3} S cm^{-1}. As a result, an enhanced mass- and charge-transfer proficiency is expected. It is critical to confirm the amount of bivalent Mg^{2+}, since it is

inactive for oxygen electrocatalysis. According to ICP-AES result in **Table 3-1**, the atomic ratio of Co/Mg in $(Mg, Co)_3O_4$ is controlled as 18.2. Hence, the Mg^{2+} occupation in lattice is illustrated in **Figure 3-6e**. The low Mg substitution is attributed to the competition for free sites between Co^{2+} and Mg^{2+} during the *in-situ* coordination process. With such model, a Mg-assisted mechanism based on coordination chemistry is described here for ORR process. Specifically, as illustrated in **Figure 3-6f**, the ORR process at octahedral Co sites involves four-step proton/electron coupled mechanism, in which the steps 1 and 4 are the rate-limiting steps due to the instable $Co_{oct}–OO^{2-}$ bond (step 1) and the strong $Co_{oct}–O^{2-}$ bond (step 4).[76] An effective strategy to accelerate ORR kinetics is to expedite the removal of resultants (OH^-) from lattice. Since Mg^{2+} ions form far weaker coordination bonds with OH^- than Co^{2+} with empty *3d* orbits, they are expected to greatly lower the OH^- concentration in nearby space. This can create buffer zones that provide thermodynamically favorable environment for OH^-detachment, and thus accelerates these intermediate steps.

Table 3-1 The ICP-AES result of as-prepared HP-DS $(Mg, Co)_3O_4$.

	Co Weight%	Mg Weight%	Co/Mg Atomic ratio	Chemical formula
$(Mg, Co)_3O_4$	64.83	1.47	18.2	$Mg_{0.16}Co_{2.84}O_4$

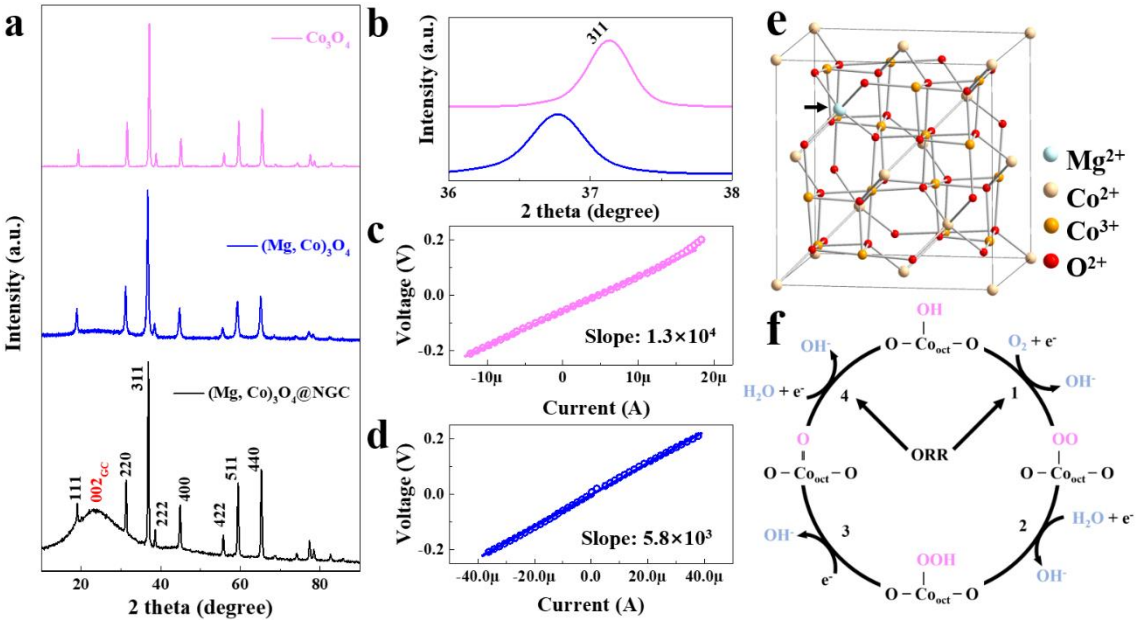

Figure 3-6 (a) XRD patterns of HP-DS Co_3O_4, HP-DS $(Mg, Co)_3O_4$ and $(Mg, Co)_3O_4$@NGC. (b) Local magnification of (311) peaks. Linear polarization resistance curves of (c) HP-DS Co_3O_4 and (d) HP-DS $(Mg, Co)_3O_4$. (e) Crystal lattice model for Mg-substituted $Fd\bar{3}m$ spinel $(Mg, Co)_3O_4$ and (f) the proposed four-electron ORR mechanism on octahedral Co sites of spinel oxides.

To validate the aforementioned positive influence of morphological and structural properties, bifunctional ORR and OER activities are measured by linear sweep voltammetry (LSV) within 0.1 M KOH electrolyte as shown in **Figure 3-7a, b**. The influence of hierarchical porosity on oxygen electrocatalysis is investigated. As shown, HP-DS $(Mg, Co)_3O_4$ exhibits superior performance, *i.e.* better bifunctional activity of 0.889 V (*vs*. RHE) defined on the gap (ΔE) between OER potential at 10 mA cm^{-2} ($E_{J\text{-}10}$) and ORR half-wave potential ($E_{half\text{-}wave}$), to LP-QS of 1.046 V. Its lower Tafel slopes than LP-QS also unveil its improved bifunctional electrocatalytic kinetics (**Figure 3-7c, d**). The high surface area, nanosized primary particles and hierarchical porosity of HP-DS are the decisive factors for its excellent bifunctional activities. The hierarchical porosity is of great significance as the micropores provide abundant

exposed active sites for oxygen electrocatalysis, while the meso/macropores encourage efficient transportation of oxygen species toward and away from electroactive sites.[118] Besides, the effects of Mg-modulation on intrinsic electrocatalytic activity of (Mg, $Co)_3O_4$ are also observed. HP-DS Co_3O_4 with the same morphology is tested to eliminate any geometric influences. In the ORR segment (**Figure 3-7a, b**), HP-DS Co_3O_4 offers a $E_{half\text{-}wave}$ of 0.713 V and j_l of 4.35 mA cm^{-2}, which are noticeably inferior to HP-DS (Mg, $Co)_3O_4$ with $E_{half\text{-}wave}$ of 0.747 V and j_l of 4.45 mA cm^{-2}. At this point, the Mg-assisted mechanism is evidenced. Meanwhile, enhanced OER kinetics is also achieved by (Mg, $Co)_3O_4$, including lower onset potential and overpotential of 0.406 V at 10 mA cm^{-2} in comparison to Co_3O_4 of 0.424 V. The optimized bifunctional electrocatalytic kinetics is contributed by the boosted mass- and electron-transfer properties through Mg-modulation, which is supported by the lower ORR/OER Tafel slopes of (Mg, $Co)_3O_4$ in comparison to Co_3O_4 (**Figure 3-7c, d**).

By further combining the merits of HP-DS (Mg, $Co)_3O_4$ and highly conductive NGC, (Mg, $Co)_3O_4$@NGC offers remarkable bifunctional performance. The start-of-the-art Pt/C and Ir/C are measured as ORR or OER benchmarks, respectively. In the ORR branch, (Mg, $Co)_3O_4$@NGC provides an onset potential (E_{onset}) of 0.925 V and a $E_{half\text{-}wave}$ of 0.842 V, which are superior to those of Pt/C (E_{onset} = 0.920 V, $E_{half\text{-}wave}$ = 0.830 V). A first-order four-electron transfer ORR pathway for (Mg, $Co)_3O_4$@NGC is identified by K-L equation based on ORR curves at various rotation rates (**Figure 3-7e, f**). As for the OER branch, despite a slightly higher onset potential, (Mg, $Co)_3O_4$@NGC affords a steeper polarization curve and reaches a current density of 10 mA cm^{-2} with lower overpotential of 0.346 V than Ir/C of 0.373 V. The excellent bifunctional catalytic kinetics of (Mg, $Co)_3O_4$@NGC are further confirmed by its low Tafel slopes (**Figure**

3-7c, d). The synergistic effects of the two components and structural superiorities are the keys for such promising bifunctional performance.

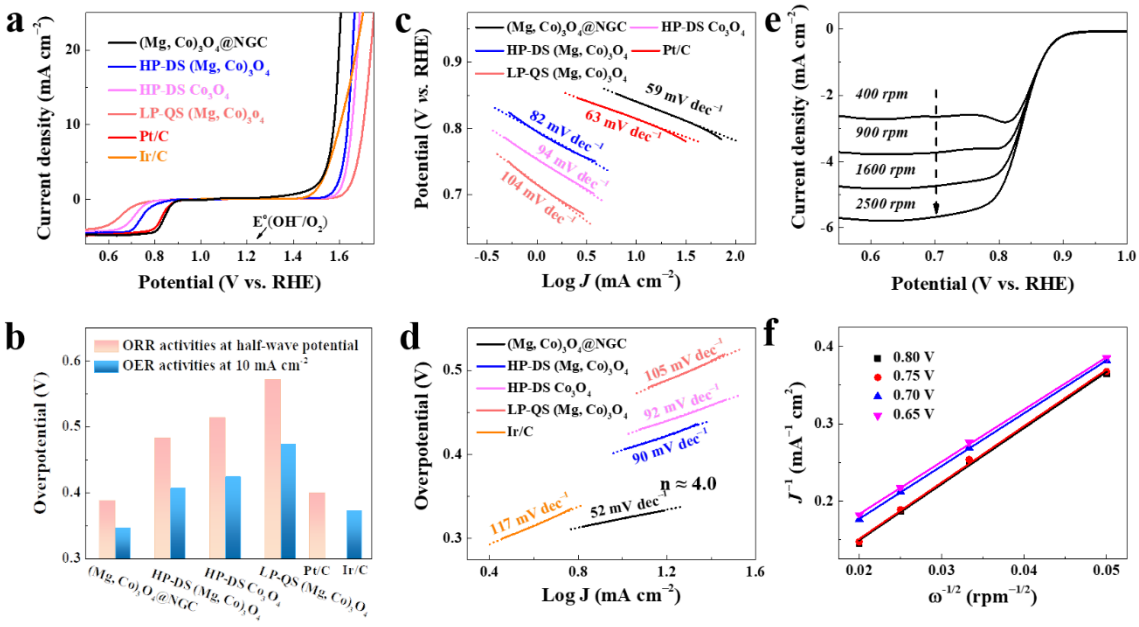

Figure 3-7 (a) Bifunctional oxygen electrocatalytic activities and (b) the specific overpotential of various electrocatalysts at RDE (1600 r.p.m) in 0.1 M KOH electrolyte. (c) ORR polarization curves at different rotating speeds and corresponding (d) K-L plots for (Mg, Co)$_3$O$_4$@NGC. (e) ORR and (f) OER Tafel plots of different electrocatalysts.

Rechargeable Zn-air batteries are fabricated using (Mg, Co)$_3$O$_4$@NGC on carbon paper as air electrode to explore its potential for practical application in ambient air. A mixture of Pt/C and Ir/C (1:1 weight ratio) with the same mass loading on carbon paper is also fabricated as the reference Zn-air batteries. The galvanodynamic charge and discharge curves are presented in **Figure 3-8a**. Both Zn-air batteries deliver a similar open circuit voltage at *ca.* 1.45 V and comparable charge performance. However, the Zn-air battery using (Mg, Co)$_3$O$_4$@NGC as air electrode outperforms the reference in the discharge segment, especially at relatively high current density. Its power density

of 125 mW cm^{-2} is much higher than the noble-metal reference of 90 mW cm^{-2} as indicated in **Figure 3-8b**. Notably, excellent durability is achieved by (Mg, Co)$_3$O$_4$@NGC as indicated in **Figure 3-8c**. When cycling at a constant current density of 10 mA cm^{-2} with a charge-discharge period of 2 hours, (Mg, Co)$_3$O$_4$@NGC assembled Zn-air battery demonstrates a charge-discharge voltage gap as low as 0.80 V and long-term cycling stability without discernible voltage degradation for over 200 hours, surpassing significantly noble-metal cathode. Even at a high current density of 20 mA cm^{-2} (**Figure 3-8d**), a narrow charge-discharge voltage gap of 0.90 V and durable cyclability over 100 hours are also delivered by (Mg, Co)$_3$O$_4$@NGC, while the noble-metal catalyst offers very limited durability less than 40 hours.

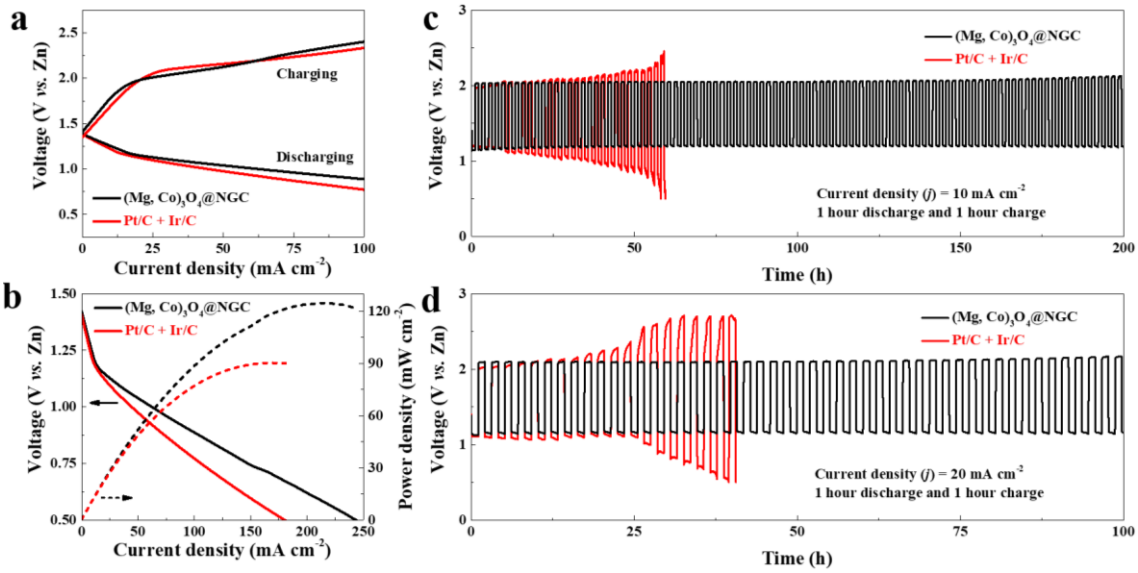

Figure 3-8 (a) Polarization curves, (b) the corresponding power density plots and their cycling performance at (c) 10 mA cm^{-2} and (d) 20 mA cm^{-2} of Zn-air batteries using (Mg, Co)$_3$O$_4$@NGC or Pt/C + Ir/C as air electrode.

3.4 Summary

Benefiting from the proposed *in-situ* coordinating strategy, double-shelled (Mg, Co)$_3$O$_4$@NGC microspheres with hierarchical porosity are designed as promising

bifunctional oxygen electrocatalysts with the following merits. First, the double-shelled architecture with hierarchical porosity greatly enhances ORR/OER kinetics. Second, the Mg modulation positively influences electrocatalytic activity by facilitating reactant transportation and improving electrical conductivity. Finally, a novel Mg-assisted mechanism based on coordination chemistry for tailoring lattice alkalinity is proposed to modify oxygen electrocatalysis. It is believed that tailoring of lattice alkalinity via controllable occupation of specific metal ions is a feasible and general strategy to alter oxygen electrocatalysis. These results open inspiring insight into rational design of efficient oxygen electrocatalysts for practical energy conversion systems.

4 Dynamic Electrocatalyst with Current-Driven Oxyhydroxide Shell for Rechargeable Zn-air Battery

4.1 Introduction

Previously, limitations in availability and rechargeability of oxygen electrocatalysts have hindered the popularization of Zn-air battery, but blooming efforts on exploring suitable and durable candidates to catalyze cathode reactions have led to the recent rejuvenation of this century-old technology.[50, 51, 79] As such, huge families of materials have been investigated, including metals, alloys, oxides, sulfides, nitrides, phosphides and their derived composites with carbon.[47, 102, 105, 106, 117, 123, 150-156] To this day, exploration for ideal bifunctional electrocatalysts remains to be the research mainstream, but attentions are shifting toward understanding the relationship between battery performance and physiochemical properties of electrocatalysts for performance breakthrough. Particularly, a debate over the actual active phases during cycling of these electrocatalysts is raised recently and conflicting results have perplexed the research community.[152, 157, 158] Increasing reports on spectroelectrochemistry towards the half reactions, *i.e.* ORR or OER, in three-electrode systems suggest that an unexplored chasm is at work. For instance, Hu *et al*. reported both nickel iron diselenide and nickel phosphide as efficient and long-lasting OER electrocatalysts, but neither is static stereotype under oxidation voltage in alkaline electrolyte.[159, 160] This contradiction was resolved with observations of surficial phase transformation from these compounds to their derived oxides or oxyhydroxides, which also aligns with results on metal oxides, sulfides and nitrides.[157, 161-163] Furthermore, the latest attention has been drawn toward ORR electrocatalysts, in which an alteration was also demonstrated.[164]

These studies expose an often-overlooked fact that directly assuming native state of metal-based electrocatalyst as the active representation in Zn-air battery operation may lead to false correlation between material characteristics and performance, albeit the undeniable role of their native properties. In particular, the electrocatalyst evolution during cycling is often ignored, and limited efforts have been placed to identify the actual configuration of electrocatalyst in the mid-way or post-cycling status. Therefore, a systematic study is in high demand to pry into this "black box" and reveal the underlying mechanism governing the current-driven transformation of electrocatalyst. Two key factors are worth pointing out, one is that the potentiodynamic driven methodology applied in ORR or OER measurements is different from the continuous galvanostatic technique for battery operation, and the other is that alkaline electrolyte used in Zn-air batteries is far more concentrated, so that a lower electrochemical barrier is required for valence variation of the principle elements. The different environment may cause variances in electrochemical behaviors in comparison to the standard three-electrode system. To be specific, it is predicted in advance that a current-driven oxyhydroxide derived from the native materials will be generated and combined with its electrochemically unavailable bulk as a "shell-bulk" configuration; the performance-dominant elements within the shell will experience periodic swing in their chemical states during cycling.

In this chapter, for vivid description of the evolution, a concept of dynamic electrocatalyst is proposed for rechargeable Zn-air battery. A time coordinate is added as the fourth axis onto the basis of conventional three-dimensional spatial space, and hence a dynamic picture is established following battery operation. As proof of this concept, a bimetal nitride, $(Co,Fe)_3N$, is selected as typical representation for metal-based materials with two major considerations. Firstly, based on both experimental and

theoretical evidences, metal nitride intrinsically exhibits metallic nature with high electrical conductivity.[113, 155, 157, 165] A thin nitrogen-doped carbon coating, dual-metal and morphological benefits are also incorporated as the promoter effects. More importantly, its oxygen-free bulk can furnish an ideal arena to record the interfacial formation of the predicted oxygen-containing shell during cycling. By collecting the time-varying information at both macro and micro scales, the detail structural evolution and actual configuration upon Zn-air battery cycling can be unveiled.

4.2 Experiment procedures

4.2.1 Material synthesis

The preparation of bimetal nitride adopted herein is a modified method based on literature.[166] It includes three major steps for an entire procedure. The first step is to synthesize the solid nanocuboid precursor. Typically, 3 g of polyvinylpyrrolidone (K30) with an average molecular weight of 40,000 was fully dissolved in 15 mL anhydrous ethanol to form a colorless and viscous solution. In a separate container, 1.4 g cobalt acetate tetrahydrate was dissolved in 85 mL anhydrous ethanol. These two solutions were mixed within a 250 mL round-bottom flask and refluxed for 12 hours at 90 °C under magnetic stirring of 1200 rpm. After centrifugation using ethanol at 7000 rpm for 3 times and sequent drying in air, the pink Co-containing precursors were obtained. Then, for the cation-carving process, 0.2 g of fresh Co-containing precursors were even dispersed in 20 mL anhydrous ethanol under ultrasonication. Another clear solution is formed by dissolving 0.16 g iron sulfate heptahydrate into 200 mL 1:1 ethanol-water solution under nitrogen gas protection. The above two solutions were mixed and allowed to react under stirring at 500 rpm for 15 minutes. Nitrogen gas was continuous bubbling during this process. The yellow powders, *i.e.* the bimetal layered double

hydroxide (LDH), were collected through centrifugation at 7000 rpm and washed with ethanol. Lastly, the ammonization process was conducted at high temperature calcination. Prior to that, the bimetal layered double hydroxide was pretreated with dopamine hydrochloride polymerization within 0.01 M tris(hydroxymethyl)aminomethane buffer aqueous solution. The ratio between the bimetal layered double hydroxide and dopamine hydrochloride was fixed to be 2, and the mixed solution was stirred at 500 rpm for 5 hours. Afterwards, the dried black precipitate was collected by centrifugation at 9000 rpm and washed with deionized water and ethanol. The precipitate was heat treated at 500 °C under ammonia gas for 1 hour, with a ramp rate of 2 °C per minute. Argon gas was used to protect the sample during the ramping period, and the tube furnace was purged by ammonia gas only after the temperature has stabilized at 500 °C. After cooling down to room temperature, the targeted bimetal nitride of $(Co,Fe)_3N$_R were obtained. The CoOOH reference were prepared following procedure in previous report.[167]

4.2.2 Materials characterizations

The morphology and energy-dispersive spectra were collected using field emission scanning electron microscope (UltraPlus FESEMs, 20 kV) and transmission electron microscope (TEM, FEI Titan 80-300 LB, 300 kV) equipped with an X-ray spectrometer detector. The electron energy loss spectroscopy (EELS) was acquired by a double aberration-corrected TEM (FEI Titan 80-300 HB, 200 kV). The surface area and porous structure were calculated based on N_2 isotherm obtained on a Brunauer–Emmett–Teller (BET) analyzer (Quantachrome Instruments QuadraSorb SI4), and the pore size distribution was calculated based on the density functional theory (DFT) model. The structural information was obtained by X-ray diffraction (Rigaku Ultima

IV with Cu Kα as the radiation source) and Raman spectroscopy (WiTEC alpha300R Raman microscope at an excitation line of 532 nm). The wide-angle X-ray scattering (WAXS) images were acquired in transmission mode at Brockhouse X-ray Diffraction and Scattering Beamlines (High Energy Wiggler, BXDS-WHE) of Canadian light source. The energy was set at 35 keV with a wavelength of 0.359106 Å. The two-dimensional images were calibrated by a LaB_6 standard sample. The General Structure Analysis System II (GSAS-II) software was employed to average and integrate the synchrotron X-ray diffraction patterns.[168] The X-ray photoelectron spectroscopy was carried out using PHI 5000 VB III, and argon ion bombardment was used to remove the samples surface so that their bulk chemical information can be collected. The result was calibrated with a reference C *1s* peak set to 284.84 eV. The electron paramagnetic response (EPR) was acquired at 77 K by a Bruker EMX-10/12 spectrometer (2 mW microwave power, 9.4 GHz microwave frequency, 100 kHz modulation frequency and 0.2 mT modulation width). *Operando* X-ray absorption spectroscopy were performed at Soft X-ray Microcharacterization Beamline (SXRMB, 06B1-1) of Canadian Light Source and a homemade Zn-air battery prototype was directly adopted as the *operando* setup. The back side of carbon paper without electrocatalyst was placed to face the incident photon and the Bruker detector. Both of Co (7709 eV) and Fe K-edge (7112 eV) spectra were recorded on fluorescence yield mode. Standard metal foils and metal oxides purchased from Sigma-Aldrich were used as reference.

4.2.3 Electrochemical measurement.

Prior to battery fabrication, the electrocatalyst ink was prepared by dispersing the electrocatalysts in 0.2 wt.% Nafion solution and then sprayed onto a carbon paper (SGL Carbon; Ion Power Inc.) with a loading of 1 mg cm^{-2} to form the gas diffusion

layer (GDL). This exact process was also used to prepare the performance benchmark with equal amount of 20 wt% Pt/C and RuO_2. Then, polished zinc plate, separator, GDL were assembled layer-by-layer to form Zn-air battery, which was filled with 6 M potassium hydroxide and 0.2 M zinc acetate aqueous solution as electrolyte. The cycling tests were carried out using galvanostatic method on a Land battery tester (LAND-CT2001A, Land Electronic Co., Ltd., Wuhan). The GDLs were treated to the predetermined electrochemical states, and then taken out immediately for these *ex-situ* characterizations. Their polarization curves were measured on a Gamry 5000E workstation. The bifunctional electrocatalytic measurements were performed on a Biologic VSP 300 workstation using a three-electrode system, in which GDLs were used directly as the working electrode, while a saturated calomel electrode and a graphitic rod served as the reference and counter electrode. Oxygen saturated 0.1 M potassium hydroxide aqueous solution was the electrolyte. The obtained data were calibrated to the reversible hydrogen electrode with the Nernst equation and further converted to the overpotential representing the difference against $E°(O_2/H_2O)$ at 1.23 V. The Tafel slopes were calculated according to the Tafel equation.

4.3 Results and discussions

Native Properties. A bimetal LDH was first obtained *via* a cation-carving method using Fe^{II} as a graving agent to attack Co-based nanocuboid precursor (**Figure 4-1a**). This method allows a series of ligand-release and re-coordination processes to obtain a secondary hollow structure with tunable Co/Fe ratio controlled by stoichiometric factor of Fe^{II} source. After dopamine polarization and subsequent ammonolysis, the target bimetal nitride is obtained with an elemental Co/Fe ratio of 5 : 4 according to the EDS result (**Figure 4-1h**). The product takes on a nanoplate-

aggregated hollow nanocuboid morphology with uniform elemental distribution (**Figure 4-1b-d** and **g**). Its N_2 adsorption/desorption isotherms in **Figure 4-1i** reveal a typical type-IV curve with a surface area of 251 m^2 g^{-1} and hierarchical porosity that includes micro-, meso- and macropores as indicated in the inset of **Figure 4-1i.** Specifically, the micro- and mesopores originate from holes on primary nanosheets and gaps in between (inset of **Figure 4-1c**), while the macropores are mainly attributed to the void cavity of the secondary nanocuboids.

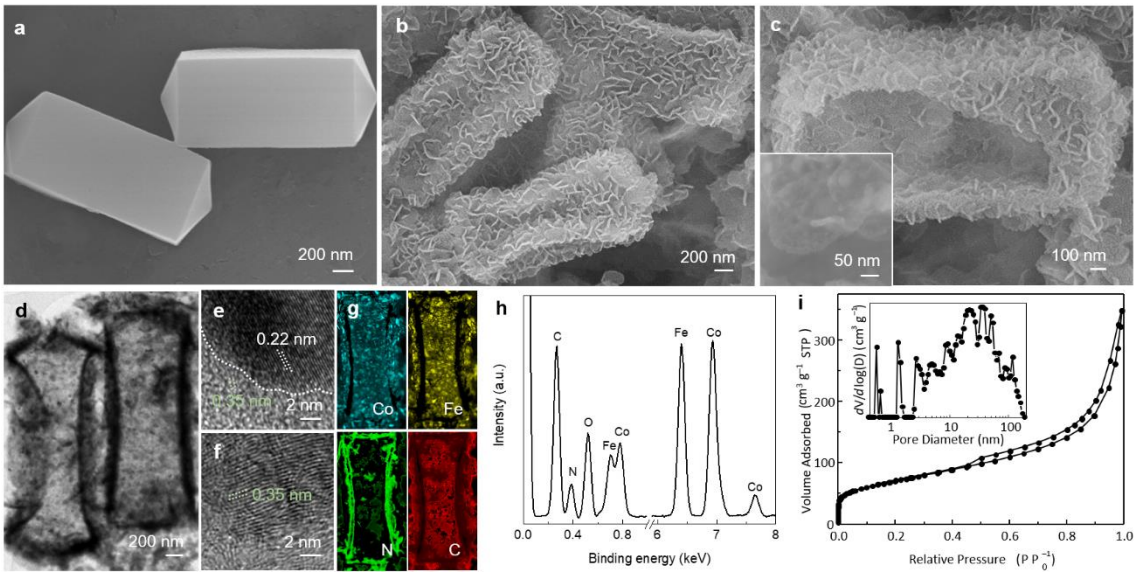

Figure 4-1 SEM images of (a) Co-containing precursor and (b, c) secondary nanocuboids at different magnification, inset of (c) shows the enlarged image of a primary nanosheet. (d) TEM images of secondary nanocuboids, (c, d) HRTEM images at different regions, (e) the corresponding elemental mappings and (h) EDS curve of $(Co,Fe)_3N$_R. (i) N_2 adsorption-desorption isotherms and the pore size distribution.

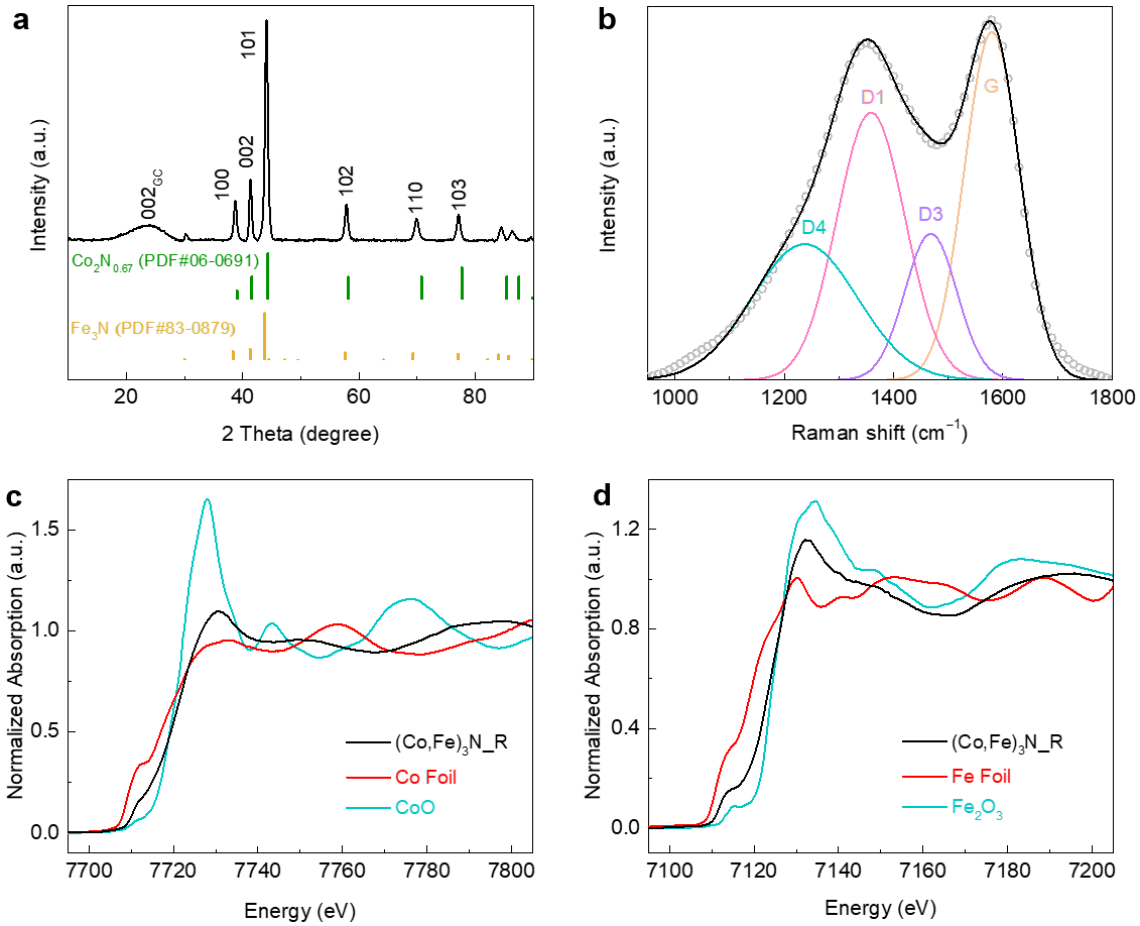

Figure 4-2 (a) XRD pattern of $(Co,Fe)_3N\_R$ with the $Co_2N_{0.67}$ (PDF#06-0691) and Fe_3N (PDF#83-0879) as the reference patterns. (b) Raman spectra of $(Co,Fe)_3N\_R$. (c) Co and (d) Fe K-edge XANES spectra with respective metal foils and oxides as the reference spectra.

XRD pattern in **Figure 4-2a** of product suggests a typical hexagonal crystal structure indexed well to the reference patterns of $Co_2N_{0.67}$ (PDF#06-0691) and Fe_3N (PDF#83-0879). Combining with EDS result, chemical formula of the bimetal nitride is confirmed to be $(Co_{0.56}Fe_{0.44})_3N$ and marked as $(Co,Fe)_3N\_R$. HRTEM image in **Figure 4-1e** demonstrates that the particle possesses a uniform crystal phase with lattice spacing of 0.22 nm belonging to the (0002) facet. A carbon outer layer on particle is also identified with a spacing of 0.35 nm and inconsistent N dopants (**Figure 4-1f**). The clear boundary in between verifies the critical role of thin carbon layer in improving

the air stability of nitride and protecting it from gradual oxidation in air.[169, 170] Raman spectroscopy analysis of the sample confirms both graphitic and defective carbon characteristics.[84, 90] As shown in **Figure 4-2b**, it is deconvoluted into four major peaks, including G band reflecting defect-free sp^2 carbon with E_{2g} symmetry, D1 band representing disorder A_{1g} symmetry of graphite, D3 band attributed to sp^3 amorphous carbon and the D4 band of polyene-like structure. As the basis for defect degree of carbon networks, I_{D1}/I_G is calculated to be 0.95 for $(Co,Fe)_3N$_R.[84] The thin carbon coating is not only beneficial for electrical conductivity and electrochemical performance, but also aids in maintaining the structural stability.

The electronic structure of $(Co,Fe)_3N$_R is unveiled by Co and Fe K-edge X-ray adsorption near-edge structure (XANES) spectra. As demonstrated in **Figure 4-2c**, Co K-edge curves of Co foil and $(Co,Fe)_3N$_R both present a pre-edge hump at 7712 eV attributed to electron transitions from 1*s* to 3*d* as their metallic feature, which is almost absent in CoO because of the dipole-forbidden transition of octahedral Co.[171] In comparison to Co foil, $(Co,Fe)_3N$_R presents a slightly weakened pre-edge hump as the nitride feature and an enlarged white-line crest, suggesting higher electron occupancies at the Co *3d* orbits and lower electrons allocation at the *4p* orbits. This observation should be ascribed to its weaker 4*p*-3*d* hybridization at Co sites and the altered net charge distribution.[172] Similar conclusions can be made with the Fe K-edge spectrum with similar pre-edge characters (**Figure 4-2d**).[173] Additionally, the inflection points of Co and Fe K-edges of $(Co,Fe)_3N$_R are both located close to their respective oxide references, suggesting similar electron offset towards N.[126]

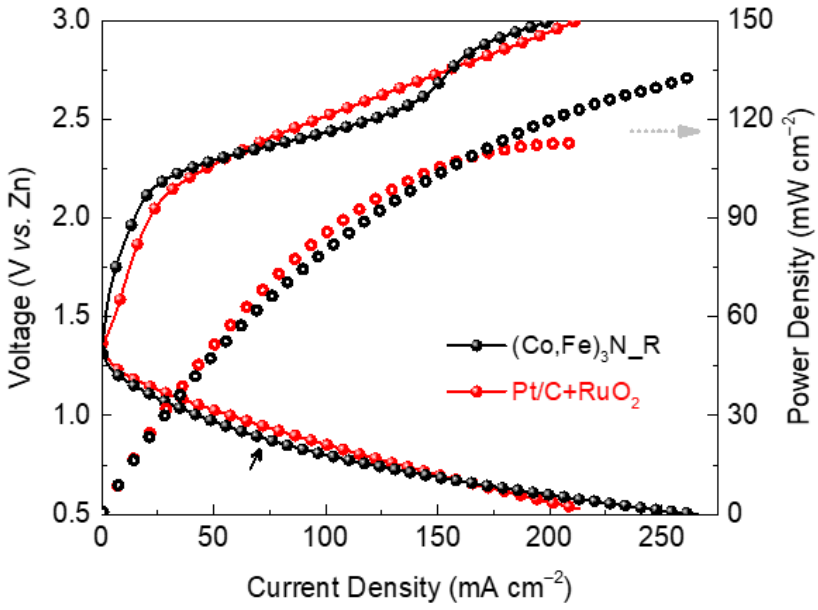

Figure 4-3 Polarization curves and power density plots of Zn-air batteries using $(Co,Fe)_3N$_R and commercial Pt/C + RuO_2.

Electrochemical behaviors. Viability in battery application of metal nitride was evaluated through a layer-by-layer Zn-air battery prototype using GDL sprayed with electrocatalyst as air electrode.[120] A performance reference with equal loading of commercial Pt/C and RuO_2 on GDL was also prepared and tested in the same manner. Their polarization plots are shown in **Figure 4-3**. With a comparable open circle voltage, $(Co,Fe)_3N$_R first performs feebly at low current discharge. However, after a short period of expansion, its performance gap against the noble-metal reference begins to narrow at around 75 mA cm^{-2}; its power density eventually peaks at 133 mW cm^{-2}, which is superior to 113 mW cm^{-2} achieved by Pt/C+RuO_2. As for the initial charging process of $(Co,Fe)_3N$_R, it can be divided into two successive regions containing two intersection sites with Pt/C+RuO_2 at 60 and 155 mA cm^{-2}. Its initial rapid voltage rise suggests the inferior intrinsic activity, but it also demonstrates much flatter slope comparing to Pt/C+RuO_2 after the initial surge. A step offset then occurs between the second intersection and the last period, and thereafter its uptrend is slightly accelerated

to a comparable level to Pt/C+RuO_2. All of the above phenomena reflected by polarization analysis point toward the electrochemical instability of the $(Co,Fe)_3N$_R and its possible transformation with accumulated influence of galvanodynamic scans.

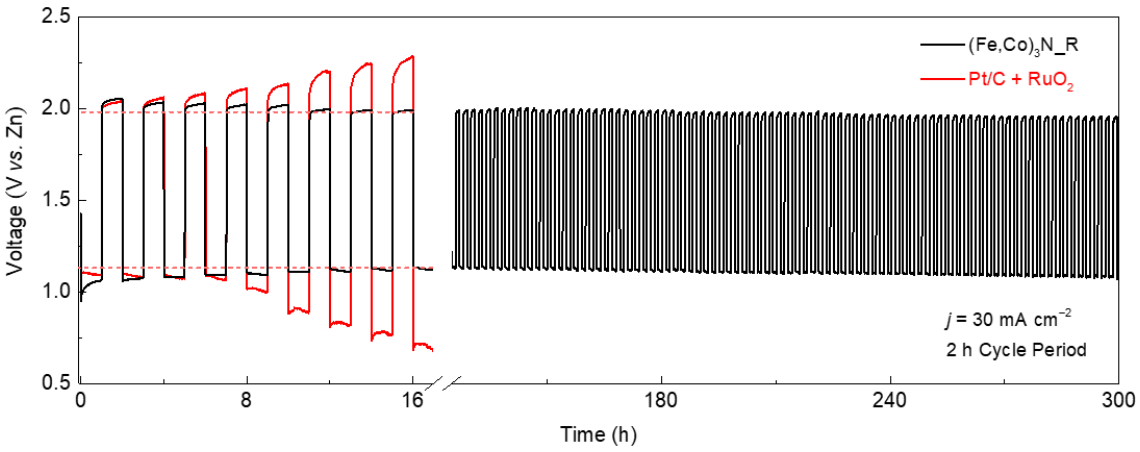

Figure 4-4 Cyclic performance of Zn-air batteries with respective $(Co,Fe)_3N$_R or equal weight ratio mixture of 20% Pt/C and RuO_2 in air cathode. Each cycle contains 1 hour discharging and 1-hour charging at a current density of 30 mA cm^{-2}.

The galvanostatic discharge-charge profile of Zn-air battery using $(Co,Fe)_3N$_R on GDL as air electrode is obtained under a current density of 30 mA cm^{-2} and 2 hours cycling period (**Figure 4-4**). In comparison to the regular recession of Pt/C+RuO_2, a slow activation process is observed for $(Co,Fe)_3N$_R in the first several hours. In detail, during the initial discharge, $(Co,Fe)_3N$_R shows a low start at 0.95 V (*vs.* Zn) against 1.10 V of Pt/C+RuO_2, but it soon elevates with reducing their discrepancy to 0.03 V by the end. When turning to the initial charge, a smooth diminishment of 0.02 V is also observed in their voltage discrepancy. In the following cycles, the discharge-charge voltage gap of $(Co,Fe)_3N$_R further narrows and eventually reaches a steady state of 0.85 V by the 8^{th} cycle (16 hours), while the gap expands rapidly to over 1.5 V for Pt/C+RuO_2. This observation should be interpreted as an evolution of the $(Co,Fe)_3N$_R that initiates at the first discharge, followed by a stepwise maturation in several hours.

Afterwards, the $(Co,Fe)_3N$_R battery maintains a life cycle for over 300 hours with a neglectable decay in discharge-charge voltage gap.

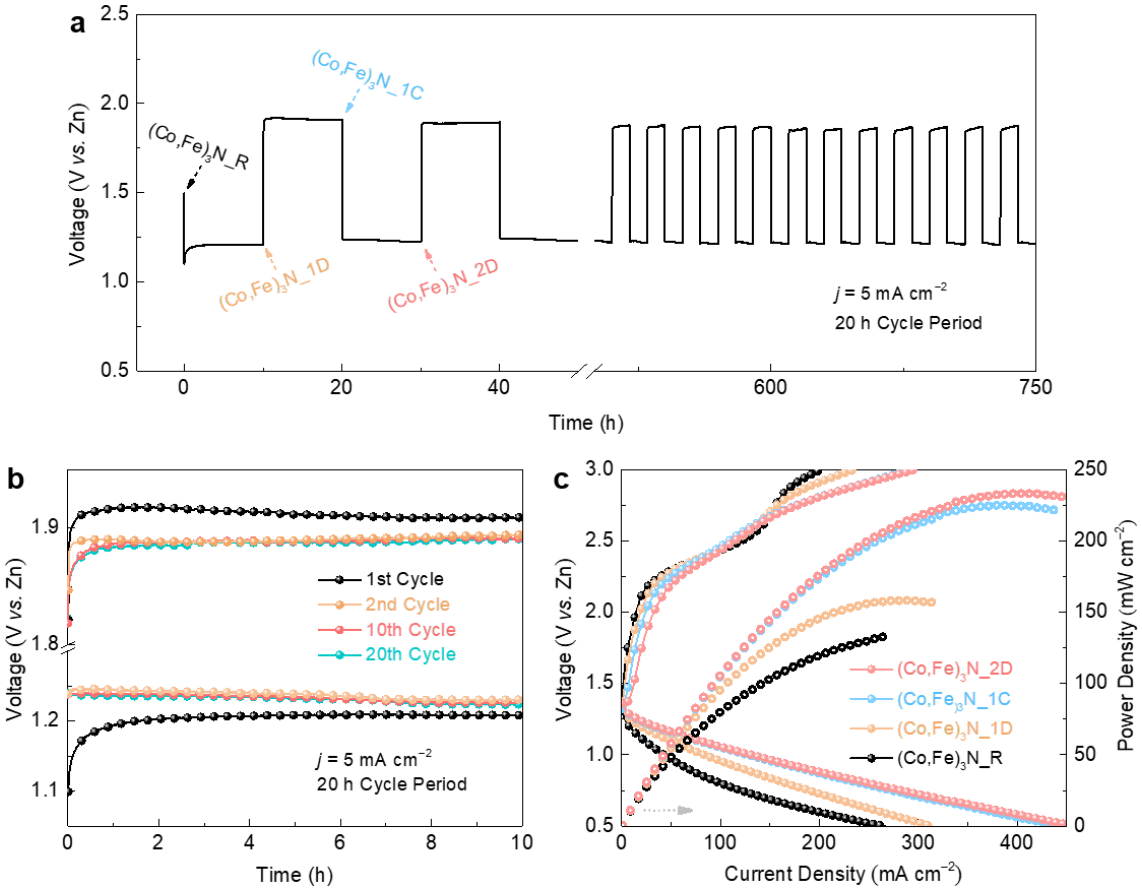

Figure 4-5 (a) 20 hours cycling profile under a current density of 5 mA cm^{-2} and (b) the corresponding comparison at different cycles. (c) The polarization curves and power density plots of Zn-air batteries processed to different electrochemical stages.

To magnify the maturation process of $(Co,Fe)_3N$_R, another cycling experiment with a discharge/charge period of 20 hours is conducted at 5 mA cm^{-2} (**Figure 4-5a, b**). Similar phenomena are observed with battery experiencing an iconic leap in its discharge plateau from 1.10 V to 1.21 V after about 2 hours, whereas its initial charge platform endures a smooth optimization from 1.92 to 1.91 V. In the subsequent cycle, a 0.04 V gain is observed to raise the discharge voltage to 1.25 V and a stable charge voltage of 1.89 V is achieved. Then, these battery parameters remain relatively constant

for the following 700 hours. Taking a panoramic view on the cycling behaviors, the maturation pathway of $(Co,Fe)_3N$_R during battery operation can be divided into four clear stages along the time coordinate as indicated in **Figure 4-5a**. They include the raw $(Co,Fe)_3N$_R, the first discharged $(Co,Fe)_3N$_1D, the first charged $(Co,Fe)_3N$_1C, and the second discharged $(Co,Fe)_3N$_2D. Besides the native properties of $(Co,Fe)_3N$_R, $(Co,Fe)_3N$_1D reflects latent generation of some new species, $(Co,Fe)_3N$_1C enables the consolidation of the active phases, and finally $(Co,Fe)_3N$_2D represents the matured configuration that realizes long-term cycling. Hereafter, their differences and influences on battery performance will be discussed in detail.

Maturation Pathway. The polarization curves of electrocatalysts processed to different electrochemical states are displayed in **Figure 4-5c**. As shown, when comparing to the raw state, a higher power density of 158 mW cm^{-2} is delivered by $(Co,Fe)_3N$_1D, then it is further raised to 225 mW cm^{-2} for $(Co,Fe)_3N$_1C and finally reaches 234 mW cm^{-2} by $(Co,Fe)_3N$_2D. Moreover, the originally arched discharge polarization curve is gradually straightened and becomes almost linear by the end of the second discharge. As for the charging curves, a positive influence is also observed in the current density ceiling and a similar straightening trend is found. The step offset at 155 mA cm^{-2} observed in $(Co,Fe)_3N$_R is visibly weakened for $(Co,Fe)_3N$_1D and further reduces for both $(Co,Fe)_3N$_1C and $(Co,Fe)_3N$_2D. Despite of the elevations, the matured catalyst demonstrates increased slopes in both of its charge and discharge polarization curves, which may be triggered by the negative kinetic influence of maturation. To validate the observations, air electrodes at selected states were transferred and examined freshly in a three-electrode system.

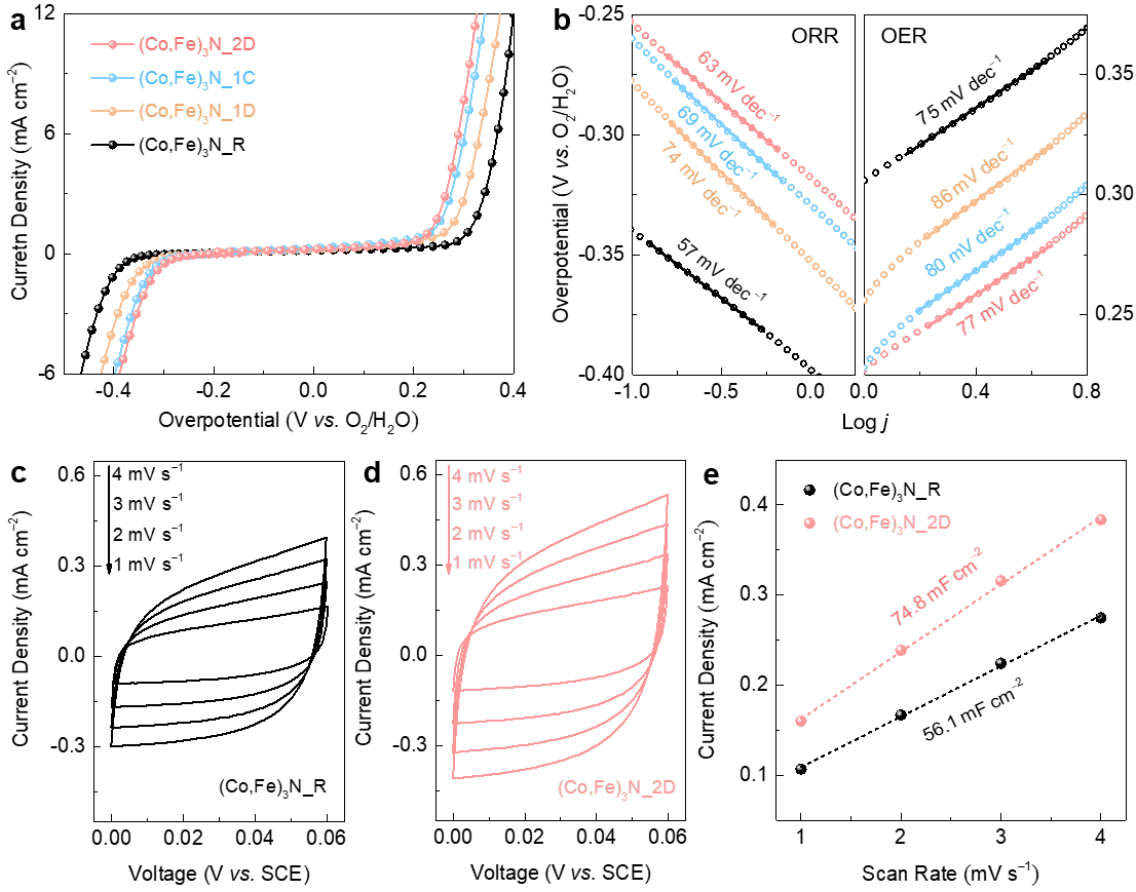

Figure 4-6 (a) Bifunctional oxygen electrocatalytic activities of those air electrodes according to three-electrode system tests in O_2 saturated 0.1 M KOH electrolyte, and (b) corresponding ORR or OER Tafel plots. (c, d) CV curves of $(Co,Fe)_3N$_R and $(Co,Fe)_3N$_2D measured in 0.1 M KOH electrolyte at the scan rates of 1 to 4 mV s^{-1} within a non-faradic voltage window. (e) Current density at the potential of 0.03 V (*vs.* SCE) as function of the scan rate.

Similar optimization of ORR/OER bifunctionality as well as increment in electrochemical double-layer capacitance (C_{dl}) can be observed in **Figure 4-6a, e**, in which the bifunctionality is defined by the voltage difference between ORR and OER branches typically collected at the current density of −2 mA cm^{-1} for ORR and 10 mA cm^{-1} for OER as compared in **Table 4-1**. The C_{dl} is calculated based on the CV curves in **Figure 4-6c, d** within a non-faradic voltage window, and the linear fitting slopes in

Figure 4-6e are used to determine their respective C_{dl} and the corresponding electrochemical active surface areas. As such, the expanded electrochemical active surface area is demonstrated by the $(Co,Fe)_3N$_2D. However, the Tafel slopes in **Figure 4-6b** reflect easing kinetics despite the slight rebounds in the latter two stages. On the basis of these electrochemical behaviors, it is preliminarily speculated that the transformation of $(Co,Fe)_3N$ during maturation in the initial cycles is a "double-edged sword", which increases bifunctionality and availability of catalytic sites, but slightly passivates the overall electrocatalytic kinetics.

Table 4-1 The key electrocatalytic parameters of electrocatalysts at different electrochemical stages.

Sample	$(Co,Fe)_3N$_R	$(Co,Fe)_3N$_1D	$(Co,Fe)_3N$_1C	$(Co,Fe)_3N$_2D
η_{ORR} at –2 mA cm^{-2} (V)	0.42	0.38	0.35	0.34
Tafel slope (mV dec^{-1})	57	74	69	63
η_{OER} at 10 mA cm^{-2} (V)	0.39	0.36	0.33	0.31
Tafel slope (mV dec^{-1})	75	86	80	77
$\eta_{ORR} + \eta_{ORR}$ (V)	0.81	0.74	0.68	0.65

To investigate the structural evolution, 2D WAXS patterns of the electrocatalysts at different stages were collected in **Figure 4-7a**. The original rings of $(Co,Fe)_3N$_R and blank carbon paper are generally maintained after electrochemical treatments, except for the two weak scattering rings at respective q values of 2.58 and 2.54 Å^{-1}. The synchrotron X-ray diffraction (SXRD) patterns in **Figure 4-7b** further validate the emergence of new phase, which can be indexed to the feature diffractions

of hexagonal CoOOH (PDF# 14-0673) as shown in **Figure 4-7c**.[174] Fe incorporation is also considered here, so the new phase is noted as (Co,Fe)OOH. As a widely-recognized insulator, the generation of the low-conductivity oxyhydroxide should be the reason for the easing kinetics observed in the electrochemical measurements.[175] Along with emergence of the new diffractions, another evolution is observed in peak intensity. When setting the graphitic (100) facet of carbon paper as reference, a gradual decrease is reflected in peak intensity of nitride-featured (101), which is diagnosed as partial vanishment of the original feature as a result of the phase transformation.

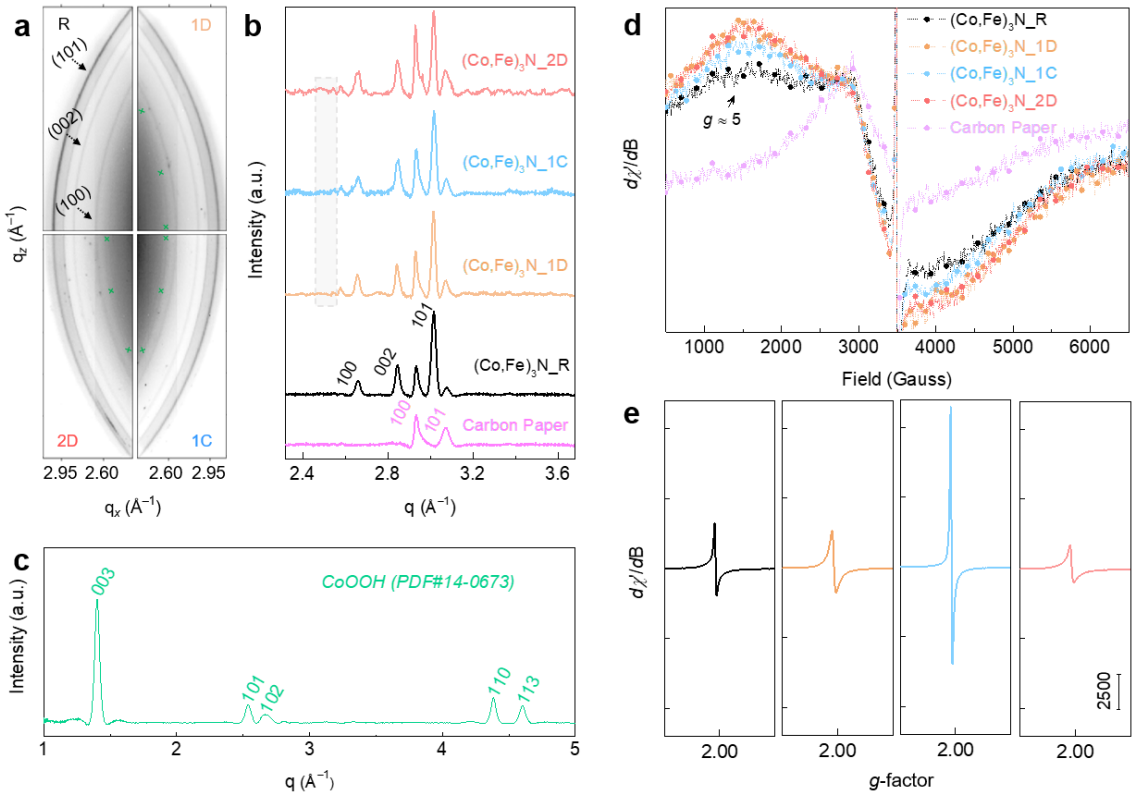

Figure 4-7 (a) 2D WAXS images, (b) integrated SXRD patterns including blank carbon paper, and (c) XRD pattern of CoOOH with a hexagonal layered structure (PDF#14-0673). (d, e) X-band EPR spectroscopies of electrocatalysts obtained at different electrochemical stages.

The variations in electronic state of the associated metal species are reflected in its resonant feature as observed by EPR. Specifically, the broad resonance peak at $g \approx 5$ (**Figure 4-7d**), commonly associated with EPR-active Co^{II} ($3d^7$) or Fe^{III} ($3d^5$),[176, 177] first experiences an intensity increment when the battery is discharged, then falls at charge and increases again at the second discharge. The Co^{II} emergence upon discharging is in agreement with the previous observation in ORR scans.[164] A reverse trend is observed with the free-electron resonance signal located at $g = 2.0$ in **Figure 4-7e**, which exhibits an intensity maximum at $(Co,Fe)_3N$_1C. Considering the EPR-silent feature of Co^{III} ($3d^6$) and Fe^{VI} ($3d^4$), the EPR signal fluctuation is ascribed to the temporal existence of Co^{IV} ($3d^5$) and the corresponding formation of oxygen vacancies.[176-178] Besides, the intensity difference between the two discharge stages confirms an irreversible weaken of nitride feature from continuous electrochemical control.

To monitor the evolution of the two metal ions, *operando* X-ray absorption spectra of the electrocatalyst during the first two discharge-charge cycles (**Figure 4-8d**) were collected. The XANES contour map of Co is displayed in **Figure 4-8a**, which shows four continuous and distinguishable periods. As the battery operation begins, a slow shift to higher energy of Co adsorption edge position is indicated by the characteristic contour line near 7720 eV in the first discharge. In the ensuing charging process, a step rise occurred at the very beginning, followed by steady increment of the edge position along with right shift and intensity enhancement of the white-line peak. Then, when initiating the second discharge, a small shift to lower energy is observed for both edge and main peak, nevertheless, the overall ascent sustains. Lastly, when the process reaches the second charge (2C), another step rise appears, followed by stabilization of the edge position and the white-line peak intensity at the highest level.

After completion of the two cycles, an overall 1.5 eV increase in the edge position is measured. This final edge position overlaps with CoOOH reference as shown in **Figure 4-9a**, indicating the presence of Co^{III} feature in $(Co,Fe)_3N$_2C. Based on theses XANES results, it can be stated that the valence state of Co continues to increase during the entire maturation process, which contradicts against the intensity fluctuation observed in EPR results. This conflict is due to the discrepancy in observation manners of the two analytical techniques, as XAS generally includes all signal contributions and monitors the average oxidation change.[126] When taking these electrochemically inaccessible Co^{II} into consideration, it would counteract the generated Co^{VI} in the shell to give an average Co^{III} feature at charged state. Another noticeable evolution is the gradual fading of the pre-edge peak at 7712 eV, implying weakening nitride feature as well as increasing Co occupation at dipole-forbidden octahedral sites in oxyhydroxide, which is responsible for the continuous increment of average Co oxidation. **Figure 4-8f, g** display *operando* Fe K-edge XANES contour map. Progressive reductions of the pre-edge peak intensity at 7114 eV and smooth increase of the white-line peak intensity are observed and complete at the beginning of the first charge. These changes are also resulting of surficial transformation from nitride to oxyhydroxide. Other than that, its constant edge position at about 7123 eV is diagnostic of the stable Fe^{III} feature in the cycling process.

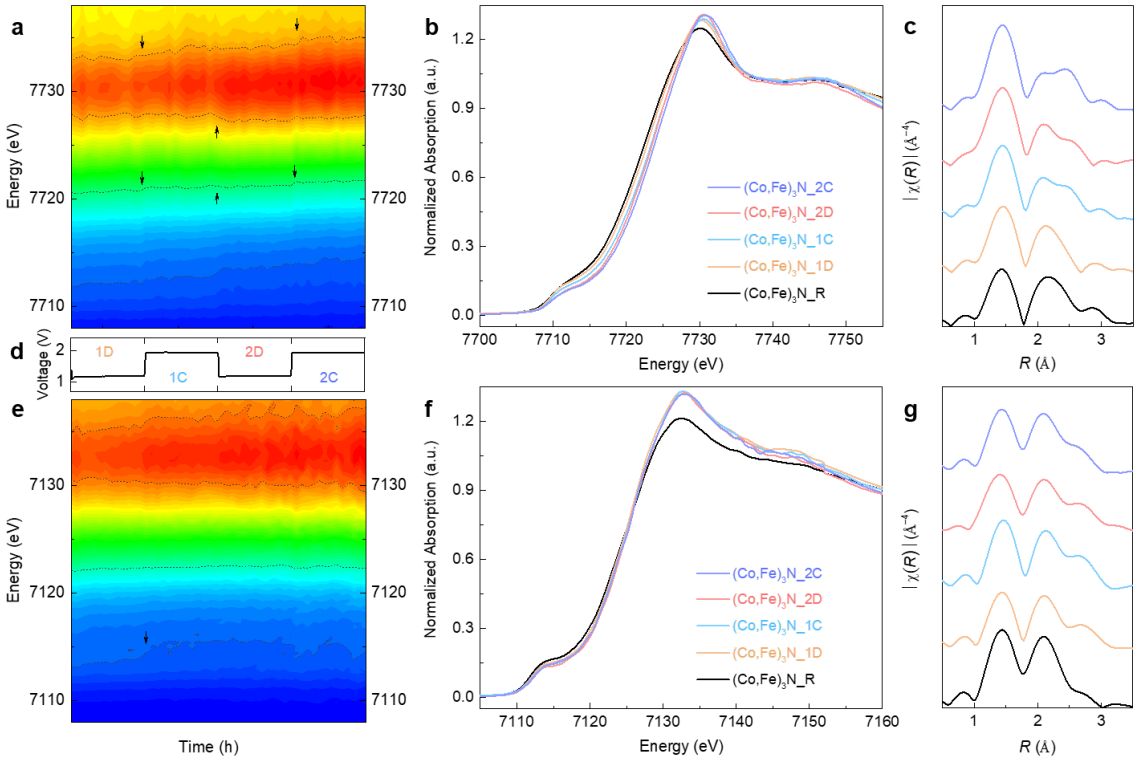

Figure 4-8 The *operando* XANES contour maps of (a) Co and (e) Fe K-edge, and the corresponding (d) voltage profile in the first two cycles; the red and blue contours respectively represent high and low adsorption intensities. *Operando* XANES and the k^3-weighted FT spectra of (b, c) Co and (f, g) Fe K-edge at different electrochemical stages.

According to previous studies based on three-electrode system, oxyhydroxide generation in OER always occurs near the catalyst surface.[157, 162, 163, 179] An analogous situation is also considered herein, *i.e.* the interfacial Co is electrochemically accessible while the bulk Co is isolated. This consideration is fully supported by XPS spectra at different depths in **Figure 4-10**. Two major differences are demonstrated in parallel and vertical comparison. The most significant difference in the parallel comparison is the presence and absence of the nitride-feature peaks at respective bulk and surface.[180] The peaks at 779 eV for Co $2p_{3/2}$ and the ones at 398 eV for N *1s* co-existed in bulk regions but are nondetectable on the surface. The O *1s* spectra shows an inverse phenomenon

with strong peak presence in shell regions while the negligible signal was shown in bulk. All indicates the different phases and compositions at the two depths. When conducting vertical comparison among spectra at the same depth, the bulk peaks shows relatively no resonance to electrochemical controls and negligible shifts are acquired for their positions. However, as for surficial elements, their peaks demonstrate visible shift along with cycling. The left shift of Co $2p_{3/2}$ as well as the satellite peak are shown in $(Co,Fe)_3N$_1C when comparing to $(Co,Fe)_3N$_1D, reflecting the increase of Co valency. Then, the three peaks shift back to their original positions for $(Co,Fe)_3N$_2D. Simultaneously, Co-O peak at about 530.7 eV in O *1s* also demonstrates a similar change upon cycling. The XPS analyses clearly confirm the hypothesis on the surficial location of electrochemically accessible Co. Combined with the EPR results, Co^{II} is identified in oxyhydroxide shell upon discharge, while Co^{IV} exists after the battery is charged.

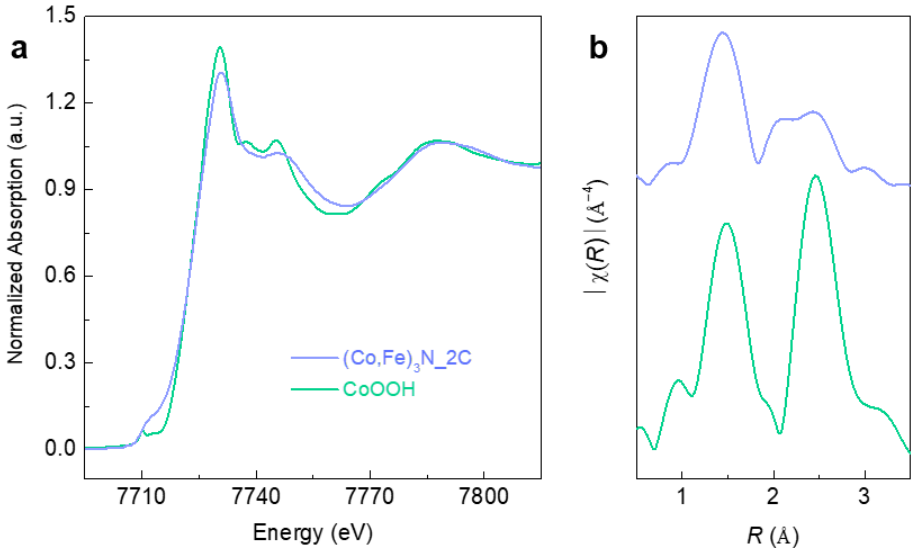

Figure 4-9 (a) Co K-edge X-ray adsorption near-edge structure and (b) k^3-weighted FT spectra comparison between CoOOH with $(Co,Fe)_3N$_2C.

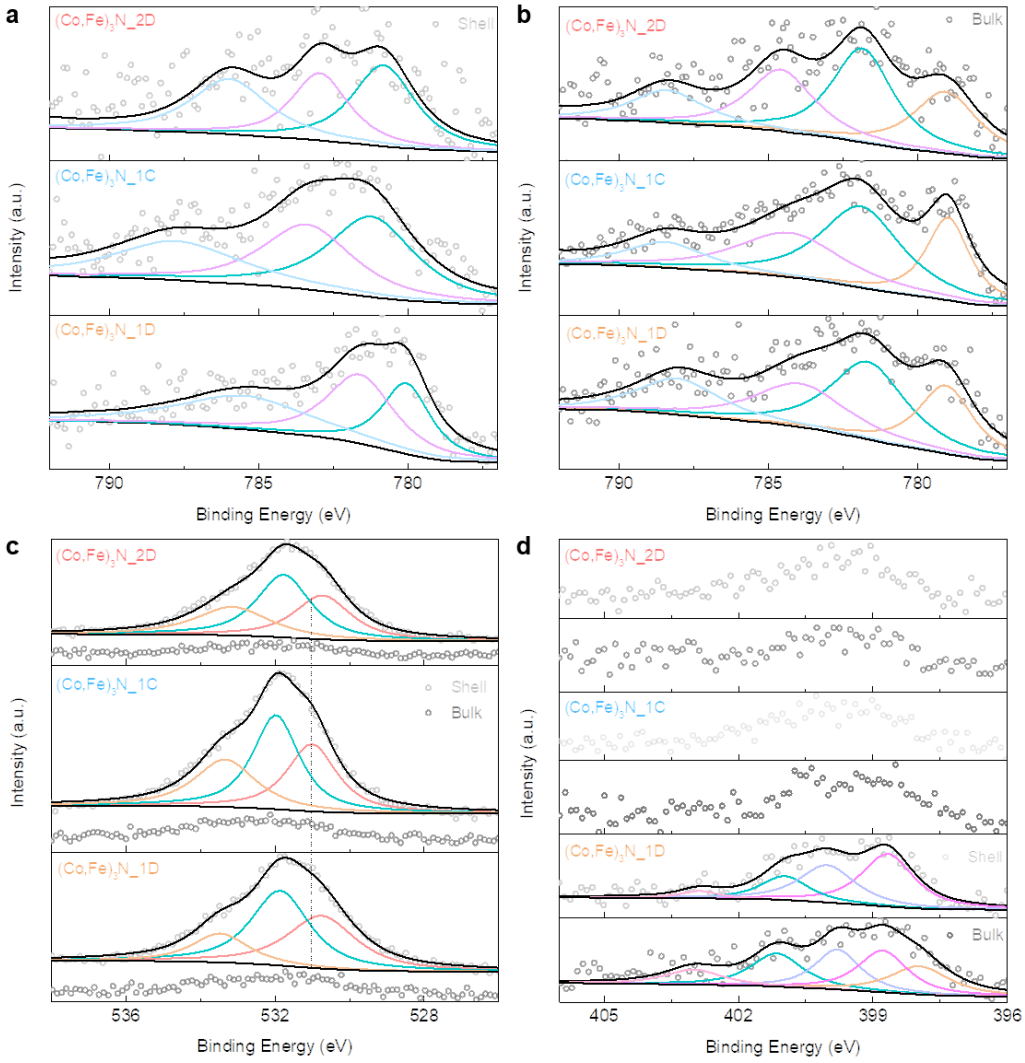

Figure 4-10 (a, b) Co *2p*$_{3/2}$, (c) O *1s* and (d) N *1s* high-resolution XPS spectra collected from surface or bulk. The bulk XPS information was collected after surficial Ar^+ etching for 20 nm.

The electrochemical influence on the coordination environment of metal ions is also captured using *operando* EXAFS result. Co K-edge k^3-weighted FT results are shown in **Figure 4-8c**. As the base spectrum, two major peaks centered at 1.4 and 2.1 Å are observed for $(Co,Fe)_3N$_R, respectively, representing the interatomic distance of Co-N and Co-metal shells in nitrides.[113] Comparatively, a slight right shift and intensity elevation of the Co-N peak is found in $(Co,Fe)_3N$_1D, while the peak of Co-metal shell reduces in intensity. These changes are symptoms for initiating oxyhydroxide

formation and overlapping of Co-N with Co-O shell at 1.4 Å. A new peak appears in $(Co,Fe)_3N$_1C at 2.5 Å, which can be assigned to the typical Co-metal shell in Co-containing oxyhydroxide as shown in **Figure 4-9b**.[179, 181] This new peak experiences slight position swings in the ensuing cycling process, corresponding to changes in the interatomic distance induced by valence variations of Co in oxyhydroxide.[179] Specifically, when the catalyst is charged, high-valence Co constrains its distance with neighboring metals or oxygens and causes left shift of the corresponding peaks. This maturation also causes the ascending of Co-O coordination number suggested by its increasing Co-O/N intensity. Regarding Fe K-edge k^3-weighted FT results, **Figure 4-8g** compares spectra obtained at each stage. As the feature Fe-metal distance in oxyhydroxide, a peak at 2.6 Å stands out in $(Co,Fe)_3N$_1D as evidence for oxyhydroxide generation. Aside for this variation, the spectra experience no significant changes in the following process.

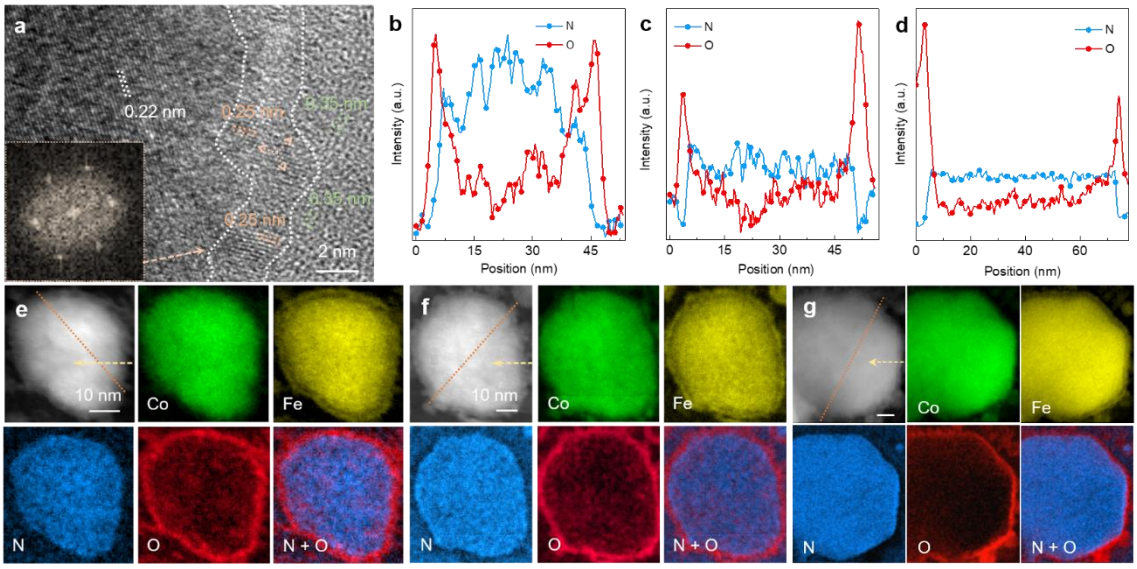

Figure 4-11 (a) HRTEM image at the edge region of a $(Co,Fe)_3N$_2D particle showing three regions with distinguishable lattice fringes; the inset shows the FFT pattern of the intermediate oxyhydroxide region. The EELS elemental line scans and mappings of (b, e) $(Co,Fe)_3N$_1D, (c, f) $(Co,Fe)_3N$_1C and (d, g) $(Co,Fe)_3N$_2D.

All the above characterizations point towards the fact that the surficial metal nitride experiences continuous transformation during cycling, but isolated analysis of the shell region is still required to open the "black box" and directly visualize the maturation process. Given such, several representative particles at different electrochemical stages were selected for TEM and EELS analyses. When comparing to $(Co,Fe)_3N$_R (**Figure 4-1e**), HRTEM image of $(Co,Fe)_3N$_2D in **Figure 4-11a** reveals the presence of a new intermediate layer with distinguishable crystal information between the nitride bulk and carbon coating layer. In this new layer, typical hexagonal lattice fringes are observed with a *d*-spacing of 0.25 nm, and its hexagonal symmetry is further verified by the FFT pattern. Except for these variations, the bulk metal nitride and the carbon layer are preserved after battery operation. Presence of this new layer is further reflected by a sharp O-rich and N-deficient boundary with a thickness of around 4 nm (**Figure 4-11e, f, g**), which is in agreement with the XPS analyses at different depths. These results confirm the generation of oxyhydroxide intermediate layer starting at the initial discharge, which maintains a similar thickness for both $(Co,Fe)_3N$_1C and $(Co,Fe)_3N$_2D. Another key point revealed is the relatively higher Fe content in the intermediate layer, this is explained by its lower electrochemical stability and supported by the completion of Fe pre-edge weakening at the very beginning of the first charge in *operando* XANES.

Ex-situ Co and Fe L-edge EELS analyses are conducted to locally decipher their chemical evolutions. Two key criterions are considered, including the peak energy position and the intensity ratio of $L_3/(L_2+L_3)$, or commonly stated as L_3 branch ratio.[182, 183] The **Figure 4-12a, b** display the electron energy-loss near-edge structure (ELNES) spectra acquired along the labeled arrows in **Figure 4-11e, f, g**. As shown in **Figure 4-12a**, the shells of $(Co,Fe)_3N$_1C and $(Co,Fe)_3N$_2D exhibit 1- and 0.7-eV right shifts

in their Co L_3 position respectively (**Table 4-2**), demonstrating their clear chemical differences in the shell and bulk regions. As for Fe L_3 peak position in **Figure 4-12b**, it remains relatively constant along the arrows. L_3 branch ratios were also calculated after background subtraction as plotted in **Figure 4-12c** and **Table 4-2**.[184] For the bulk region, a continuous downward trend of L_3 branch ratio is observed in Co L-edge spectra, which implies slight increase of average valence states during maturation. It should be noted that these bulk spectra represent the average chemical states due to the transmission probing manner of EELS, and therefore this tendency matches well with *operando* XANES results. However, a maximum valence is acquired at the shell region of $(Co,Fe)_3N$_1C that is even higher than the reported Co_3O_4 reference,[184] which then falls back in $(Co,Fe)_3N$_2D to a similar level as $(Co,Fe)_3N$_1D. Due to the *ex-situ* and high-vacuum TEM environment, the absolute valences of shell elements are relatively lower than their actual states in battery operation, but the shell-bulk difference and variation trend are still detected. Combining with the above analyses, the prediction on "shell-bulk" type configuration and periodic valence swings of surficial Co between Co^{II} and Co^{IV} during cycling is confirmed. Regarding Fe in oxyhydroxide intermediate layer, its L_3 ratios remain constant at a narrow range close to Fe^{III}.[185] Its feeble response to the electrochemical control stands with the XAS results, revealing the different roles of the two metals.

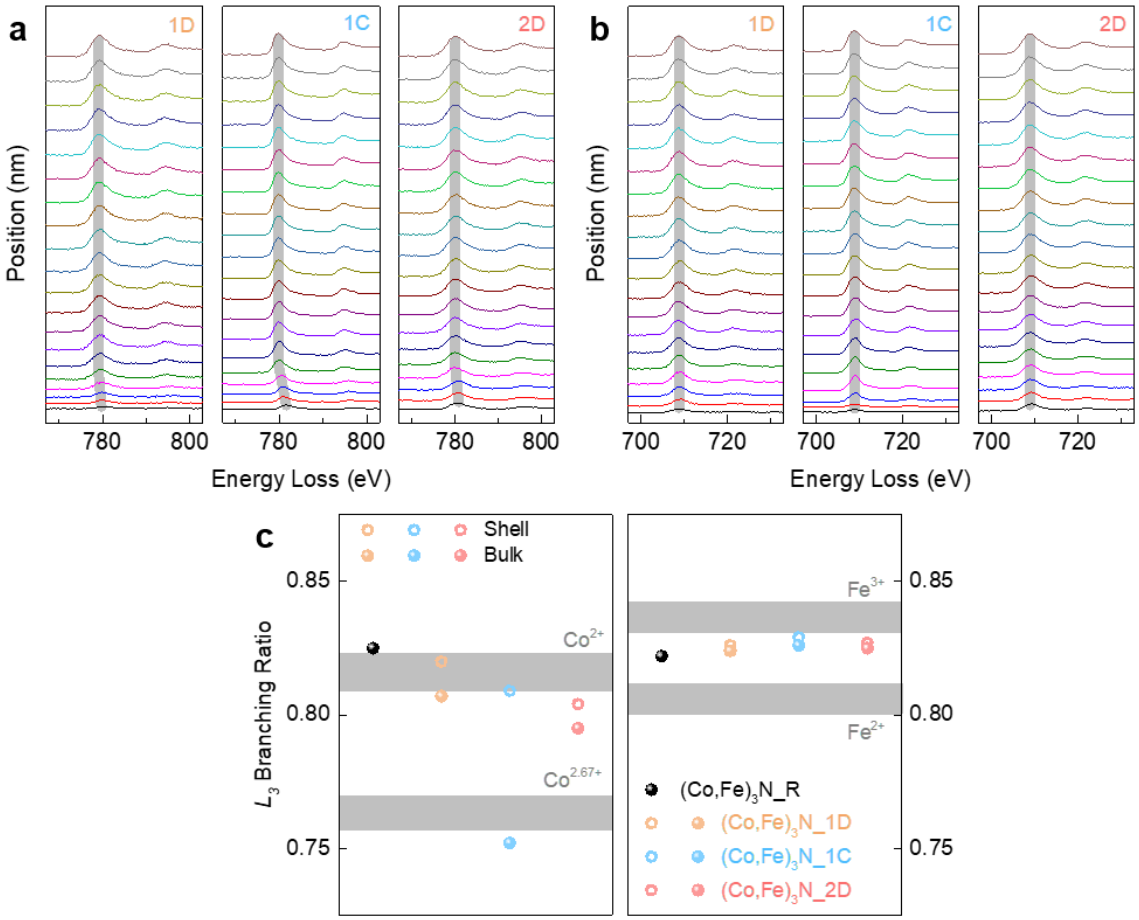

Figure 4-12 (a) Co and (b) Fe L-edge ELNES spectra along the arrows marked in Figure 4-11; (c) the L_3 branching ratio at different electrochemical stages, in which the reference location of valence states are based on literatures.[184, 185] Before ELNES spectra processing, all the background intensities of Co and Fe L-edge were subtracted by a step function of Arctan.[184] The L_3 branching ratio describes the variation between the L_3 and L_2 white-line peaks, and it is defined by the intensity ratio of $I_{L3}/(I_{L3}+I_{L2})$.

Table 4-2 ELNES analyses of electrocatalysts at different electrochemical stages.

Sample		$(Co,Fe)_3N$_1D		$(Co,Fe)_3N$_1C		$(Co,Fe)_3N$_2D	
		Bulk	Shell	Bulk	Shell	Bulk	Shell
Co L-edge	L_3-edge	779.1	779.6	779.8	780.8	780.0	780.7
	L_2-edge	794.4	794.8	794.8	795.8	795.5	795.7
	L_3/L_2 Intensity ratio	4.6	4.2	4.2	3.0	4.1	3.9
	L_3 Branching Ratio	0.820	0.807	0.809	0.752	0.804	0.795
Fe L-edge	L_3-edge	708.9	708.9	708.9	709.1	709.0	709.0
	L_2-edge	721.4	721.4	721.3	721.8	722.0	722.0
	L_3/L_2 Intensity ratio	4.7	4.7	4.7	4.8	4.7	4.8
	L_3 Branching Ratio	0.824	0.826	0.826	0.829	0.825	0.827

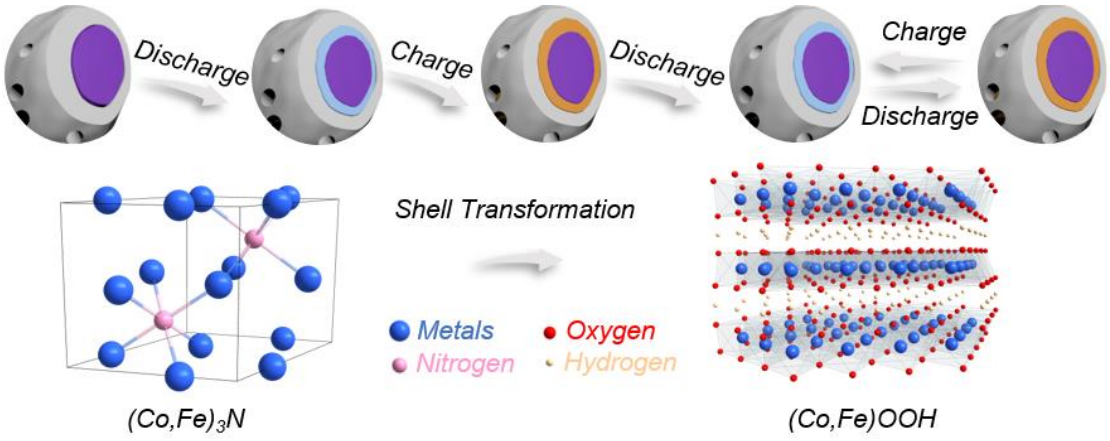

Figure 4-13 Schematic illustration for the maturation pathway of $(Co,Fe)_3N$_R with shell transformation from nitride to oxyhydroxide during cycling. The blue and orange

regions both represent the oxygen intermediate layers while the two colors demonstrate their different chemical states at discharge or charge.

As illustrated in **Figure 4-13**, the dynamic picture of metal nitride as bifunctional oxygen electrocatalyst in Zn-air battery operation is presented. Briefly, the as-prepared $(Co,Fe)_3N$_R is equipped with hierarchical morphology, optimal pore tunnels, and high electrical conductivity, so that outstanding electrochemical parameters are endowed. The maturation pathway launches immediately upon the initial discharge. Primary effect of this stage is generation of preliminary oxyhydroxide shell, which is accompanied by slight reduction of nitride features and emergence of Co^{II} and Fe^{III} features. It suggests the separation in trajectories of the shell and bulk regions, but this configuration is not yet matured, and Co related evolution is still in progress. Next, high-valence Co^{VI} emerges ostensibly in the 1C process along with appearance of oxyhydroxide-featured Co-metal interatomic shell in *operando* EXAFS spectra. Comparatively, the negligible change is demonstrated in bulk Co. The Co participation in oxyhydroxide shell is further aggravated in 2D, which ends when contradiction of increasing overall Co valency and falling surficial Co valence state is observed. At this stage, the maturation of the as-prepared metal nitride is completed, and the battery parameters stabilize. The large performance enhancement in maturation is ascribed to active sites transformation and corresponding expansion in electrochemical active area provided by oxyhydroxide shells. Nevertheless, as the insulator feature of the newly generated oxyhydroxide layer, the maturation is not a process without any downside. The low conductivity of this new phase does slightly passivate the overall electrocatalytic kinetics. Then, a cation rearrangement, *i.e.* increasing Co participation, in oxyhydroxide layer during maturation led by a dissolution/re-deposition mechanism should be responsible for the small kinetic

recovery in electrochemical measurements.[162] For the following cycles, although this "shell-bulk" configuration is maintained, periodic swings of the Co valence state continue to occur within oxyhydroxide shell.

At this point, with bimetal nitride as a general representation, a new recognition of dynamic electrocatalyst and its corresponding maturation process in rechargeable Zn-air battery are thoroughly presented. There are several points requires clarification. Firstly, physical factors such as air circulation and electrolyte permeation on carbon paper or Zn plate are excluded as origins for performance improvement due to the fading of noble-metal reference battery within the same conditions. Hence, the change in electrochemical performance is solely linked to the phase transformation of metal nitrides during the battery operation. Secondly, the oxyhydroxide shell in the matured configuration exhibits a hexagonal crystalline that significantly differs from the amorphous feature in previous report.[162] Its stable surface chemistry prevents further transformation after maturation and constrains the shell thickness to about 4 nm. This phenomenon combined with the settled battery parameters suggest termination of the lattice oxygen activation process.[163] Thirdly, several previous reports have proposed to combine the conversion reactions of principle elements with the oxygen reactions to form hybrid batteries.[186-188] From the above results, it is clear that the performance contribution of Co redox is too small to be reflected by any additional voltage plateaus, especially in long-period cycling tests. The periodic swings in the oxyhydroxide shell should be understood as an inherent process of galvanostatic cycling and the oxygen related redox is the sole dominator for the battery behavior. Fourthly, in this study, Co in the intermediate (Co,Fe)OOH layer is considered as the primary performance contributor due to its periodic variations during the electrochemical process, while Fe remain relatively idle. Although different pictures may be presented in nitrides with

other metal combinations, the unveiled maturation and the current-driven configuration is pervasive for them. Moreover, owing to the similar chemical reactivity, such process is also applicable for most of metal-based electrocatalysts in Zn-air battery, such as metals, alloys, oxides, phosphides and chalcogenides.[158-160, 162, 163] Finally, by gathering those fundamental understandings of electrocatalyst within battery operation, material design principles can be optimized accordingly. As for an ideal electrocatalyst for rechargeable Zn-air battery, two key components should be possessed besides rational geometrical optimization. One is a thin and highly active oxyhydroxide shell that serves as the primary activity contributor responsible for catalyzing the oxygen reaction in battery cycling, and another is a highly conductive bulk to maintain the electrochemical kinetics.

4.4 Summary

In this chapter, a bimetal nitride with secondary morphology and hierarchical porosity has been synthesized. When served as the electrocatalyst in rechargeable Zn-air battery, it not only delivers performance similar to precious benchmarks at its native stage, but also demonstrates a maturation process that leads to a maximum power density of 234 mW cm^{-2} and a discharge-charge voltage gap of 0.85 V at 30 mA cm^{-2} that lasted stably for more than 300 hours. This maturation process is also reproduced in a long-period cycling test, which achieves a voltage gap of 0.64 V at 5 mA cm^{-2} for over 750 hours cycling. More importantly, the underlying evolutions of metal nitrides upon battery operation are clearly visualized and explained using a wide range of characterization techniques. On the basis of the obtained experimental evidence, a concept of dynamic electrocatalyst is established with a current-driven “shell-bulk” configuration that is believed to be pervasive for most metal-based electrocatalysts. This mechanistic insight into the dynamic electrocatalyst paves a new avenue for future

innovations on electrocatalyst designs regarding rechargeable Zn-air battery applications.

5 Anion Evolution Induced Performance Improvement for Zn-air Battery

5.1 Introduction

The previous chapter establishes a "shell-bulk" configuration as the actual species for metal nitrides in rechargeable Zn-air battery cycling, and the active sites are isolated within the newly generated oxyhydroxide shell.[189] Then, when extending this maturation pathway to other categories of metal-based electrocatalyst, several uncertainties arouse and draw my further attentions. First, what is the chemical and structural states of generated oxyhydroxide in other elemental combinations within Zn-air battery condition? The oxyhydroxide shell of metal nitride in Chapter 4 is formed on the basis of the hexagonal CoOOH with Fe substitution. Then, my further interests involve validating whether the oxyhydroxide shell is still crystal in the absence of Co, or it will be an amorphous phase. Another motivation is driven here to break the Co reliance in battery science, due to its toxicity and cost concern.[49, 190, 191] As such, Ni with a nearly one-third price of Co provide a decent alternative with reasonable performance.[190]

The second uncertainty is about performance diversity among different types of metal compounds. If the assumptions were given on that the metal compounds follow the transformation pathway as described in Chapter 4 and the oxyhydroxide shell is a general active phase, their electrocatalytic performance should be at a relatively narrow range, especially for these with the same elemental composition, as it is mainly related to their native electric conductivity, composition and crystal variations in oxyhydroxide shells.[192-194] This point based on the metal sites is what the conventional electrocatalytic mechanism describes. However, a huge performance chasm exists in the comparisons

among different types of metal-based electrocatalysts. As a typical demonstration, the metal selenides are recently reported as a class of the most active OER electrocatalysts.[160, 195, 196] A huge performance margin is commonly obtained when comparing to other counterparts. For example, $(Ni,Co)_{0.85}Se$ was synthesized with a η_{OER} of 255 mV at 10 mA cm^{-1} within 1 M KOH electrolyte,[197] while, in another work, 350 mV was required for a flower-like $NiCo_2O_4$ to reach the same level.[198]

Therefore, there should be some other underlying interpretations for such performance advance of metal selenide, which raises the third uncertainty regarding the role of anion elements in these metal compounds, *i.e.* whether it is positive for electrocatalysis within the actual configuration. The previous research interests mostly focus on characterizing the chemical states and evolution of metal cations, while the contributions of those anion elements receive very limited efforts. Admittedly, the anion elements are considered as inactive in many cases, *e.g.* the metal nitrides in Chapter 4. The phase transformation at surface regions from $(Co,Fe)_3N$ to (Co,Fe)OOH results in O-rich and N-deficient distributions within the newly generated shells, which is supported by the high-resolution N *1s* XPS results. Except for that, no other new N species is generated superficially. It suggests the formation of oxyhydroxide shell occurs along with the surficial N loss into electrolyte, which exposes the electrocatalytic inactive feature of N in metal nitrides. The situation alters in perovskite oxides, in which lattice O were experimentally evident as accessible redox within the generated amorphous oxyhydroxide to provide additional OER activity.[162, 192, 199] The implementation of lattice O redox is also reported for spinel oxides.[163] As a well-know unstable OER electrocatalyst, the metal selenides also experience a surface transformation to oxides or hydroxide.[158] Hu *et al.* identified $NiFeO_x$ as the OER actual species for $Ni_xFe_{1-x}Se_2$ with a η_{OER} of 195 mV at 10 mA cm^{-1} within 1 M KOH.[160]

Next, Xue *et al.* further studied the phase evolution of $NiSe_2$ during OER chrono-potential treatment and demonstrated the generated NiOOH particles as the actual phase.[196] Besides the OER process, the application of selenides in Zn-air battery is also explored recently by Hu *et al*. and Gao *et al*.[200, 201] However, the influence of Se is still unrevealed.

In this chapter, to address above uncertainties, a metal diselenide, $(Ni,Fe)Se_2$, is synthesized and applied as the bifunctional electrocatalyst. As a direct comparison, an alloy-based counterpart (NiFe) is also prepared following a similar procedure without the selenization treatment. The systematic comparison between them highlighted the role of Se in performance improvement of Zn-air battery. At their native state, $(Ni,Fe)Se_2$ performs relatively inferior because of the expanded particle size and the reduced surface area during selenization. After the maturation, amorphous oxyhydroxide shells are generated in $(Ni,Fe)Se_2$ with the gradually weakened selenide feature. Besides the current-driven valence swings of performance-dominant Ni as the active sites, the oxidation of Se is also observed during battery cycling. With these generated Se cations, $(Ni,Fe)Se_2$ surpasses FeNi in various battery parameters. Herein, the maturation pathway of $(Ni,Fe)Se_2$ and the positive effects of Se on Zn-air battery operation will be discussed in detail in this chapter.

5.2 Experiment procedures

5.2.1 Material synthesis

A cation-carving method is also adopted here to prepare Ni and Fe containing LDH as the calcination precursor. First, Ni-based precursor were prepared by solvothermal reactions. 1.2 g of polyvinylpyrrolidone (PVP, K30) and 0.56 g nickel acetate tetrahydrate, $Ni(CH_3COO)_2{\cdot}4H_2O$, were dissolved into 80 mL of anhydrous

ethanol under ultrasonication to form clear solution. This mixed solution was transferred into a 100 mL Teflon-lined autoclave and treated at 120 °C for 400 minutes. After washing and centrifugation using ethanol at 7000 r.p.m for 3 times, the green powders of Ni-based solid polyhedrons were dried and obtained as the precursor for cation-carving process. Second, iron sulfate heptahydrate, $FeSO_4 \cdot 7H_2O$, was adopted as the graving agent for the cation carving process. 0.18 g of $FeSO_4 \cdot 7H_2O$ was dissolved into 100 mL deionized water within a 250 mL round-bottom flask under N_2 gas protection, followed by adding 100 mL anhydrous ethanol. In another beaker, 0.2 g of fresh Ni-based solid polyhedrons were dispersed into 20 mL anhydrous ethanol. Then, the second solution was transferred into the above round-bottom flask under magnetic stirring at 500 r.p.m. After reaction for 12 minutes, the Ni and Fe containing LDH was gathered after washing and centrifugation at 7000 r.p.m using respective ethanol and water for three times. Lastly, $(Ni,Fe)Se_2$ was prepared through calcination process with selenization. Prior to the calcination, a dopamine polymerization was used to coat the Ni and Fe containing LDH. In a typical experiment, 50 mg dopamine hydrochloride and 100 mg Ni and Fe containing LDH were dissolved into 0.01 M tris(hydroxymethyl)aminomethane buffer aqueous solution and stirred for 5 hours. The black powders were collected using centrifugation at 9000 r.p.m, washed with deionized water and ethanol, and dried in a convection oven overnight at 60 °C. As for selenization process, 20 mg of the black powders and 40 mg selenium powders were put at the two ends of ceramic boats, followed by loading the ceramic boats into tube furnace and keep the end with selenium at the upstream side of Ar gas. Then, the tube furnace was raised to 450 °C with a ramp rate of 2 °C per minute and stabilized for 2 hours. After cooling down to room temperature, the target metal diselenide $(Ni,Fe)Se_2$ was collected.

5.2.2 Material characterizations

The morphology and elemental composition were collected by field-emission scanning electron microscope (UltraPlus FESEMs, 20 kV) and field-emission transmission electron microscope (JEM-3200FS, 200 kV) equipped with an X-ray spectrometer detector (NORAN System 7 EDS). The N_2 isotherm was measured on a Brunauer-Emmett-Teller analyzer (Quantachrome Instruments QuadraSorb SI4), and the density-functional theory model was used to calculate the pore-size distribution. An X-ray diffractometer (Rigaku Ultima IV) with Cu Kα source and X-ray photoelectron Spectrometer (ESCALAB 250Xi) were used to determine the structural and chemical states of samples. Ar^+ bombardment was performed in XPS measurements to detect the bulk information, and C 1s peak at 284.84 eV was used as calibration reference.

Operando synchrotron X-ray diffractions (SXRD) were conducted at Brockhouse X-ray Diffraction and Scattering Beamline (High Energy Wiggler, BXDS-WHE) of Canadian Light Source (CLS) using a transmission mode. The photon energy was set at 35 keV and the X-ray wavelength is 0.359106 Å. The Zn-air battery protype was used directly as the *operando* setup. On the Zn anode, a hole with an approximate diameter of 0.4 cm was drilled to let photons go through, and Kapton™ tape (Nitto Americas, Inc.) was used to seal the electrolyte. 2D diffraction patterns were acquired consecutively with a time interval of 5 minutes during discharging and charging. These patterns were calibrated by a LaB_6 reference and integrated into 1D curves on General Structure Analysis System (GSAS) software.[168] As for the *operando* X-ray absorption (XAS) measurements, the same setup was utilized to collect spectra in fluorescence mode at Hard X-ray MicroAnalysis (HXMA, 06ID-1) beamline of CLS. The backside of GDL were placed facing incident photon and a 30 element Ge director. Each operando XAS spectrum was acquired after 20 minutes stabilization at each discharge

or charge state. The commercial Metal foils and their oxide references were also recorded. During the *operando* experiments, a Land battery tester (LAND-CT2001A, Land Electronic Co., Ltd., Wuhan) was used to discharge and charge Zn-air battery in a galvanostatic manner with a current density of 20 mA cm^{-2} and a cycle period of 4 hours.

5.2.3 Electrochemical measurements

Prior to the fabrication of Zn-air battery, catalyst powders were respectively dispersed into 0.2 wt% Nafion solution under ultrasonication. Then, this solution was sprayed onto carbon papers (SGL Carbon; Ion Power Inc.) as the GDL with an electrocatalyst loading of 1 mg cm^{-2}. The polished Zn plates and 6 M KOH solution dissolved with 0.2 M Zn acetate were utilized as the anode and electrolyte, respectively. The Land battery tester was also used in battery measurements. Battery cycling was conducted using a galvanic pulse method at a constant current density. The polarization curves of Zn-air battery were collected on a Gamry 5000E workstation. The polarization at different cycling states were freshly collected on the Zn-air batteries that were pretreated to specific electrochemical states.

5.3 Results and discussion

Native properties. The Ni-based precursor exhibits a morphology of solid polyhedrons as shown in **Figure 5-1a**. The formation of Ni-Fe LDH is also based on the cation-carving mechanism as illustrated in Chapter 4. Briefly, a consecutive ligand-release process occurs on Ni-based precursor followed by re-coordination with Fe^{II} source in aqueous solution.[189] After calcination, a secondary nanobox decorated with some nanoparticles is obtained in (Ni,Fe)Se_2 (**Figure 5-1b, c**). The size of these nanoparticles is over 200 nm in diameter. These large particles are generated during the

selenization process, and the uniform distribution of Fe, Ni, and Se is demonstrated within the particles as indicated in their elemental mappings and line scans (**Figure 5-1d, e**). The element ratio of Fe and Ni is also calculated to be 0.837 based on EDS result, and hence the general chemical formula of (Ni,Fe)Se_2 is determined as $Ni_{0.54}Fe_{0.46}Se_2$. Besides a thin layer of carbon coating, the HRTEM image in **Figure 5-1f** demonstrates clear lattice fringes with d-spacing of 0.298 nm that are typically indexing to the (200) facet of $NiSe_2$ and $FeSe_2$, which is further confirmed by the FFT patterns.

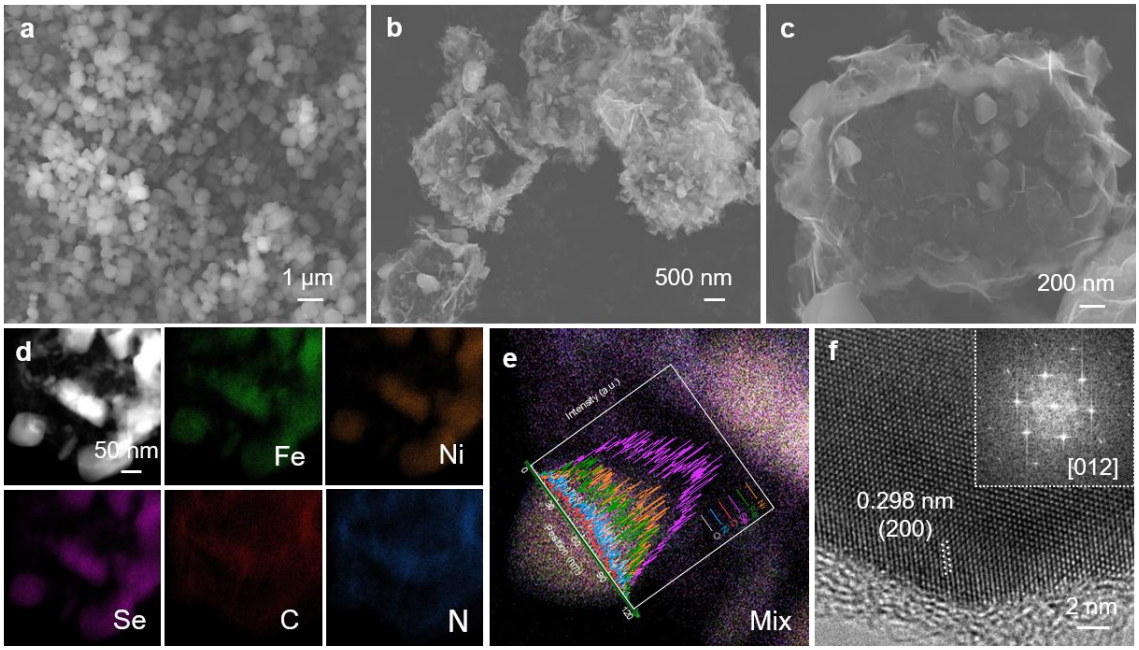

Figure 5-1 SEM images of (a) Ni-based precursor and (b) (Ni,Fe)Se_2. (d) The STEM images as well as the elemental mappings of (Ni,Fe)Se_2; and (e) the mixed distribution of Fe, Ni, Se, C, N, O, and the corresponding elemental line scans. (f) HRTEM image as well as the corresponding FFT patterns.

The surface area and porosity of (Ni,Fe)Se_2 is measured by N_2 adsorption and desorption isotherms as shown in **Figure 5-2**. A typical type-IV curve is obtained with a hysteresis loop, reflecting the hierarchical porosity of (Ni,Fe)Se_2, *i.e.* the co-existence of micropores and meso/macropores. The pore distribution profile in the inset of **Figure**

5-2 confirms its hierarchical porosity. The micropores are mostly generated from the carbon layer with defective features, while the meso/macropores originate from the nanobox morphology. Nevertheless, the selenization treatment results in the obvious size growth in primary nanoparticles of (Ni,Fe)Se_2 as demonstrated by the microscopic characterizations, and hence its surface area is limited to be 109 m^2 g^{-1}.

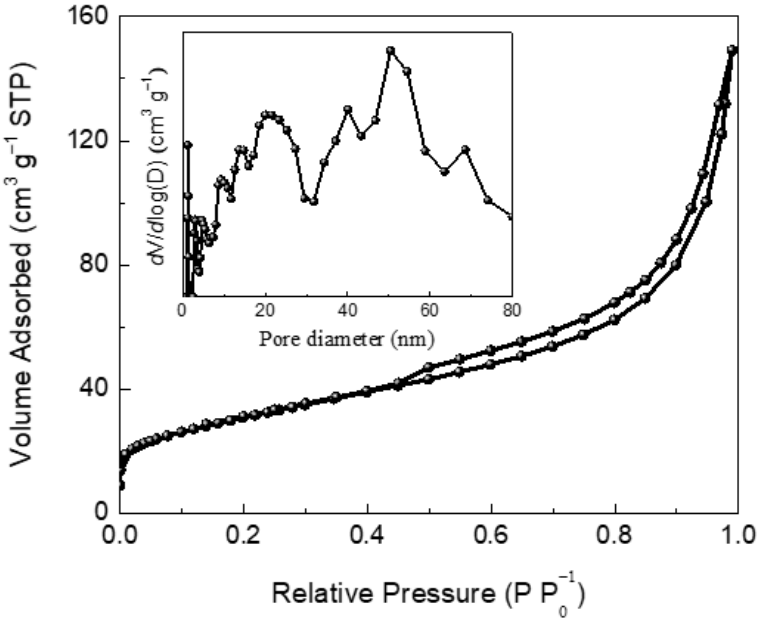

Figure 5-2 The N_2 adsorption and desorption isotherm of (Ni,Fe)Se_2 and its porosity distribution.

The crystal structure of (Ni,Fe)Se_2 is identified by XRD pattern as shown in **Figure 5-3a**. These diffraction peaks can be well indexed to the standard patterns of $NiSe_2$ (PDF#65-1843) and $FeSe_2$ (PDF#48-1881) references, while the absence of elemental Se signals reflects the complete selenization and no other impurity. As such, the pure phase Ni-Fe based diselenide is obtained. Due to the intrinsic metallicity, (Ni,Fe)Se_2 should be capable to enable high electrocatalytic charge transfer.[197, 202] When further taking its morphology feature into consideration, an relatively inferior battery performance is expected for (Ni,Fe)Se_2 due to its limited active sites.

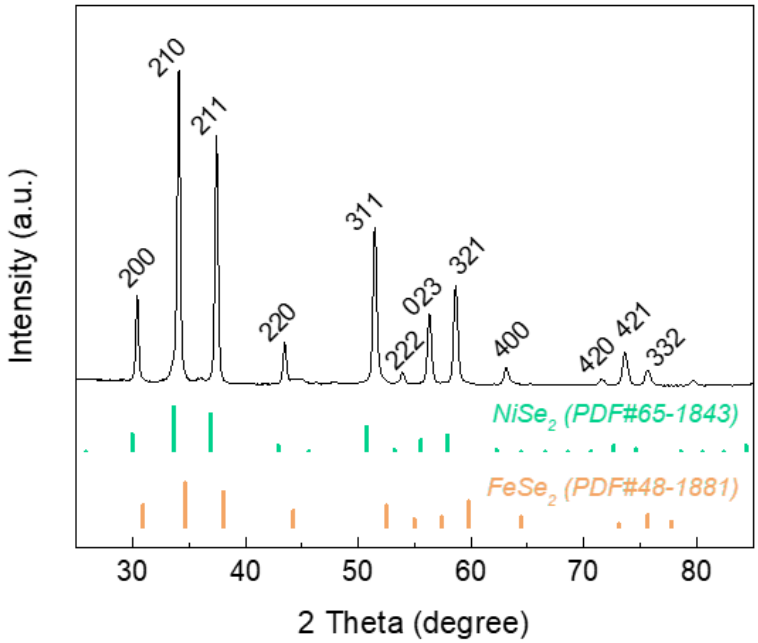

Figure 5-3 XRD patterns of (Ni,Fe)Se_2 as well as the respective reference patterns.

Electrochemical analysis. With aim to validate the electrochemical behavior, the Zn-air battery cycling is conducted on (Ni,Fe)Se_2 as illustrated in **Figure 5-4**. A Ni-Fe alloy based material is also synthesized as the performance counterpart to study the role of Se on battery performance. Both similarities and differences are demonstrated in such performance comparison. These two batteries both exhibit a activation process during the first several cycles, followed by gradual narrow in voltage gap (**Figure 5-5a, b, c**) and increment in power density (**Figure 5-5d, e**). Such processes should be attributed to the establishment and stabilization of the electrochemical active configuration within this period, coinciding with the maturation pathway as described in Chapter 4. As two well-known instable electrocatalysts under electrochemical conditions, the "shell-bulk configuration with the transformed oxyhydroxides are also considered here for both (Ni,Fe)Se_2 and NiFe. [158, 192, 203-205]

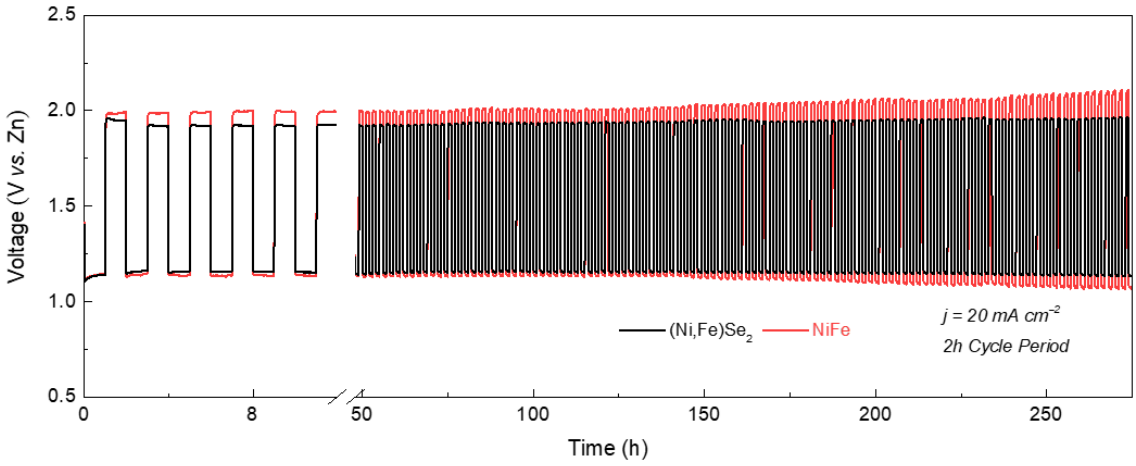

Figure 5-4 The cyclic performance of rechargeable Zn-air battery using $(Ni,Fe)Se_2$ or NiFe as bifunctional electrocatalyst at a current density of 20 mA cm^{-2} and a cycle period of 2 hours.

However, the performance difference as indicated in **Figure 5-4** clearly unveil the different pictures for their maturation pathway. Specifically, at the very beginning of the first discharge (1D), the battery with NiFe obtains a discharge voltage at 1.12 V (*vs.* Zn) that is slightly higher than the one using $(Ni,Fe)Se_2$ of 1.10 V. Although both discharge profiles exhibit upward shifts, the leading space of NiFe is shrunk during the 1D process and ended at less than 0.01 V. The inferior discharge performance of $(Ni,Fe)Se_2$ is attributed to its limited surface area, which verifies the performance expectations based on structural and morphological properties. Then, their positions are reversed in the first charge (1C). A charge voltage of 1.96 V is firstly obtained by the battery with $(Ni,Fe)Se_2$ that outperforms 1.98 V of NiFe, followed by further expansion in their difference to 0.4 V (**Figure 5-5a**). In the next several cycles, their battery parameters are gradually stabilized (**Figure 5-4** and **5-5b**), followed by maturation completion at about 5^{th} cycle. Then, the discharge and charge voltages of $(Ni,Fe)Se_2$ battery respectively reach 1.16 V and 1.92 V with a voltage gap of 0.76 V (**Figure 5-5c**). Meanwhile, a voltage gap of 0.85 V is obtained for the NiFe battery. As another

electrochemical feature for establishing matured configuration, a new plateaus at around 1.9 V attributed to the Ni redox couples in Zn-Ni battery systems emerges for both Zn-air batteries as marked in **Figure 5-5c**.[26, 49, 187, 188, 191, 206] Comparatively, as demonstrated in the inset, the NiFe battery exhibits relatively longer Ni oxidation plateaus and hence higher availability of Ni redox couples, which further confirms the size factor of (Ni,Fe)Se_2. Afterwards, when batteries reach the OER charging plateaus, an obviously lower voltage is performed by (Ni,Fe)Se_2 using the less metal sites. Considering the analogous situation in discharging, the existence of Se should be deciphered as the promoter effects for Zn-air battery cycling. Besides the reserved superiority in both discharge and charge performance, a higher cycleability is demonstrated by (Ni,Fe)Se_2 during the over 270 hours operation, while the NiFe battery experiences a gradual expansion in discharge-charge voltage gaps starting at 150th hour (**Figure 5-4**). It means that Se is also beneficial to stabilize the active phase upon long-term operation.

The scenario about the electrochemical behaviors reproduces in the polarization measurements on the two Zn-air batteries. At the raw state, the NiFe battery with a peak power density of 135 mW cm^{-2} outperforms (Ni,Fe)Se_2 battery of 126 mW cm^{-2} in the discharge branch, while a higher charging current density is achieved by (Ni,Fe)Se_2 battery under the same cut-off voltage. After 5 cycles, both batteries exhibit performance improvement in their battery parameters. In comparison, a wider range of increase is offered by the one using (Ni,Fe)Se_2 to achieve a power density of 212 mW cm^{-2}, while it is 160 mW cm^{-2} for NiFe. As for the charging behaviors, similar to the galvanostatic charge curves at 5th cycle (**Figure 5-5c**), the arched polarization curves are obtained at the low current density region, further suggesting the enabling of Ni-based redox couples upon cycling. Besides, a higher charging current density is

obtained by (Ni,Fe)Se_2 battery to achieve a fixed voltage. At this point, it can be speculated that the participation of Se is the game-changing factor for the electrochemical behaviors of (Ni,Fe)Se_2 in rechargeable Zn-air battery.

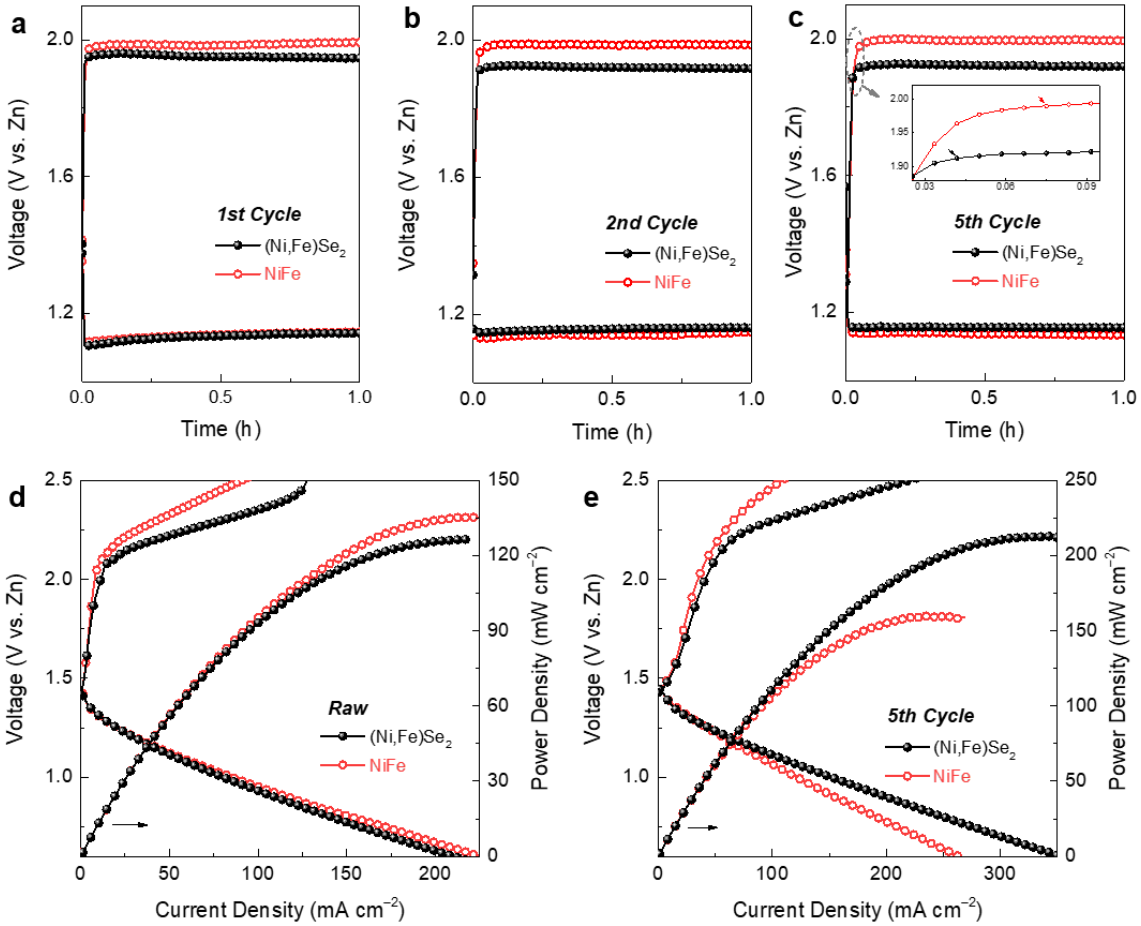

Figure 5-5 The comparisons in discharge-charge profiles of Zn-air battery with (Ni,Fe)Se_2 or NiFe at (a) 1st, (b) 2nd, and (c) 5th cycle; their corresponding polarization curves as well as the power density (d) at raw state and (e) after 5 cycles.

Structural evolution. To verify the proposed speculations, *i.e.* actual configuration upon battery cycling and promoter effects of Se, in electrochemical analysis, *operando* XANES experiments upon the first two-cycle cycling in Zn-air battery are conducted to unveil the detail evolution on each element (**Figure 5-6**). The first two cycles are segmented into five periods along the time axis based on different

electrochemical states, including the raw state (Ni,Fe)Se_2_R, the first discharged (Ni,Fe)Se_2_1D, the first charged (Ni,Fe)Se_2_1C, the second discharged (Ni,Fe)Se_2_2D, and the second charged (Ni,Fe)Se_2_2C. As shown in Ni K-edge XANES spectra (**Figure 5-6a**), its raw states exhibit a hump peak at about 8341 eV. This park is attributed to the selenide feature, which is also observed in Fe K-edge of (Ni,Fe)Se_2_Raw (**Figure 5-6b**) and reported for other selenides in literatures.[196, 200] Upon the battery operation, the weakening of this hump peak is observed for both Ni and Fe K-edges, suggesting their participation into the phase transformation and the formation of electrochemical response layer at the triphasic interfaces. However, two different pictures for Ni or Fe evolutions reflect their different roles in battery operation. Ni in the newly generated oxyhydroxide layer is characterized as the electrocatalytic sites due to its current driven evolution. In detail, besides the gradual fading of selenide feature, the edge position of Ni in **Figure 5-6a** experiences a positive shift during the 1D and 1C process, followed by shift back in 2D and finally reach the highest level at 2C. When comparing to the commercial references, the edge position of (Ni,Fe)Se_2_2D is between Ni^{II} in NiO and Ni^{III} in Ni_2O_3, while (Ni,Fe)Se_2_2C is even higher than the Ni^{III}. Taking the electrochemical inaccessible Ni into account, Ni^{III} and Ni^{IV} sites in oxyhydroxide is unveiled as the actual species responsible for the discharge and charge performance, respectively. While the Fe K-edge is relatively electrochemical inert as shown in **Figure 5-6b**, as it maintains a Fe^{III} feature referring to Fe_2O_3 during the two cycles. On basis of the above *operando* XANS results, the phase transformation with fading of selenide feature and the periodic valent swings of Ni sites within the electrochemical response layer are validated.

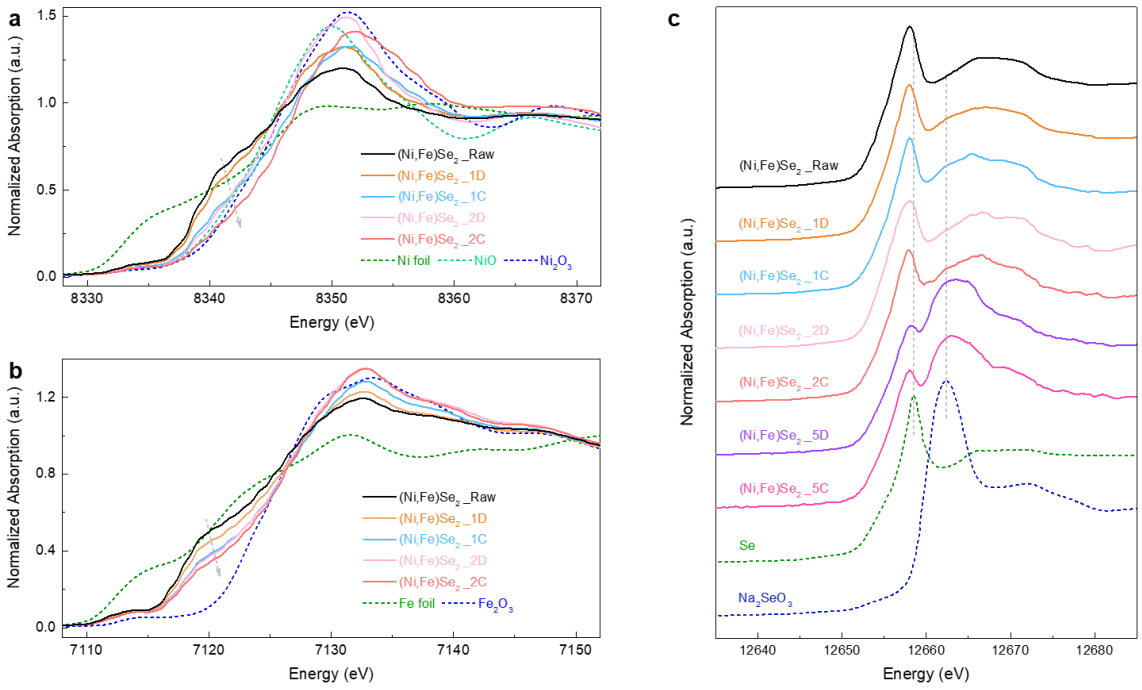

Figure 5-6 The *operando* XANES spectra of (Ni,Fe)Se_2 for (a) Ni K-edge, (b) Fe K-edge and (c) Se K-edge during Zn-air battery. The K-edges of respective metal foils and oxides are also shown as the standard reference of their oxidation. As for the denomination of these samples, the number in their name postfix reflects their specific cycle number, while the letter of D or C represents the discharge or charge state.

In addition to the two metal elements, the evolution of Se is also captured by operando XANES spectra in **Figure 5-6c**. As shown, a typical anionic feature is demonstrated by (Ni,Fe)Se_2_Raw with a sharp white-line peak at 12658 eV and two overlapped broad humps due to the multiple scattering of photoelectron. The position of the white-line peak is lower than Se^0 powders and consistent with the Se^{II-} systems in literatures.[207, 208] Upon battery operation, the continuous shrink of this peak suggests the deceased concentration of anionic Se in (Ni,Fe)Se_2, while a new peak at about 12663 eV gradually emerges between the original white-line peaks and humps. When extending to the 5th cycle, the new peak has become the dominant feature for both discharge and charge states. While Se^{II-} features still exist as the evidence of

electrochemically inaccessible bulk. The energy position of the new peak coincides with the white-line peak of $Na_2Se^{IV}O_3$ reference. When comparing the spectra between (Ni,Fe)Se_2_5D and (Ni,Fe)Se_2_5C, no visible shift is observed for all these peaks, reflecting its inert response to electrochemical conditions within the matured configuration. The direct evidence confirms the oxidation of the Se^{II-} to Se^{IV} during the maturation pathway, and then its chemical states maintains stable in the following cycling.

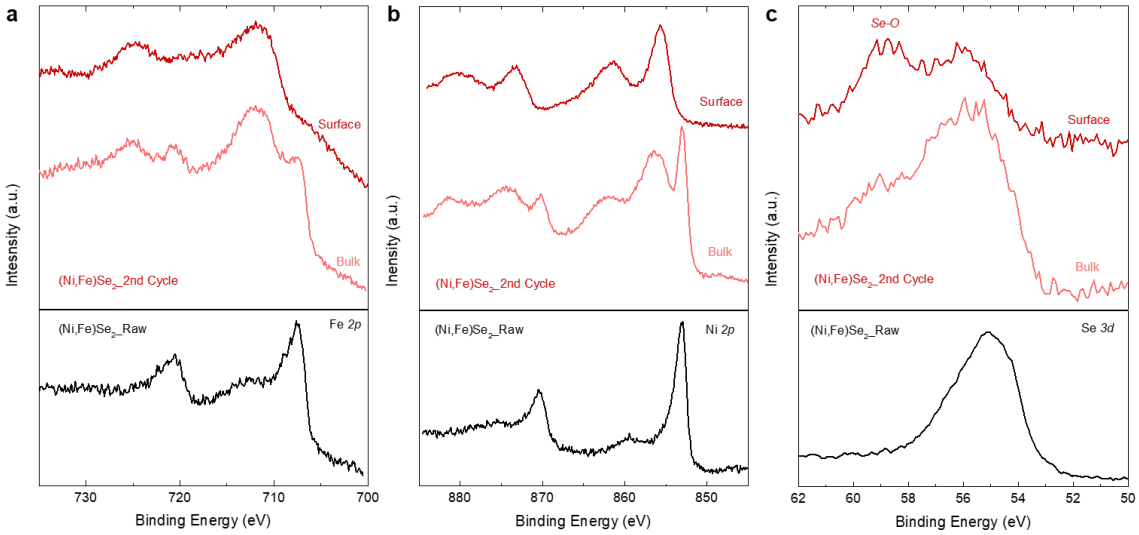

Figure 5-7 The high-resolution (a) Fe, (b) Co, and (c) Se XPS spectra collected at surface or bulk regions of (Ni,Fe)Se_2 after the 2nd cycle in comparisons with their raw states. 20 nm surficial Ar^+ etching was conducted on the sample to obtain bulk information.

The *operando* XAS is not a surface-sensitive technique and monitors the average chemical states of each element. Therefore, to further validate the formation of "shell-bulk" configuration for (Ni,Fe)Se_2, high resolution XPS spectra combined with Ar^+ bombardment is conducted to gather the surface and bulk information of samples pretreated to the 2nd cycle. As shown in **Figure 5-7a, b**, the selenide feature peaks of Ni and Fe are solely detected at the bulk regions, while the surface elements are fully

oxidized. High resolution Se XPS spectra confirm the emergence of Se-O peak at surface in addition to the original *3d* peak. In literatures, on basis of the similar XPS observations, the generation of SeO_x species on selenides have been concluded after OER.[160, 201, 209] Except that, no other experimental evidence has been provided for SeO_x generation. Also, this conclusion cannot offer a convincing explanation for its performance superiority in comparison to NiFe.

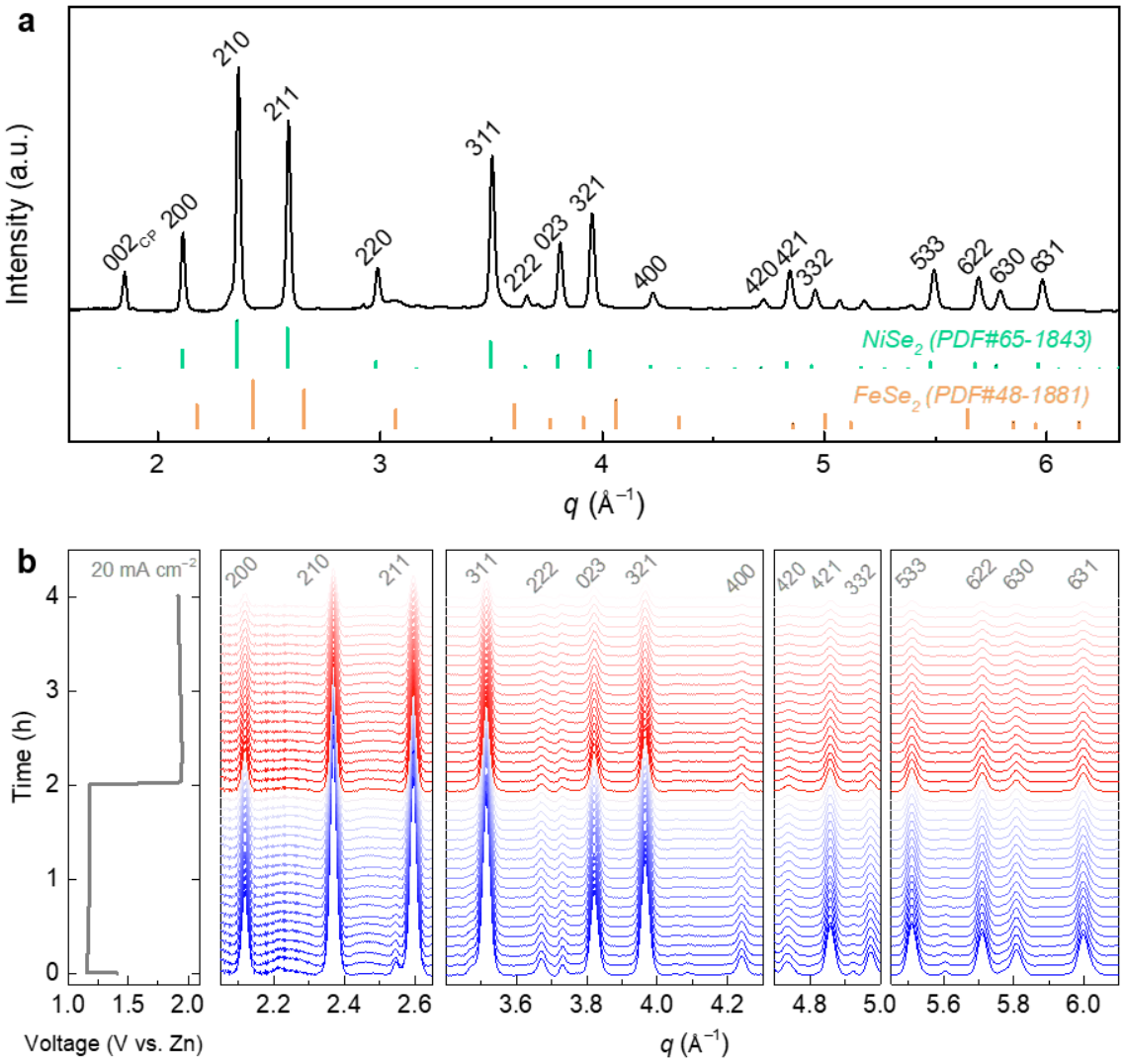

Figure 5-8 (a) SXRD pattern of (Ni,Fe)Se_2 at the raw state as well as the corresponding standard references of $NiSe_2$ (PDF#65-1843) and $FeSe_2$ (PDF#48-1881). (b) Its discharge-charge profiles of the first cycle in Zn-air battery and the corresponding *operando* SXRD patterns.

Then, the *operando* SXRD experiment is carried out to detect the phase transformation or any new phase formation in (Ni,Fe)Se_2 during the first-cycle operation in Zn-air battery. **Figure 5-8a** shows the SXRD pattern of (Ni,Fe)Se_2_Raw before cycling. Besides the typical graphitized diffractions from carbon paper, it matches with powder XRD pattern (**Figure 5-3a**) and is well indexed to the standard references of diselenides. During the first cycle, all the diffractions maintain at their original positions with negligible shifts. These fixed diffractions are attributed to the electrochemical inaccessible bulk regions in the "shell-bulk" configuration of (Ni,Fe)Se_2. Meanwhile, their intensities are noticeable decreased, which demonstrates the weakened selenide feature in accordance with the *operando* XANES results. However, no other new diffractions appear as the evidence for oxyhydroxide formation. It means the generated oxyhydroxide shell exhibits an amorphous phase, which is different from the nitride derived oxyhydroxide with hexagonal crystalline as indicated in Chapter 4. More importantly, the generation of SeO_x is also undetectable under Zn-air battery operation. Combined with the observation of Se^{IV} species and electrochemical behavior of (Ni,Fe)Se_2, it would be more proper to describe as Se substitution within the amorphous oxyhydroxide, other than the heterogeneous SeO_x.

5.4 Summary

In this Chapter, a metal diselenide, (Ni,Fe)Se_2, with secondary morphology and hierarchical porosity is designed and prepared as bifunctional electrocatalyst to power rechargeable Zn-air battery. By using multiple *operando* techniques, its dynamic evolution is showcased in detail upon battery operation. Several points should be mentioned when applying the established maturation pathway and "shell-bulk" configuration in the previous Chapter to (Ni,Fe)Se_2, which makes it distinguishable with the bimetal nitrides. First, the amorphous oxyhydroxide shell is generated along

with weakening selenide feature. Second, Ni plays as the electrocatalytic active site in such elemental combination of Ni and Fe, and meanwhile itself can offer redox plateaus in battery cycling. Third, within the generated oxyhydroxide layer, the periodic valence change of Ni is observed, *i.e.* Ni^{III} or Ni^{IV} is responsible for discharging or charging performance, while Fe maintains at trivalent state. More importantly, besides the metal cations, another primary contribution of this Chapter is the observation of Se evolution. Upon Zn-air battery operation, the anionic Se is partially oxidized to Se^{IV} and co-existed with Ni and Fe in the newly generated amorphous layer. *Operando* SXRD patterns reveal the absence of any new species, including the SeO_x, and hence the (Ni,Fe)OOH with Se substitution is considered as the performance contributor in the actual configuration of $(Ni,Fe)Se_2$. The positive influence of Se substitution on the battery parameters is highlighted by its comparison with the NiFe counterpart. Specifically, $(Ni,Fe)Se_2$ exhibit an inferior native electrocatalytic performance in Zn-air battery with a power density of 126 mW cm^{-2}, due to the selenization induced growth in particle size. In comparison, the battery using NiFe as the bifunctional electrocatalyst performs 135 mW cm^{-2}. Then, both Zn-air batteries demonstrate a maturation period for the establishment of actual configuration in the first several cycles, followed by the gradual stabilization in battery parameters. Then, $(Ni,Fe)Se_2$ battery reaches a power density of 212 mW cm^{-2} at 5^{th} cycle, which is higher than NiFe battery of 160 mW cm^{-2}. Therefore, the Se evolution and the corresponding Se^{IV} substitution within amorphous oxyhydroxide should be responsible for such large performance margin of $(Ni,Fe)Se_2$, and the improved battery cycleability.

At this point, the above uncertainties regarding the dynamic evolution in different metal combination and the role of anionic element are all addressed. When metal selenides serve as the bifunctional electrocatalyst for rechargeable Zn-air battery,

Se also gets involved into electrochemical evolution and plays a role as the booster to improve the electrocatalytic process at the nearby active sites. These fundamental understandings can provide new insight into electrochemical behaviors at air cathode and may inspire some further design strategies on basis of anion modulation.

6 Conclusions and Recommendations

In the present thesis, different types of metal-based materials, including spinel oxide (Chapter 3), metal nitride (Chapter 4) and metal diselenide (Chapter 5) have been developed and served as bifunctional electrocatalysts to power rechargeable Zn-air batteries. These electrocatalysts are designed based on the principles, *i.e.* to increase the accessibility and intrinsic activity of electrocatalytic sites. By using virous characterization techniques, their morphological and structural features at the raw states have been studied. The attentions are also paid to understand their electrochemical behavior and the underlying structural evolution.

In Chapter 3, an in-situ coordinating strategy is proposed to amend the porous structure of multi-shelled materials with tuneable composition. It is achieved by inducing a homogenous distribution of metal cations within carbonaceous frameworks, rather than densely gather on the surface. After template removal, a hierarchical porosity is obtained on the double-shell spinel, which is characterized by surface analysis and visualized through 3D tomography. Such porosity is beneficial for increasing the number of active sites and accelerating reactant transfer towards/away these sites. Meanwhile, this strategy also opens the feasibility for composition alteration. As such, Mg is substituted into Co_3O_4 at relatively low amount. Although itself is inactive for electrocatalysis, the Mg substitution can positively influence the electrocatalytic performance though two aspects, including the increase in the overall electrical conductivity and formation of buffer zones with lowered lattice alkalinity. With these merits, such Mg substituted spinel with hierarchical porous doubled-shelled structure outperforms either limited porous or Mg-free counterparts in electrocatalytic measurements. When it is assembled into Zn-air battery, a power density of 125 mW

cm^{-2}, a discharge-charge voltage gap of 0.8 V and cycleability of over 200 hours are demonstrated.

Chapter 4 showcases a Co-Fe nitride with intrinsically metallic nature as a new candidate for electrocatalyst. More importantly, it can provide a clear background to record the phase transformation during battery cycling. The bimetal nitride is prepared through a cation-carving method and presents a morphology of hollow nanocuboids with hierarchical porosity. As a result, its native state provides a power density of 133 mW cm^{-2} and a voltage gap of 1.08 V at 30 mA cm^{-2}. Then, after a period of maturation, the battery parameters are gradually optimized and stabilized at 234 mW cm^{-2} and 0.85 V. To understand the reasons underlying such performance upgrade in preliminary cycling, the structural evolution of nitride is visualized by means of *operando* spectroelectrochemistry and microscopic studies. The experimental evidence unveils a surficial phase transformation from nitride to oxyhydroxide with hexagonal crystalline. Before the maturation completion, a self rearrangement is also detected within the new phase. As such, a concept of "dynamic electrocatalyst" is developed herein, and a "shell-bulk" configuration is established as the actual species of nitride under Zn-air battery operation. Besides, Co sites within oxyhydroxide shell are isolated as the electrocatalytic active sites due to its periodic valence variation, *i.e.* Co^{II} for discharging and Co^{IV} for charging.

In Chapter 5, the concept of "dynamic electrocatalyst" is further extended to a Ni-Fe diselenide, and the role of Se in electrocatalysis is studied. This diselenide with intrinsic metallicity is prepared through selenization upon calcination, which result in large primary particles and relatively low surface area. Despite its hierarchical porosity, such size factor is not ideal for oxygen electrocatalysis, and hence an inferior native discharge performance is provided, when comparing to the alloy-based counterpart

with the same metal composition. However, when the maturation is completed, their positions in the performance comparison are reversed. At the 5th cycle, the diselenide achieves a power density of 212 mW cm^{-2} and a discharge-charge voltage gap of 0.76 V at 20 mA cm^{-2}, outperforming the counterpart of 160 mW cm^{-2} and 0.85 V. Besides, a cycleability for over 270 hours is obtained by diselenide, while the alloy reflects a gradual expansion in voltage gap starting at around 150th hours. To get insights into these electrochemical behaviors, *operando* XANES is carried out to record the evolution of each element. Similar to the situation in nitride, the surficial phase transformation occurs with the weaning of diselenide feature. The periodic valence variation of Ni is observed while Fe remains electrochemical inert, and hence Ni within oxyhydroxide is considered as the active site. More importantly, the oxidation of Se and the emergence of Se^{IV} are also observed. According to *operando* SXRD patterns and XPS spectra at different depths, an amorphous Ni-Fe oxyhydroxide with Se substitution is generated as the shell in the actual configuration. Se substitution is considered as the reason for the performance profits in the comparison with alloy-based counterpart.

Based on these above understandings obtained in this thesis, some recommendations can be provided for further research regarding metal-based electrocatalyst for rechargeable Zn-air battery.

i) *Further optimization on the nanostructure of electrocatalyst.* According to design principles for electrocatalyst, the nanostructure engineering can open possibilities to increase surface area, promote electrolyte accessibility and accelerate reactant diffusion. In this thesis, several nanostructures have been designed and obtained, but there is still a lot of room to make some differences. For example, the primary particle size is around 20 nm for $(Mg, Co)_3O_4$, around 50 nm for $(Co,Fe)_3N$

and over 200 nm for (Ni,Fe)Se_2. By diminishing the particle size, it is expected to further increase the number of active sites and hence optimize the electrocatalytic activity. Meanwhile, some other novel nanostructures with hierarchical porosity are also expected.

ii) *Further exploration on the oxyhydroxide formation in the actual configuration.* The present thesis reveals that oxyhydroxide species is generated through surficial phase transformation of metal-based electrocatalysts, and the "shell-bulk" configuration is the actual state under Zn-air battery operation. The respective role of the shell and bulk components is also discussed here. However, the oxyhydroxide shell of nitride in Chapter 4 and the diselenide in Chapter 5 are both obtained passively under electrochemical conditions, which constrains the feasibility to regulate its composition and structure. The rational ratio between the shell and bulk also remains unexplored. Therefore, some novel design strategies to intentionally incorporate the active shell and conductive bulk within a multi-phase electrocatalyst are highly desired. With the direct synthesis of the actual configuration, the optimal elemental composition and shell/bulk ratio can be investigated for further performance optimization on Zn-air battery in both activity and durability.

iii) *Re-consideration on the active species of electrocatalyst and role of anion elements.* As exposed in this thesis, the actual state of electrocatalyst is different with its raw state, and the oxygen electrocatalysis is a dynamic process. Therefore, although a huge number of electrocatalysts have been reported for Zn-air battery, it would be not accurate to treat their raw properties as the sole criterion for battery performance. Besides, the evolution of anion elements is also required additional attentions. Unlike the lattice O, Se do not directly get involved into electrocatalysis, but it can positively influence the nearby Ni sites. Therefore, in the future research, it should be very careful

to identify the active sites and actual configuration, and the contribution of anion element should be also taken into consideration.

iv) *Further investigation on operando techniques to obtain in-depth understanding on electrocatalytic mechanism.* Some highly active species, such as Co^{4+}, only exist under electrochemical conditions. Their exposure in air for ex-situ characterizations usually contributes to distorted results. The current established techniques that are operando available mainly includes XRD, XAS, Raman and SEM, and more advanced techniques, such as EPR and TEM, are highly expected to provide more comprehensive results. The key lies in the design of aqueous cells as the *operando* setup for implementation of new operando techniques. Besides, in this thesis, *operando* XAS and XRD experiments have been conducted to study these active species and the corresponding evolution pathway during initial several cycles. However, challenges remain to understand the degradation mechanism of electrocatalyst during prolonged cycling. Extended battery cycling under harsh environment combined with operando characterizations is also highly recommended.

Reference

1. M. Armand; Tarascon, J.-M., Building better batteries. *Nature* **2008,** *451*, 652-657.

2. Li, M.; Lu, J.; Chen, Z.; Amine, K., 30 Years of Lithium-Ion Batteries. *Adv. Mater.* **2018,** *30*, e1800561.

3. Liu, J.; Bao, Z.; Cui, Y.; Dufek, E. J.; Goodenough, J. B.; Khalifah, P.; Li, Q.; Liaw, B. Y.; Liu, P.; Manthiram, A.; Meng, Y. S.; Subramanian, V. R.; Toney, M. F.; Viswanathan, V. V.; Whittingham, M. S.; Xiao, J.; Xu, W.; Yang, J.; Yang, X.-Q.; Zhang, J.-G., Pathways for practical high-energy long-cycling lithium metal batteries. *Nat. Energy* **2019,** *4*, 180-186.

4. Albertus, P.; Babinec, S.; Litzelman, S.; Newman, A., Status and challenges in enabling the lithium metal electrode for high-energy and low-cost rechargeable batteries. *Nat. Energy* **2017,** *3*, 16-21.

5. Ding, Y.; Cano, Z. P.; Yu, A.; Lu, J.; Chen, Z., Automotive Li-Ion Batteries: Current Status and Future Perspectives. *Electrochem. Energy Rev.* **2019,** *2*, 1-28.

6. Bruce, P. G.; Freunberger, S. A.; Hardwick, L. J.; Tarascon, J.-M., Li–O2 and Li–S Batteries with High Energy Storage. *Nat. Mater.* **2011,** *11*, 19-29.

7. Li, G.; Chen, Z.; Lu, J., Lithium-Sulfur Batteries for Commercial Applications. *Chem* **2018,** *4*, 3-7.

8. Slater, M. D.; Kim, D.; Lee, E.; Johnson, C. S., Sodium-Ion Batteries. *Adv. Funct. Mater.* **2013,** *23*, 947-958.

9. Eftekhari, A.; Jian, Z.; Ji, X., Potassium Secondary Batteries. *ACS Appl. Mater. Interfaces* **2017,** *9,* 4404-4419.

10. Li, M.; Wang, C.; Chen, Z.; Xu, K.; Lu, J., New Concepts in Electrolytes. *Chem. Rev.* **2020**.

11. Li, M.; Lu, J.; Ji, X.; Li, Y.; Shao, Y.; Chen, Z.; Zhong, C.; Amine, K., Design Strategies for Nonaqueous Multivalent-Ion and Monovalent-Ion Battery Anodes. *Nat. Rev. Mater.* **2020,** *5,* 276-294.

12. Zhang, T.; Tao, Z.; Chen, J., Magnesium–Air Batteries: from Principle to Application. *Mater. Horiz.* **2014,** *1,* 196-206.

13. Lin, M. C.; Gong, M.; Lu, B.; Wu, Y.; Wang, D. Y.; Guan, M.; Angell, M.; Chen, C.; Yang, J.; Hwang, B. J.; Dai, H., An ultrafast rechargeable aluminium-ion battery. *Nature* **2015,** *520,* 325-8.

14. Li, Y.; Lu, J., Metal–air batteries: will they be the future electrochemical energy storage device of choice? *ACS Energy Lett.* **2017,** *2,* 1370-1377.

15. Mainar, A. R.; Colmenares, L. C.; Blázquez, J. A.; Urdampilleta, I., A brief overview of secondary zinc anode development: The key of improving zinc‐based energy storage systems. *Int J Energy Res.* **2017,** *42,* 1-16.

16. Ming, J.; Guo, J.; Xia, C.; Wang, W.; Alshareef, H. N., Zinc-Ion Batteries: Materials, Mechanisms, and Applications. *Mater. Sci. Eng. R: Rep.* **2019,** *135,* 58-84.

17. Li, Y.; Dai, H., Recent Advances in Zinc-Air Batteries. *Chem. Soc. Rev.* **2014,** *43,* 5257-75.

18. Song, M.; Tan, H.; Chao, D.; Fan, H. J., Recent Advances in Zn-Ion Batteries. *Adv. Funct. Mater.* **2018,** *28,* 1802564.

19. Wan, F.; Niu, Z., Design Strategies for Vanadium-based Aqueous Zinc-Ion Batteries. *Angew. Chem. Int. Ed.* **2019,** *58,* 16358-16367.

20. Ma, L.; Chen, S.; Long, C.; Li, X.; Zhao, Y.; Liu, Z.; Huang, Z.; Dong, B.; Zapien, J. A.; Zhi, C., Achieving High - Voltage and High - Capacity Aqueous Rechargeable Zinc Ion Battery by Incorporating Two - Species Redox Reaction. *Adv. Energy Mater.* **2019,** *9,* 1902446.

21. Yadav, G. G.; Gallaway, J. W.; Turney, D. E.; Nyce, M.; Huang, J.; Wei, X.; Banerjee, S., Regenerable Cu-Intercalated MnO2 Layered Cathode for Highly Cyclable Energy Dense Batteries. *Nat. Commun.* **2017,** *8,* 14424.

22. Alfaruqi, M. H.; Mathew, V.; Gim, J.; Kim, S.; Song, J.; Baboo, J. P.; Choi, S. H.; Kim, J., Electrochemically Induced Structural Transformation in a γ-MnO2 Cathode of a High Capacity Zinc-Ion Battery System. *Chem. Mater.* **2015,** *27,* 3609-3620.

23. Kozawa, A.; Powers, R. A., Electrochemical reactions in batteries. Emphasizing the MnO2 cathode of dry cells. *J. Chem. Educ.* **1972,** *49,* 587.

24. Selvakumaran, D.; Pan, A.; Liang, S.; Cao, G., A Review on Recent Developments and Challenges of Cathode Materials for Rechargeable Aqueous Zn-Ion Batteries. *J. Mater. Chem. A* **2019,** *7,* 18209-18236.

25. Hu, P.; Wang, T.; Zhao, J.; Zhang, C.; Ma, J.; Du, H.; Wang, X.; Cui, G., Ultrafast Alkaline Ni/Zn Battery Based on Ni-Foam-Supported Ni3S2 Nanosheets. *ACS Appl. Mater. Interfaces* **2015,** *7,* 26396-9.

26. Higashi, S.; Lee, S. W.; Lee, J. S.; Takechi, K.; Cui, Y., Avoiding Short Circuits from Zinc Metal Dendrites in Anode by Backside-Plating Configuration. *Nat. Commun.* **2016,** *7,* 11801.

27. McLarnon, F. R.; Cairns, E. J., The Secondary Alkaline Zinc Electrode. *J. Electrochem. Soc.* **1991,** *138,* 645-664.

28. Sun, W.; Wang, F.; Hou, S.; Yang, C.; Fan, X.; Ma, Z.; Gao, T.; Han, F.; Hu, R.; Zhu, M.; Wang, C., Zn/MnO2 Battery Chemistry With H(+) and Zn(2+) Coinsertion. *J. Am. Chem. Soc.* **2017,** *139,* 9775-9778.

29. Chao, D.; Zhou, W.; Ye, C.; Zhang, Q.; Chen, Y.; Gu, L.; Davey, K.; Qiao, S. Z., An Electrolytic Zn-MnO2 Battery for High-Voltage and Scalable Energy Storage. *Angew. Chem. Int. Ed.* **2019,** *58,* 7823-7828.

30. Yadav, G. G.; Turney, D.; Huang, J.; Wei, X.; Banerjee, S., Breaking the 2 V Barrier in Aqueous Zinc Chemistry: Creating 2.45 and 2.8 V MnO2–Zn Aqueous Batteries. *ACS Energy Lett.* **2019,** *4,* 2144-2146.

31. Zhong, C.; Liu, B.; Ding, J.; Liu, X.; Zhong, Y.; Li, Y.; Sun, C.; Han, X.; Deng, Y.; Zhao, N.; Hu, W., Decoupling Electrolytes towards Stable and High-Energy Rechargeable Aqueous Zinc–Manganese Dioxide Batteries. *Nat. Energy* **2020**.

32. Yuan, Z.; Yin, Y.; Xie, C.; Zhang, H.; Yao, Y.; Li, X., Advanced Materials for Zinc-Based Flow Battery: Development and Challenge. *Adv. Mater.* **2019,** *31,* e1902025.

33. Jorné, J.; Kim, J.; Kralik, D., The zinc-chlorine battery: half-cell overpotential measurements. *Journal of Applied Electrochemistry* **1979,** *9,* 573-579.

34. Wang, C.; Lai, Q.; Feng, K.; Xu, P.; Li, X.; Zhang, H., From zeolite-type metal organic framework to porous nano-sheet carbon: High activity positive electrode material for bromine-based flow batteries. *Nano Energy* **2018,** *44*, 240-247.

35. Xie, C.; Liu, Y.; Lu, W.; Zhang, H.; Li, X., Highly stable zinc–iodine single flow batteries with super high energy density for stationary energy storage. *Energy & Environmental Science* **2019,** *12*, 1834-1839.

36. Li, B.; Nie, Z.; Vijayakumar, M.; Li, G.; Liu, J.; Sprenkle, V.; Wang, W., Ambipolar Zinc-Polyiodide Electrolyte for a High-Energy Density Aqueous Redox Flow Battery. *Nat. Commun.* **2015,** *6*, 6303.

37. Zhang, J.; Jiang, G.; Xu, P.; Ghorbani Kashkooli, A.; Mousavi, M.; Yu, A.; Chen, Z., An All-Aqueous Redox Flow Battery with Unprecedented Energy Density. *Energy Environ. Sci.* **2018,** *11*, 2010-2015.

38. Gong, K.; Ma, X.; Conforti, K. M.; Kuttler, K. J.; Grunewald, J. B.; Yeager, K. L.; Bazant, M. Z.; Gu, S.; Yan, Y., A zinc–iron redox-flow battery under $100 per kW h of system capital cost. *Energy & Environmental Science* **2015,** *8*, 2941-2945.

39. Li, Y.; Geysens, P.; Zhang, X.; Sniekers, J.; Fransaer, J.; Binnemans, K.; Vankelecom, I. F., Cerium-containing complexes for low-cost, non-aqueous redox flow batteries (RFBs). *Journal of Power Sources* **2020,** *450*, 227634.

40. Leung, P.; Martin, T.; Shah, A.; Mohamed, M.; Anderson, M.; Palma, J., Membrane-less hybrid flow battery based on low-cost elements. *Journal of Power Sources* **2017,** *341*, 36-45.

41. Winsberg, J.; Stolze, C.; Schwenke, A.; Muench, S.; Hager, M. D.; Schubert, U. S., Aqueous 2, 2, 6, 6-tetramethylpiperidine-N-oxyl catholytes for a high-capacity

and high current density oxygen-insensitive hybrid-flow battery. *ACS Energy Letters* **2017,** *2,* 411-416.

42. Winsberg, J.; Janoschka, T.; Morgenstern, S.; Hagemann, T.; Muench, S.; Hauffman, G.; Gohy, J. F.; Hager, M. D.; Schubert, U. S., Poly (TEMPO)/Zinc Hybrid - Flow Battery: A Novel, "Green," High Voltage, and Safe Energy Storage System. *Advanced Materials* **2016,** *28,* 2238-2243.

43. Yuan, Z.; Yin, Y.; Xie, C.; Zhang, H.; Yao, Y.; Li, X., Advanced Materials for Zinc - Based Flow Battery: Development and Challenge. *Advanced Materials* **2019,** *31,* 1902025.

44. Khor, A.; Leung, P.; Mohamed, M.; Flox, C.; Xu, Q.; An, L.; Wills, R.; Morante, J.; Shah, A., Review of zinc-based hybrid flow batteries: From fundamentals to applications. *Materials today energy* **2018,** *8,* 80-108.

45. Weng, G.-M.; Li, Z.; Cong, G.; Zhou, Y.; Lu, Y.-C., Unlocking the Capacity of Iodide for High-Energy-Density Zinc/Polyiodide and Lithium/Polyiodide Redox Flow Batteries. *Energy Environ. Sci.* **2017,** *10,* 735-741.

46. Xie, C.; Zhang, H.; Xu, W.; Wang, W.; Li, X., A Long Cycle Life, Self - Healing Zinc–Iodine Flow Battery with High Power Density. *Angewandte Chemie International Edition* **2018,** *57,* 11171-11176.

47. Cao, R.; Lee, J.-S.; Liu, M.; Cho, J., Recent Progress in Non-Precious Catalysts for Metal-Air Batteries. *Adv. Energy Mater.* **2012,** *2,* 816-829.

48. Fu, J.; Cano, Z. P.; Park, M. G.; Yu, A.; Fowler, M.; Chen, Z., Electrically Rechargeable Zinc-Air Batteries: Progress, Challenges and Perspectives. *Adv. Mater.* **2017,** *29,* 1604685.

49. Deng, Y.-P.; Liang, R.; Jiang, G.; Jiang, Y.; Yu, A.; Chen, Z., The Current State of Aqueous Zn-Based Rechargeable Batteries. *ACS Energy Lett.* **2020,** *5,* 1665-1675.

50. Cheng, F.; Chen, J., Metal-Air Batteries: from Oxygen Reduction Electrochemistry to Cathode Catalysts. *Chem. Soc. Rev.* **2012,** *41,* 2172-2192.

51. Lee, J.-S.; Tai Kim, S.; Cao, R.; Choi, N.-S.; Liu, M.; Lee, K. T.; Cho, J., Metal-air batteries with high energy density: Li-air versus Zn-air. *Adv. Energy Mater.* **2011,** *1,* 34-50.

52. Hartmann, P.; Bender, C. L.; Vracar, M.; Durr, A. K.; Garsuch, A.; Janek, J.; Adelhelm, P., A rechargeable room-temperature sodium superoxide (NaO2) battery. *Nature materials* **2013,** *12,* 228-32.

53. Xiao, N.; Ren, X.; McCulloch, W. D.; Gourdin, G.; Wu, Y., Potassium Superoxide: A Unique Alternative for Metal-Air Batteries. *Acc Chem Res* **2018,** *51,* 2335-2343.

54. Grande, L.; Paillard, E.; Hassoun, J.; Park, J. B.; Lee, Y. J.; Sun, Y. K.; Passerini, S.; Scrosati, B., The lithium/air battery: still an emerging system or a practical reality? *Adv Mater* **2015,** *27,* 784-800.

55. Abraham, K. M.; Jiang, Z., A Polymer Electrolyte-Based Rechargeable lithium/Oxygen Battery. *J. Electrochem. Soc.* **1996,** *143,* 1-5.

56. Kundu, D.; Black, R.; Adams, B.; Nazar, L. F., A Highly Active Low Voltage Redox Mediator for Enhanced Rechargeability of Lithium–Oxygen Batteries. *ACS Central Science* **2015,** *1,* 510-515.

57. Kundu, D.; Black, R.; Adams, B.; Harrison, K.; Zavadil, K.; Nazar, L. F., Nanostructured Metal Carbides for Aprotic Li-O2 Batteries: New Insights into Interfacial Reactions and Cathode Stability. *J Phys Chem Lett* **2015,** *6,* 2252-8.

58. Black, R.; Adams, B.; Nazar, L. F., Non-Aqueous and Hybrid Li-O2 Batteries. *Advanced Energy Materials* **2012,** *2,* 801-815.

59. Black, R.; Oh, S. H.; Lee, J. H.; Yim, T.; Adams, B.; Nazar, L. F., Screening for superoxide reactivity in Li-O2 batteries: effect on Li2O2/LiOH crystallization. *Journal of the American Chemical Society* **2012,** *134,* 2902-5.

60. Ganapathy, S.; Adams, B. D.; Stenou, G.; Anastasaki, M. S.; Goubitz, K.; Miao, X. F.; Nazar, L. F.; Wagemaker, M., Nature of Li2O2 oxidation in a Li-O2 battery revealed by operando X-ray diffraction. *Journal of the American Chemical Society* **2014,** *136,* 16335-44.

61. Oh, S. H.; Black, R.; Pomerantseva, E.; Lee, J. H.; Nazar, L. F., Synthesis of a metallic mesoporous pyrochlore as a catalyst for lithium-O2 batteries. *Nature chemistry* **2012,** *4,* 1004-10.

62. Lu, J.; Li, L.; Park, J. B.; Sun, Y. K.; Wu, F.; Amine, K., Aprotic and Aqueous Li-O2 Batteries. *Chem. Rev.* **2014,** *114,* 5611-5640.

63. Tan, P.; Chen, B.; Xu, H.; Zhang, H.; Cai, W.; Ni, M.; Liu, M.; Shao, Z., Flexible Zn- and Li-Air Batteries: Recent Advances, Challenges, and Future Perspectives. *Energy Environ. Sci.* **2017,** *10,* 2056-2080.

64. Pan, J.; Xu, Y. Y.; Yang, H.; Dong, Z.; Liu, H.; Xia, B. Y., Advanced Architectures and Relatives of Air Electrodes in Zn-Air Batteries. *Advanced Science* **2018,** 1700691.

65. Zhang, X.; Wang, X.-G.; Xie, Z.; Zhou, Z., Recent progress in rechargeable alkali metal–air batteries. *Green Energy & Environment* **2016,** *1*, 4-17.

66. Xu, M.; Ivey, D. G.; Xie, Z.; Qu, W., Rechargeable Zn-air batteries: Progress in electrolyte development and cell configuration advancement. *Journal of Power Sources* **2015,** *283*, 358-371.

67. Wang, Y.; Fu, J.; Zhang, Y.; Li, M.; Hassan, F. M.; Li, G.; Chen, Z., Continuous fabrication of a MnS/Co nanofibrous air electrode for wide integration of rechargeable zinc-air batteries. *Nanoscale* **2017,** *9*, 15865-15872.

68. Zhao, Z.; Fan, X.; Ding, J.; Hu, W.; Zhong, C.; Lu, J., Challenges in Zinc Electrodes for Alkaline Zinc–Air Batteries: Obstacles to Commercialization. *ACS Energy Lett.* **2019,** *4*, 2259-2270.

69. Lee, S.-M.; Kim, Y.-J.; Eom, S.-W.; Choi, N.-S.; Kim, K.-W.; Cho, S.-B., Improvement in Self-Discharge of Zn Anode by Applying Surface Modification for Zn–Air Batteries with High Energy Density. *J. Power Sources* **2013,** *227*, 177-184.

70. Jo, Y. N.; Prasanna, K.; Kang, S. H.; Ilango, P. R.; Kim, H. S.; Eom, S. W.; Lee, C. W., The Effects of Mechanical Alloying on the Self-Discharge and Corrosion Behavior in Zn-Air Batteries. *J. Ind. Eng. Chem.* **2017,** *53*, 247-252.

71. Liang, M.; Zhou, H.; Huang, Q.; Hu, S.; Li, W., Synergistic Effect of Polyethylene Glycol 600 and Polysorbate 20 on Corrosion Inhibition of Zinc Anode in Alkaline Batteries. *J Appl. Electrochem.* **2011,** *41*, 991-997.

72. Wang, Z.; Huang, J.; Guo, Z.; Dong, X.; Liu, Y.; Wang, Y.; Xia, Y., A Metal-Organic Framework Host for Highly Reversible Dendrite-free Zinc Metal Anodes. *Joule* **2019,** *3*, 1289-1300.

73. Zheng, J.; Zhao, Q.; Tang, T.; Yin, J.; Quilty, C. D.; Renderos, G. D.; Liu, X.; Deng, Y.; Wang, L.; Bock, D. C.; Jaye, C.; Zhang, D.; Takeuchi, E. S.; Takeuchi, K. J.; Marschilok, A. C.; Archer, L. A., Reversible Epitaxial Electrodeposition of Metals in Battery Anodes. *Science* **2019,** *366,* 645-648.

74. Suo, L.; Borodin, O.; Gao, T.; Olguin, M.; Ho, J.; Fan, X.; Luo, C.; Wang, C.; Xu, K., "Water-in-salt" Electrolyte Enables High-Voltage Aqueous Lithium-Ion Chemistries. *Science* **2015,** *350,* 938-943.

75. Wang, F.; Borodin, O.; Gao, T.; Fan, X.; Sun, W.; Han, F.; Faraone, A.; Dura, J. A.; Xu, K.; Wang, C., Highly Reversible Zinc Metal Anode for Aqueous Batteries. *Nat. Mater.* **2018,** *17,* 543-549.

76. Wei, C.; Feng, Z.; Scherer, G. G.; Barber, J.; Shao-Horn, Y.; Xu, Z. J., Cations in Octahedral Sites: A Descriptor for Oxygen Electrocatalysis on Transition-Metal Spinels. *Adv. Mater.* **2017,** *29,* 1606800.

77. Guo, S.; Zhang, S.; Sun, S., Tuning nanoparticle catalysis for the oxygen reduction reaction. *Angewandte Chemie* **2013,** *52,* 8526-44.

78. Dai, L.; Xue, Y.; Qu, L.; Choi, H. J.; Baek, J. B., Metal-free catalysts for oxygen reduction reaction. *Chem Rev* **2015,** *115,* 4823-92.

79. Tang, C.; Wang, H. F.; Zhang, Q., Multiscale Principles to Boost Reactivity in Gas-Involving Energy Electrocatalysis. *Acc. Chem. Res.* **2018,** *51,* 881-889.

80. Reier, T.; Nong, H. N.; Teschner, D.; Schlögl, R.; Strasser, P., Electrocatalytic Oxygen Evolution Reaction in Acidic Environments - Reaction Mechanisms and Catalysts. *Advanced Energy Materials* **2017,** *7,* 1601275.

81. Suen, N. T.; Hung, S. F.; Quan, Q.; Zhang, N.; Xu, Y. J.; Chen, H. M., Electrocatalysis for the oxygen evolution reaction: recent development and future perspectives. *Chemical Society reviews* **2017,** *46*, 337-365.

82. Co3O4 and Co- Based Spinel Oxides Bifunctional Oxygen Electrodes. *Int. J. Electrochem. Sci.* **2010,** 556-577.

83. Gong, M.; Dai, H., A mini review of NiFe-based materials as highly active oxygen evolution reaction electrocatalysts. *Nano Research* **2014,** *8*, 23-39.

84. Jiang, Y.; Deng, Y. P.; Liang, R.; Fu, J.; Luo, D.; Liu, G.; Li, J.; Zhang, Z.; Hu, Y.; Chen, Z., Multidimensional Ordered Bifunctional Air Electrode Enables Flash Reactants Shuttling for High-Energy Flexible Zn-Air Batteries. *Adv. Energy Mater.* **2019,** *9*, 1900911.

85. Fu, G.; Cui, Z.; Chen, Y.; Li, Y.; Tang, Y.; Goodenough, J. B., Ni3Fe-N Doped Carbon Sheets as a Bifunctional Electrocatalyst for Air Cathodes. *Adv. Energy Mater.* **2016,** 1601172.

86. Fu, J.; Liang, R.; Liu, G.; Yu, A.; Bai, Z.; Yang, L.; Chen, Z., Recent Progress in Electrically Rechargeable Zinc-Air Batteries. *Adv. Mater.* **2018,** *31*, 1805230.

87. Liu, X.; Dai, L., Carbon-Based Metal-Free Catalysts. *Nat. Rev. Mater.* **2016,** *1*, 16064.

88. Lei, W.; Deng, Y.-P.; Li, G.; Cano, Z. P.; Wang, X.; Luo, D.; Liu, Y.; Wang, D.; Chen, Z., Two-Dimensional Phosphorus-Doped Carbon Nanosheets with Tunable Porosity for Oxygen Reactions in Zinc-Air Batteries. *ACS Catal.* **2018,** *8*, 2464-2472.

89. Pei, Z.; Li, H.; Huang, Y.; Xue, Q.; Huang, Y.; Zhu, M.; Wang, Z.; Zhi, C., Texturing in situ: N,S-Enriched Hierarchically Porous Carbon as a Highly Active Reversible Oxygen Electrocatalyst. *Energy Environ. Sci.* **2017,** *10*, 742-749.

90. Zhang, J.; Zhao, Z.; Xia, Z.; Dai, L., A Metal-Free Bifunctional Electrocatalyst for Oxygen Reduction and Oxygen Evolution Reactions. *Nat. Nanotechnol.* **2015,** *10*, 444-452.

91. Yang, H. B.; Miao, J.; Hung, S.-F.; Chen, J.; Tao, H. B.; Wang, X.; Zhang, L.; Chen, R.; Gao, J.; Chen, H. M.; Dai, L.; Liu, B., Identification of catalytic sites for oxygen reduction and oxygen evolution in N-doped graphene bifunctional electrocatalysts. *Sci. Adv.* **2016,** *2*, e1501122.

92. Chen, J.; Siegel, J. B.; Matsuura, T.; Stefanopoulou, A. G., Carbon Corrosion in PEM Fuel Cell Dead-Ended Anode Operations. *J. Electrochem. Soc.* **2011,** *158*, B1164-B1174.

93. Park, M. G.; Lee, D. U.; Seo, M. H.; Cano, Z. P.; Chen, Z., 3D Ordered Mesoporous Bifunctional Oxygen Catalyst for Electrically Rechargeable Zinc-Air Batteries. *Small* **2016,** *12*, 2707-14.

94. Lee, D. U.; Choi, J.-Y.; Feng, K.; Park, H. W.; Chen, Z., Advanced Extremely Durable 3D Bifunctional Air Electrodes for Rechargeable Zinc-Air Batteries. *Adv. Energy Mater.* **2014,** *4*, 1301389.

95. Wang, X. T.; Ouyang, T.; Wang, L.; Zhong, J. H.; Ma, T.; Liu, Z. Q., Redox-Inert Fe(3+) Ions in Octahedral Sites of Co-Fe Spinel Oxides with Enhanced Oxygen Catalytic Activity for Rechargeable Zinc-Air Batteries. *Angew. Chem. Int. Ed. Engl.* **2019,** *58*, 13291-13296.

96. Suntivich, J.; Gasteiger, H. A.; Yabuuchi, N.; Nakanishi, H.; Goodenough, J. B.; Shao-Horn, Y., Design principles for oxygen-reduction activity on perovskite oxide catalysts for fuel cells and metal-air batteries. *Nat Chem* **2011,** *3,* 546-50.

97. Bu, Y.; Gwon, O.; Nam, G.; Jang, H.; Kim, S.; Zhong, Q.; Cho, J.; Kim, G., A Highly Efficient and Robust Cation Ordered Perovskite Oxide as a Bifunctional Catalyst for Rechargeable Zinc-Air Batteries. *ACS Nano* **2017,** *11,* 11594-11601.

98. Zhong, X.; Jiang, Y.; Chen, X.; Wang, L.; Zhuang, G.; Li, X.; Wang, J.-g., Integrating cobalt phosphide and cobalt nitride-embedded nitrogen-rich nanocarbons: high-performance bifunctional electrocatalysts for oxygen reduction and evolution. *J. Mater. Chem. A* **2016,** *4,* 10575-10584.

99. Lin, C.; Li, X.; Shinde, S. S.; Kim, D.-H.; Song, X.; Zhang, H.; Lee, J.-H., Long-Life Rechargeable Zn Air Battery Based on Binary Metal Carbide Armored by Nitrogen-Doped Carbon. *ACS Applied Energy Materials* **2019,** *2,* 1747-1755.

100. Zhang, J.; Bai, X.; Wang, T.; Xiao, W.; Xi, P.; Wang, J.; Gao, D.; Wang, J., Bimetallic Nickel Cobalt Sulfide as Efficient Electrocatalyst for Zn-Air Battery and Water Splitting. *Nanomicro Lett* **2019,** *11,* 2.

101. Niu, W.; Li, Z.; Marcus, K.; Zhou, L.; Li, Y.; Ye, R.; Liang, K.; Yang, Y., Surface-Modified Porous Carbon Nitride Composites as Highly Efficient Electrocatalyst for Zn-Air Batteries. *Adv. Energy Mater.* **2018,** *8.*

102. Li, G.; Wang, X.; Fu, J.; Li, J.; Park, M. G.; Zhang, Y.; Lui, G.; Chen, Z., Pomegranate-Inspired Design of Highly Active and Durable Bifunctional Electrocatalysts for Rechargeable Metal-Air Batteries. *Angew. Chem. Int. Ed.* **2016,** *55,* 4977-4982.

103. Lee, D. U.; Xu, P.; Cano, Z. P.; Kashkooli, A. G.; Park, M. G.; Chen, Z., Recent Progress and Perspectives on Bifunctional Oxygen Electrocatalysts for Advanced Rechargeable Metal–Air Batteries. *J. Mater. Chem. A* **2016,** *4*, 7107-7134.

104. Xing, Z.; Deng, Y.-P.; Sy, S.; Tan, G.; Li, A.; Li, J.; Niu, Y.; Li, N.; Su, D.; Lu, J.; Chen, Z., Carbon-Pore-Sheathed Cobalt Nanoseeds: An Exceptional and Durable Bifunctional Catalyst for Zinc-Air Batteries. *Nano Energy* **2019,** *65*, 104051.

105. Zhang, Z.; Deng, Y. P.; Xing, Z.; Luo, D.; Sy, S.; Cano, Z. P.; Liu, G.; Jiang, Y.; Chen, Z., "Ship in a Bottle" Design of Highly Efficient Bifunctional Electrocatalysts for Long-Lasting Rechargeable Zn-Air Batteries. *ACS Nano* **2019,** *13*, 7062-7072.

106. Liu, X.; Park, M.; Kim, M. G.; Gupta, S.; Wu, G.; Cho, J., Integrating NiCo Alloys with Their Oxides as Efficient Bifunctional Cathode Catalysts for Rechargeable Zinc-Air Batteries. *Angew. Chem. Int. Ed.* **2015,** *54*, 9654-9658.

107. Ma, H.; Wang, B., A bifunctional electrocatalyst α-MnO2-LaNiO3/carbon nanotube composite for rechargeable zinc–air batteries. *RSC Adv.* **2014,** *4*, 46084-46092.

108. Ren, D.; Ying, J.; Xiao, M.; Deng, Y. P.; Ou, J.; Zhu, J.; Liu, G.; Pei, Y.; Li, S.; Jauhar, A. M.; Jin, H.; Wang, S.; Su, D.; Yu, A.; Chen, Z., Hierarchically Porous Multimetal‐Based Carbon Nanorod Hybrid as an Efficient Oxygen Catalyst for Rechargeable Zinc–Air Batteries. *Adv. Funct. Mater.* **2019,** *30*.

109. Xing, Z.; Deng, Y.-P.; Sy, S.; Tan, G.; Li, A.; Li, J.; Niu, Y.; Li, N.; Su, D.; Lu, J.; Chen, Z., Carbon-pore-sheathed cobalt nanoseeds: An exceptional and durable bifunctional catalyst for zinc-air batteries. *Nano Energy* **2019,** *65*.

110. Shu, X.; Chen, S.; Chen, S.; Pan, W.; Zhang, J., Cobalt nitride embedded holey N-doped graphene as advanced bifunctional electrocatalysts for Zn-Air batteries and overall water splitting. *Carbon* **2020,** *157,* 234-243.

111. Li, Y.; Gong, M.; Liang, Y.; Feng, J.; Kim, J. E.; Wang, H.; Hong, G.; Zhang, B.; Dai, H., Advanced zinc-air batteries based on high-performance hybrid electrocatalysts. *Nature communications* **2013,** *4,* 1805.

112. Wang, Y.-C.; Huang, L.; Zhang, P.; Qiu, Y.-T.; Sheng, T.; Zhou, Z.-Y.; Wang, G.; Liu, J.-G.; Rauf, M.; Gu, Z.-Q.; Wu, W.-T.; Sun, S.-G., Constructing a Triple-Phase Interface in Micropores to Boost Performance of Fe/N/C Catalysts for Direct Methanol Fuel Cells. *ACS Energy Lett.* **2017,** *2,* 645-650.

113. Xu, K.; Chen, P.; Li, X.; Tong, Y.; Ding, H.; Wu, X.; Chu, W.; Peng, Z.; Wu, C.; Xie, Y., Metallic Nickel Nitride Nanosheets Realizing Enhanced Electrochemical Water Oxidation. *J. Am. Chem. Soc.* **2015,** *137,* 4119-4125.

114. Seh, Z. W.; Kibsgaard, J.; Dickens, C. F.; Chorkendorff, I.; Norskov, J. K.; Jaramillo, T. F., Combining Theory and Experiment in Electrocatalysis: Insights into Materials Design. *Science* **2017,** *355,* eaad4998

115. Liang, H. W.; Zhuang, X.; Bruller, S.; Feng, X.; Mullen, K., Hierarchically Porous Carbons with Optimized Nitrogen Doping as Highly Active Electrocatalysts for Oxygen Reduction. *Nat. Commun.* **2014,** *5,* 4973.

116. Fu, J.; Hassan, F. M.; Zhong, C.; Lu, J.; Liu, H.; Yu, A.; Chen, Z., Defect Engineering of Chalcogen-Tailored Oxygen Electrocatalysts for Rechargeable Quasi-Solid-State Zinc-Air Batteries. *Adv. Mater.* **2017,** *29,* 1702526.

117. Deng, Y.-P.; Jiang, Y.; Luo, D.; Fu, J.; Liang, R.; Cheng, S.; Bai, Z.; Liu, Y.; Lei, W.; Yang, L.; Zhu, J.; Chen, Z., Hierarchical Porous Double-Shelled Electrocatalyst with Tailored Lattice Alkalinity towards Bifunctional Oxygen Reactions for Metal-Air Battery. *ACS Energy Lett.* **2017,** *2,* 2706-2712.

118. Fu, X.; Zamani, P.; Choi, J. Y.; Hassan, F. M.; Jiang, G.; Higgins, D. C.; Zhang, Y.; Hoque, M. A.; Chen, Z., In Situ Polymer Graphenization Ingrained with Nanoporosity in a Nitrogenous Electrocatalyst Boosting the Performance of Polymer-Electrolyte-Membrane Fuel Cells. *Adv. Mater.* **2017,** *29,* 1604456.

119. Seo, M. H.; Park, M. G.; Lee, D. U.; Wang, X.; Ahn, W.; Noh, S. H.; Choi, S. M.; Cano, Z. P.; Han, B.; Chen, Z., Bifunctionally Active and Durable Hierarchically Porous Transition Metal-Based Hybrid Electrocatalyst for Rechargeable Metal-Air Batteries. *Appl. Catal. B: Environ.* **2018,** *239,* 677-687.

120. Chen, Z.; Yu, A.; Higgins, D.; Li, H.; Wang, H.; Chen, Z., Highly active and durable core-corona structured bifunctional catalyst for rechargeable metal-air battery application. *Nano Lett.* **2012,** *12,* 1946-52.

121. Fu, J.; Hassan, F. M.; Li, J.; Lee, D. U.; Ghannoum, A. R.; Lui, G.; Hoque, M. A.; Chen, Z., Flexible Rechargeable Zinc-Air Batteries through Morphological Emulation of Human Hair Array. *Adv. Mater.* **2016,** *28,* 6421-6428.

122. Zhang, G.; Xia, B. Y.; Wang, X.; David Lou, X. W., Strongly coupled NiCo(2)O(4)-rGO hybrid nanosheets as a methanol-tolerant electrocatalyst for the oxygen reduction reaction. *Adv Mater* **2014,** *26,* 2408-12.

123. Jiang, Y.; Deng, Y.-P.; Fu, J.; Lee, D. U.; Liang, R.; Cano, Z. P.; Liu, Y.; Bai, Z.; Hwang, S.; Yang, L.; Su, D.; Chu, W.; Chen, Z., Interpenetrating Triphase

Cobalt-Based Nanocomposites as Efficient Bifunctional Oxygen Electrocatalysts for Long-Lasting Rechargeable Zn-Air Batteries. *Adv. Energy Mater.* **2018,** *8,* 1702900.

124. Ren, D.; Ying, J.; Xiao, M.; Deng, Y. P.; Ou, J.; Zhu, J.; Liu, G.; Pei, Y.; Li, S.; Jauhar, A. M.; Jin, H.; Wang, S.; Su, D.; Yu, A.; Chen, Z., Hierarchically Porous Multimetal‐Based Carbon Nanorod Hybrid as an Efficient Oxygen Catalyst for Rechargeable Zinc–Air Batteries. *Adv. Funct. Mater.* **2019,** *30,* 1908167.

125. Lee, D. U.; Li, J.; Park, M. G.; Seo, M. H.; Ahn, W.; Stadelmann, I.; Ricardez-Sandoval, L.; Chen, Z., Self-assembly of Spinel Nano-crystals into Mesoporous Spheres as Bi-functionally Active Oxygen Reduction and Evolution Electrocatalysts. *ChemSusChem* **2017,** *10,* 2258-2266.

126. Oversteeg, C. H. M. v.; Doan, H. Q.; Groot, F. M. F. d.; Cuk, T., In situ X-ray absorption spectroscopy of transition metal based water oxidation catalysts. *Chem. Soc. Rev.* **2017,** *46,* 102-125.

127. Henderson, G. S.; de Groot, F. M. F.; Moulton, B. J. A., X-ray Absorption Near-Edge Structure (XANES) Spectroscopy. *Reviews in Mineralogy and Geochemistry* **2014,** *78,* 75-138.

128. Ice, G. E.; Budai, J. D.; Pang, J. W. L., The Race to X-ray Microbeam and Nanobeam Science. *Science* **2011,** *334,* 1234-1239.

129. Kanan, M. W.; Yano, J.; Surendranath, Y.; Dinca, M.; Yachandra, V. K.; Nocera, D. G., Structure and Valency of a Cobalt-Phosphate Water Oxidation Catalyst Determined by in Situ X-ray Spectroscopy. *J. Am. Chem. Soc.* **2010,** *132,* 13692-13701.

130. Inkson, B. J., Scanning electron microscopy (SEM) and transmission electron microscopy (TEM) for materials characterization. In *Materials Characterization Using Nondestructive Evaluation (NDE) Methods*, 2016; pp 17-43.

131. Liang, Y.; Li, Y.; Wang, H.; Zhou, J.; Wang, J.; Regier, T.; Dai, H., Co3O4 nanocrystals on graphene as a synergistic catalyst for oxygen reduction reaction. *Nat. Mater.* **2011,** *10*, 780-786.

132. Rosen, J.; Hutchings, G. S.; Jiao, F., Ordered Mesoporous Cobalt Oxide as Highly Efficient Oxygen Evolution Catalyst. *J. Am. Chem. Soc.* **2013,** *135*, 4516-4521.

133. Tong, X.; Xia, X.; Guo, C.; Zhang, Y.; Tu, J.; Fan, H. J.; Guo, X.-Y., Efficient oxygen reduction reaction using mesoporous Ni-doped Co3O4 nanowire array electrocatalysts. *J. Mater. Chem. A* **2015,** *3*, 18372-18379.

134. Higgins, D.; Zamani, P.; Yu, A.; Chen, Z., The Application of Graphene and Its Composites in Oxygen Reduction Electrocatalysis: A Perspective and Review of Recent Progress. *Energy Environ. Sci.* **2016,** *9*, 357-390.

135. Xia, B. Y.; Yan, Y.; Li, N.; Wu, H. B.; Lou, X. W.; Wang, X., A Metal-Organic Framework-Derived Bifunctional Oxygen Electrocatalyst. *Nat. Energy* **2016,** *1*, 15006.

136. Lee, J.-S.; Nam, G.; Sun, J.; Higashi, S.; Lee, H.-W.; Lee, S.; Chen, W.; Cui, Y.; Cho, J., Composites of a Prussian Blue Analogue and Gelatin-Derived Nitrogen-Doped Carbon-Supported Porous Spinel Oxides as Electrocatalysts for a Zn-Air Battery. *Adv. Energy Mater.* **2016,** *6*, 1601052.

137. Lee, D. U.; Kim, B. J.; Chen, Z., One-pot Synthesis of A Mesoporous NiCo2O4 Nanoplatelet and Graphene Hybrid and Its Oxygen Reduction and Evolution Activities as An Efficient Bi-functional Electrocatalyst. *J. Mater. Chem. A* **2013,** *1,* 4754-4762.

138. Wang, J.; Tang, H.; Zhang, L.; Ren, H.; Yu, R.; Jin, Q.; Qi, J.; Mao, D.; Yang, M.; Wang, Y.; Liu, P.; Zhang, Y.; Wen, Y.; Gu, L.; Ma, G.; Su, Z.; Tang, Z.; Zhao, H.; Wang, D., Multi-Shelled Metal Oxides Prepared via An Anion-Adsorption Mechanism for Lithium-Ion Batteries. *Nat. Energy* **2016,** *1,* 16050.

139. Qi, J.; Lai, X.; Wang, J.; Tang, H.; Ren, H.; Yang, Y.; Jin, Q.; Zhang, L.; Yu, R.; Ma, G.; Su, Z.; Zhao, H.; Wang, D., Multi-Shelled Hollow Micro-/Nanostructures. *Chem. Soc. Rev.* **2015,** *44,* 6749-6773.

140. Zhou, L.; Zhuang, Z.; Zhao, H.; Lin, M.; Zhao, D.; Mai, L., Intricate Hollow Structures: Controlled Synthesis and Applications in Energy Storage and Conversion. *Adv. Mater.* **2017,** *29,* 1602914.

141. Zhang, G.; Lou, X. W., General Synthesis of Multi-Shelled Mixed Metal Oxide Hollow Spheres with Superior Lithium Storage Properties. *Angew. Chem. Int. Ed.* **2014,** *53,* 9041-9044.

142. Guan, B. Y.; Kushima, A.; Yu, L.; Li, S.; Li, J.; Lou, X. W., Coordination Polymers Derived General Synthesis of Multishelled Mixed Metal-Oxide Particles for Hybrid Supercapacitors. *Adv. Mater.* **2017,** *29,* 1605902.

143. Sun, X.; Li, Y., Colloidal Carbon Spheres and Their Core/Shell Structures with Noble-Metal Nanoparticles. *Angew. Chem. Int. Ed.* **2004,** *43,* 597-601.

144. Liu, X.; Chang, Z.; Luo, L.; Xu, T.; Lei, X.; Liu, J.; Sun, X., Hierarchical ZnxCo3–xO4 Nanoarrays with High Activity for Electrocatalytic Oxygen Evolution. *Chem. Mater.* **2014,** *26,* 1889-1895.

145. Li, C.; Han, X.; Cheng, F.; Hu, Y.; Chen, C.; Chen, J., Phase and Composition Controllable Synthesis of Cobalt Manganese Spinel Nanoparticles towards Efficient Oxygen Electrocatalysis. *Nat. Commun.* **2015,** *6,* 7345.

146. Kamioka, N.; Ichitsubo, T.; Uda, T.; Imashuku, S.; Taninouchi, Y.-k.; Matsubara, E., Synthesis of spinel-type magnesium cobalt oxide and its electrical conductivity. *Mater. Trans.* **2008,** *49,* 824-828.

147. Liu, Y.; Chen, F.; Ye, W.; Zeng, M.; Han, N.; Zhao, F.; Wang, X.; Li, Y., High-Performance Oxygen Reduction Electrocatalyst Derived from Polydopamine and Cobalt Supported on Carbon Nanotubes for Metal-Air Batteries. *Adv. Funct. Mater.* **2017,** *27,* 1606034.

148. Nam, G.; Park, J.; Choi, M.; Oh, P.; Park, S.; Kim, M. G.; Park, N.; Cho, J.; Lee, J.-S., Carbon-coated core-shell Fe-Cu nanoparticles as highly active and durable electrocatalysts for a Zn-air battery. *ACS Nano* **2015,** *9,* 6493–6501.

149. Deng, Y.-P.; Fu, F.; Wu, Z.-G.; Yin, Z.-W.; Zhang, T.; Li, J.-T.; Huang, L.; Sun, S.-G., Layered/spinel heterostructured Li-rich materials synthesized by one-step solvothermal strategy with enhanced electrochemical performance for Li-ion batteries. *J. Mater. Chem. A* **2016,** *4,* 257-263.

150. Wang, Q.; Shang, L.; Shi, R.; Zhang, X.; Zhao, Y.; Waterhouse, G. I. N.; Wu, L.-Z.; Tung, C.-H.; Zhang, T., NiFe layered double hydroxide nanoparticles on Co,N-codoped carbon nanoframes as efficient bifunctional catalysts for rechargeable zinc-air batteries. *Adv. Energy Mater.* **2017,** *7,* 1700467.

151. Tang, C.; Wang, B.; Wang, H. F.; Zhang, Q., Defect Engineering toward Atomic Co-Nx -C in Hierarchical Graphene for Rechargeable Flexible Solid Zn-Air Batteries. *Adv. Mater.* **2017,** *29,* 1703185.

152. Fu, G.; Cui, Z.; Chen, Y.; Xu, L.; Tang, Y.; Goodenough, J. B., Hierarchically mesoporous nickel-iron nitride as a cost-efficient and highly durable electrocatalyst for Zn-air battery. *Nano Energy* **2017,** *39,* 77-85.

153. Liu, G.; Li, J.; Fu, J.; Jiang, G.; Lui, G.; Luo, D.; Deng, Y. P.; Zhang, J.; Cano, Z. P.; Yu, A.; Su, D.; Bai, Z.; Yang, L.; Chen, Z., An Oxygen-Vacancy-Rich Semiconductor-Supported Bifunctional Catalyst for Efficient and Stable Zinc-Air Batteries. *Adv. Mater.* **2019,** *31,* 1806761.

154. Nam, G.; Son, Y.; Park, S. O.; Jeon, W. C.; Jang, H.; Park, J.; Chae, S.; Yoo, Y.; Ryu, J.; Kim, M. G.; Kwak, S. K.; Cho, J., A Ternary Ni46Co40Fe14 Nanoalloy-Based Oxygen Electrocatalyst for Highly Efficient Rechargeable Zinc–Air Batteries. *Adv. Mater.* **2018,** *30,* 1803372.

155. Zhu, C.; Yin, Z.; Lai, W.; Sun, Y.; Liu, L.; Zhang, X.; Chen, Y.; Chou, S.-L., Fe-Ni-Mo nitride porous nanotubes for full water splitting and Zn-air batteries. *Adv. Energy Mater.* **2018,** *8,* 1802327.

156. Li, H.; Li, Q.; Wen, P.; Williams, T. B.; Adhikari, S.; Dun, C.; Lu, C.; Itanze, D.; Jiang, L.; Carroll, D. L.; Donati, G. L.; Lundin, P. M.; Qiu, Y.; Geyer, S. M., Colloidal cobalt phosphide nanocrystals as trifunctional electrocatalysts for overall water splitting powered by a zinc-air battery. *Adv. Mater.* **2018,** *30,* 1705796.

157. Chen, P.; Xu, K.; Fang, Z.; Tong, Y.; Wu, J.; Lu, X.; Peng, X.; Ding, H.; Wu, C.; Xie, Y., Metallic Co4N porous nanowire arrays activated by surface oxidation

as electrocatalysts for the oxygen evolution reaction. *Angew. Chem. Int. Ed.* **2015,** *54*, 14710-14714.

158. Jin, S., Are Metal Chalcogenides, Nitrides, and Phosphides Oxygen Evolution Catalysts or Bifunctional Catalysts? *ACS Energy Lett.* **2017,** *2*, 1937-1938.

159. Stern, L.-A.; Feng, L.; Song, F.; Hu, X., Ni2P as a Janus catalyst for water splitting: the oxygen evolution activity of Ni2P nanoparticles. *Energy Environ. Sci.* **2015,** *8*, 2347-2351.

160. Xu, X.; Song, F.; Hu, X., A nickel iron diselenide-derived efficient oxygen-evolution catalyst. *Nat. Commun.* **2016,** *7*, 12324.

161. Li, J.; Liu, G.; Fu, J.; Jiang, G.; Luo, D.; Hassan, F. M.; Zhang, J.; Deng, Y.-P.; Xu, P.; Ricardez-Sandoval, L.; Chen, Z., Surface decorated cobalt sulfide as efficient catalyst for oxygen evolution reaction and its intrinsic activity. *J. Catal.* **2018,** *367*, 43-52.

162. Fabbri, E.; Nachtegaal, M.; Binninger, T.; Cheng, X.; Kim, B. J.; Durst, J.; Bozza, F.; Graule, T.; Schaublin, R.; Wiles, L.; Pertoso, M.; Danilovic, N.; Ayers, K. E.; Schmidt, T. J., Dynamic Surface Self-Reconstruction is the key of Highly Active Perovskite Nano-Electrocatalysts for Water Splitting. *Nat. Mater.* **2017,** *16*, 925-931.

163. Wu, T.; Sun, S.; Song, J.; Xi, S.; Du, Y.; Chen, B.; Sasangka, W. A.; Liao, H.; Gan, C. L.; Scherer, G. G.; Zeng, L.; Wang, H.; Li, H.; Grimaud, A.; Xu, Z. J., Iron-Facilitated Dynamic Active-Site Generation on Spinel CoAl2O4 with Self-Termination of Surface Reconstruction for Water Oxidation. *Nat. Catal.* **2019,** *2*, 763-772.

164. Yang, Y.; Wang, Y.; Xiong, Y.; Huang, X.; Shen, L.; Huang, R.; Wang, H.; Pastore, J. P.; Yu, S. H.; Xiao, L.; Brock, J. D.; Zhuang, L.; Abruna, H. D., In situ X-ray absorption spectroscopy of a synergistic Co-Mn oxide catalyst for the oxygen reduction reaction. *J. Am. Chem. Soc.* **2019,** *141,* 1463-1466.

165. Yuan, Y.; Wang, J.; Adimi, S.; Shen, H.; Thomas, T.; Ma, R.; Attfield, J. P.; Yang, M., Zirconium Nitride Catalysts Surpass Platinum for Oxygen Reduction. *Nat. Mater.* **2020,** *19,* 282-286.

166. Yu, L.; Yang, J. F.; Guan, B. Y.; Lu, Y.; Lou, X. W. D., Hierarchical hollow nanoprisms organized by ultrathin Ni-Fe layered double hydroxide nanosheets with enhanced electrocatalytic activity toward oxygen evolution. *Angew. Chem. Int. Ed.* **2017,** *57,* 172-176.

167. Chen, C.-H.; Abbas, S. F.; Morey, A.; Sithambaram, S.; Xu, L.-P.; Garces, H. F.; Hines, W. A.; Suib, S. L., Controlled Synthesis of Self-Assembled Metal Oxide Hollow Spheres Via Tuning Redox Potentials: Versatile Nanostructured Cobalt Oxides. *Adv. Mater.* **2008,** *20,* 1205-1209.

168. Toby, B. H.; Von Dreele, R. B., GSAS-II: the genesis of a modern open-source all purpose crystallography software package. *J. Appl. Crystallogr.* **2013,** *46,* 544-549.

169. Dong, Y.; Wang, B.; Zhao, K.; Yu, Y.; Wang, X.; Mai, L.; Jin, S., Air-Stable Porous Fe2N Encapsulated in Carbon Microboxes with High Volumetric Lithium Storage Capacity and a Long Cycle Life. *Nano Lett.* **2017,** *17,* 5740-5746.

170. Yang, Y.; Zeng, R.; Xiong, Y.; DiSalvo, F. J.; Abruna, H. D., Cobalt-Based Nitride-Core Oxide-Shell Oxygen Reduction Electrocatalysts. *J. Am. Chem. Soc.* **2019,** *141,* 19241-19245.

171. Deb, A.; Bergmann, U.; Cramer, S. P.; Cairns, E. J., In situ x-ray absorption spectroscopic study of the Li[Ni1/3Co1 ⁄ 3Mn1 ⁄ 3]O2 cathode material. *J. Appl. Phys.* **2005,** *97*, 113523.

172. Lee, Y. S.; Rhee, J. Y.; Whang, C. N.; Lee, Y. P., Electronic structure of Co-Pt alloys: X-ray spectroscopy and density-functional calculations. *Phys. Rev. B* **2003,** *68*, 235111.

173. Friebel, D.; Louie, M. W.; Bajdich, M.; Sanwald, K. E.; Cai, Y.; Wise, A. M.; Cheng, M. J.; Sokaras, D.; Weng, T. C.; Alonso-Mori, R.; Davis, R. C.; Bargar, J. R.; Norskov, J. K.; Nilsson, A.; Bell, A. T., Identification of highly active Fe sites in (Ni,Fe)OOH for electrocatalytic water splitting. *J. Am. Chem. Soc.* **2015,** *137*, 1305-1313.

174. Huang, Z.-F.; Song, J.; Nsanzimana, J. M. V.; Du, Y.; Wang, C.; Xi, S.; Dou, S.; Xu, Z. J.; Wang, X., Chemical and Structural Origin of Lattice Oxygen Oxidation in Co–Zn Oxyhydroxide Oxygen Evolution Electrocatalysts. *Nat. Energy* **2019**.

175. Burke, M. S.; Kast, M. G.; Trotochaud, L.; Smith, A. M.; Boettcher, S. W., Cobalt-iron (oxy)hydroxide oxygen evolution electrocatalysts: the role of structure and composition on activity, stability, and mechanism. *J. Am. Chem. Soc.* **2015,** *137*, 3638-3648.

176. McAlpin, J. G.; Surendranath, Y.; Dinca, M.; Stich, T. A.; Stoian, S. A.; Casey, W. H.; Nocera, D. G.; Britt, R. D., EPR evidence for Co(IV) species produced during water oxidation at neutral pH. *J. Am. Chem. Soc.* **2010,** *132*, 6882-6883.

177. Dhage, P.; Samokhvalov, A.; Repala, D.; Duin, E. C.; Tatarchuk, B. J., Regenerable Fe–Mn–ZnO/SiO2sorbents for room temperature removal of H2S from

fuel reformates: performance, active sites, Operando studies. *Phys. Chem. Chem. Phys.* **2011,** *13,* 2179-2187.

178. Yin, J.; Li, Y.; Lv, F.; Fan, Q.; Zhao, Y. Q.; Zhang, Q.; Wang, W.; Cheng, F.; Xi, P.; Guo, S., NiO/CoN porous nanowires as efficient bifunctional catalysts for Zn-air batteries. *ACS Nano* **2017,** *11,* 2275-2283.

179. Song, S.; Zhou, J.; Su, X.; Wang, Y.; Li, J.; Zhang, L.; Xiao, G.; Guan, C.; Liu, R.; Chen, S.; Lin, H.-J.; Zhang, S.; Wang, J.-Q., Operando X-ray spectroscopic tracking of self-reconstruction for anchored nanoparticles as high-performance electrocatalysts towards oxygen evolution. *Energy Environ. Sci.* **2018,** *11,* 2945-2953.

180. Cruz, W. D. L.; Contreras, O.; Soto, G.; Perez-Tijerina, E., Cobalt nitride films produced by reactive pulsed laser deposition. *Rev. Mex. Fis.* **2006,** *52,* 409-412.

181. Huang, J.; Chen, J.; Yao, T.; He, J.; Jiang, S.; Sun, Z.; Liu, Q.; Cheng, W.; Hu, F.; Jiang, Y.; Pan, Z.; Wei, S., CoOOH nanosheets with high mass activity for water oxidation. *Angew. Chem. Int. Ed.* **2015,** *54,* 8722-8727.

182. Thole, B. T.; van der Laan, G., Branching ratio in x-ray absorption spectroscopy. *Phys. Rev. B* **1988,** *38,* 3158-3171.

183. Krishnan, K. M., Iron L3, 2 near-edge fine structure studies. *Ultramicroscopy* **1990,** *32,* 309-311.

184. Wang, Z. L.; Yin, J. S.; Jiang, Y. D., EELS analysis of cation valence states and oxygen vacancies in magnetic oxides. *Micron* **2000,** *31,* 571-580.

185. Schmid, H. K.; Mader, W., Oxidation states of Mn and Fe in various compound oxide systems. *Micron* **2006,** *37,* 426-432.

186. Tan, P.; Chen, B.; Xu, H.; Cai, W.; He, W.; Liu, M.; Shao, Z.; Ni, M., Co3O4 Nanosheets as Active Material for Hybrid Zn Batteries. *Small* **2018,** *14,* 1800225.

187. Lee, D. U.; Fu, J.; Park, M. G.; Liu, H.; Ghorbani Kashkooli, A.; Chen, Z., Self-Assembled NiO/Ni(OH) Nanoflakes as Active Material for High-Power and High-Energy Hybrid Rechargeable Battery. *Nano Lett.* **2016,** *16,* 1794-1802.

188. Li, B.; Quan, J.; Loh, A.; Chai, J.; Chen, Y.; Tan, C.; Ge, X.; Hor, T. S.; Liu, Z.; Zhang, H.; Zong, Y., A Robust Hybrid Zn-Battery with Ultralong Cycle Life. *Nano Lett.* **2017,** *17,* 156-163.

189. Deng, Y.-P.; Jiang, Y.; Liang, R.; Zhang, S.-J.; Luo, D.; Hu, Y.; Wang, X.; Li, J.-T.; Yu, A.; Chen, Z., Dynamic electrocatalyst with current-driven oxyhydroxide shell for rechargeable zinc-air battery. *Nat. Commun.* **2020,** *11,* 1952.

190. Li, M.; Lu, J., Cobalt in Lithium-Ion Batteries. *Science* **2020,** *367,* 979-980.

191. Zhou, W.; Zhu, D.; He, J.; Li, J.; Chen, H.; Chen, Y.; Chao, D., A scalable top-down strategy toward practical metrics of Ni-Zn battery with total energy densities of 165 Wh/kg and 506 Wh/L. *Energy & Environmental Science* **2020**.

192. Xu, Z. J., Transition metal oxides for water oxidation: All about oxyhydroxides? *Sci. China Mater.* **2020,** *63,* 3-7.

193. McCrory, C. C.; Jung, S.; Peters, J. C.; Jaramillo, T. F., Benchmarking heterogeneous electrocatalysts for the oxygen evolution reaction. *Journal of the American Chemical Society* **2013,** *135,* 16977-87.

194. Liu, X.; Ni, K.; Wen, B.; Guo, R.; Niu, C.; Meng, J.; Li, Q.; Wu, P.; Zhu, Y.; Wu, X.; Mai, L., Deep Reconstruction of Nickel-Based Precatalysts for Water Oxidation Catalysis. *ACS Energy Lett.* **2019,** *4,* 2585-2592.

195. Nai, J.; Lu, Y.; Yu, L.; Wang, X.; Lou, X. W. D., Formation of Ni-Fe Mixed Diselenide Nanocages as a Superior Oxygen Evolution Electrocatalyst. *Adv Mater* **2017,** *29*.

196. Wang, L.; Wang, X.; Xi, S.; Du, Y.; Xue, J., alpha-Ni(OH)2 Originated from Electro-Oxidation of NiSe2 Supported by Carbon Nanoarray on Carbon Cloth for Efficient Water Oxidation. *Small* **2019,** *15*, e1902222.

197. Xia, C.; Jiang, Q.; Zhao, C.; Hedhili, M. N.; Alshareef, H. N., Selenide-Based Electrocatalysts and Scaffolds for Water Oxidation Applications. *Adv Mater* **2016,** *28*, 77-85.

198. Devaguptapu, S. V.; Hwang, S.; Karakalos, S.; Zhao, S.; Gupta, S.; Su, D.; Xu, H.; Wu, G., Morphology Control of Carbon-Free Spinel NiCo2O4 Catalysts for Enhanced Bifunctional Oxygen Reduction and Evolution in Alkaline Media. *ACS applied materials & interfaces* **2017,** *9*, 44567-44578.

199. Grimaud, A.; Diaz-Morales, O.; Han, B.; Hong, W. T.; Lee, Y. L.; Giordano, L.; Stoerzinger, K. A.; Koper, M. T. M.; Shao-Horn, Y., Activating lattice oxygen redox reactions in metal oxides to catalyse oxygen evolution. *Nature chemistry* **2017,** *9*, 457-465.

200. Zheng, X.; Han, X.; Cao, Y.; Zhang, Y.; Nordlund, D.; Wang, J.; Chou, S.; Liu, H.; Li, L.; Zhong, C.; Deng, Y.; Hu, W., Identifying Dense NiSe2/CoSe2 Heterointerfaces Coupled with Surface High - Valence Bimetallic Sites for Synergistically Enhanced Oxygen Electrocatalysis. *Adv. Mater.* **2020,** 2000607.

201. Qian, Z.; Chen, Y.; Tang, Z.; Liu, Z.; Wang, X.; Tian, Y.; Gao, W., Hollow Nanocages of NixCo1−xSe for Efficient Zinc–Air Batteries and Overall Water Splitting. *Nano-Micro Letters* **2019,** *11*.

202. Kong, D.; Wang, H.; Lu, Z.; Cui, Y., CoSe2 nanoparticles grown on carbon fiber paper: an efficient and stable electrocatalyst for hydrogen evolution reaction. *Journal of the American Chemical Society* **2014,** *136,* 4897-900.

203. Jiang, H.; He, Q.; Zhang, Y.; Song, L., Structural Self-Reconstruction of Catalysts in Electrocatalysis. *Acc Chem Res* **2018,** *51,* 2968-2977.

204. Huang, J.; Li, Y.; Zhang, Y.; Rao, G.; Wu, C.; Hu, Y.; Wang, X.; Lu, R.; Li, Y.; Xiong, J., Identification of Key Reversible Intermediates in Self-Reconstructed Nickel-Based Hybrid Electrocatalysts for Oxygen Evolution. *Angewandte Chemie* **2019,** *58,* 17458-17464.

205. Li, Y.; Du, X.; Huang, J.; Wu, C.; Sun, Y.; Zou, G.; Yang, C.; Xiong, J., Recent Progress on Surface Reconstruction of Earth-Abundant Electrocatalysts for Water Oxidation. *Small* **2019,** *15,* e1901980.

206. Parker, J. F.; Chervin, C. N.; Pala, I. R.; Machler, M.; Burz, M. F.; Long, J. W.; Rolison, D. R., Rechargeable nickel-3D zinc batteries: An energy-dense, safer alternative to lithium-ion. *Science* **2017,** *356,* 415-418.

207. Joseph, B.; Iadecola, A.; Simonelli, L.; Mizuguchi, Y.; Takano, Y.; Mizokawa, T.; Saini, N. L., A study of the electronic structure of FeSe(1-x)Te(x) chalcogenides by Fe and Se K-edge x-ray absorption near edge structure measurements. *J Phys Condens Matter* **2010,** *22,* 485702.

208. Das, S.; Lindsay, M. B. J.; Hendry, M. J., Selenate removal by zero-valent iron under anoxic conditions: effects of nitrate and sulfate. *Environmental Earth Sciences* **2019,** *78*.

209. Tang, C.; Cheng, N.; Pu, Z.; Xing, W.; Sun, X., NiSe Nanowire Film Supported on Nickel Foam: An Efficient and Stable 3D Bifunctional Electrode for Full Water Splitting. *Angewandte Chemie* **2015,** *54*, 9351-5.